Effects of spin symmetry breaking in topological insulators

Inauguraldissertation
zur Erlangung der Würde eines Doktors der Philosophie
vorgelegt der
Philosophisch-Naturwissenschaftlichen Fakultät
der Universität Basel

von

Christoph Peter Orth

aus Koblenz, Deutschland

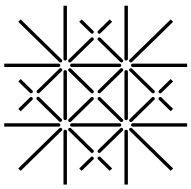

Universität Basel

Basel, 2016

Genehmigt von der Philosophisch-Naturwissenschaftlichen Fakultät

auf Antrag von

Prof. Christoph Bruder

Prof. Thomas L. Schmidt

Prof. Patrik Recher

Basel, den 10. November 2015

Prof. Jörg Schibler, Dekan

Namensnennung-Keine kommerzielle Nutzung-Keine Bearbeitung 3.0 Schweiz
(CC BY-NC-ND 3.0 CH)

Sie dürfen: **Teilen** — den Inhalt kopieren, verbreiten und zugänglich machen

Unter den folgenden Bedingungen:

Namensnennung — Sie müssen den Namen des Autors/Rechteinhabers in der von ihm festgelegten Weise nennen.

Keine kommerzielle Nutzung — Sie dürfen diesen Inhalt nicht für kommerzielle Zwecke nutzen.

Keine Bearbeitung erlaubt — Sie dürfen diesen Inhalt nicht bearbeiten, abwandeln oder in anderer Weise verändern.

Wobei gilt:

- **Verzichtserklärung —** Jede der vorgenannten Bedingungen kann **aufgehoben** werden, sofern Sie die ausdrückliche Einwilligung des Rechteinhabers dazu erhalten.
- **Public Domain (gemeinfreie oder nicht-schützbare Inhalte) —** Soweit das Werk, der Inhalt oder irgendein Teil davon zur Public Domain der jeweiligen Rechtsordnung gehört, wird dieser Status von der Lizenz in keiner Weise berührt.
- **Sonstige Rechte —** Die Lizenz hat keinerlei Einfluss auf die folgenden Rechte:
    - Die Rechte, die jedermann wegen der Schranken des Urheberrechts oder aufgrund gesetzlicher Erlaubnisse zustehen (in einigen Ländern als grundsätzliche Doktrin des **fair use** bekannt);
    - Die **Persönlichkeitsrechte** des Urhebers;
    - Rechte anderer Personen, entweder am Lizenzgegenstand selber oder bezüglich seiner Verwendung, zum Beispiel für **Werbung** oder Privatsphärenschutz.
- **Hinweis —** Bei jeder Nutzung oder Verbreitung müssen Sie anderen alle Lizenzbedingungen mitteilen, die für diesen Inhalt gelten. Am einfachsten ist es, an entsprechender Stelle einen Link auf diese Seite einzubinden.

Quelle: http://creativecommons.org/licenses/by-nc-nd/3.0/ch/ Datum: 12.11.2013

Summary

Topological insulators are one of the most thoroughly investigated systems in condensed matter physics over the last years. In these systems, a prominent role is inevitably taken by time-reversal symmetry, which leads to Kramers theorem and symmetry protected edge states. However, Kramers theorem does not imply that the spin-z component is a good quantum number. This thesis sheds light on several phenomena that appear in topological insulators without this spin conservation, for example in the context of generic helical liquids. A topological insulator strip is examined which allows for forward- and backscattering between the edge states. This results in a measurable effect on the conductance. Furthermore, interfaces between edge-state regions with induced superconductivity, strong interactions and broken spin conservation are analyzed. Calculations using Luttinger liquid theory reveal parafermions at these interfaces. Finally, disorder in the Kane-Mele model in combination with Rashba spin-orbit coupling is studied. It is found that disorder can lead to a topological phase, the topological Anderson insulator, even though the clean system is a trivial insulator.

Electrical science has revealed to us the true nature of light, has provided us with innumerable appliances and instruments of precision, and has thereby vastly added to the exactness of our knowledge.

Nikola Tesla

Acknowledgements

I would like to express my special appreciation and thanks to my adviser, Prof. Thomas L. Schmidt. Your mentoring tremendously helped me to gain physical insights and was always encouraging. Especially, I want to thank you that you had always time for questions and discussions. I would furthermore like to thank Prof. Christoph Bruder for the possibility to finish my thesis in Basel and for the general advice and support in all other aspects. I would also like to thank Prof. Patrik Recher for coming to Basel and having the time to review my thesis and Prof. Daniel Loss for being the chairman of my defense.

Many thanks to my colleagues and collaborators for many fruitful and inspiring discussions and an enjoyable atmosphere in the department.

Finally, I would like to especially thank my wife Sylvie and my family for their never-ending support and patience and the trust I can experience every day.

Contents

Acronyms

1D one-dimensional . . . 2
2D two-dimensional . . . 1
3D three-dimensional . . . 1
TRS time-reversal symmetry . . . 1
HgTeQW mercury telluride–cadmium telluride semiconductor quantum well . . . 1
SLE system of linear equations . . . 17
FQH fractional quantum hall . . . 27
RG renormalization group . . . 3
InAs indium arsenic/gallium antimony . . . 2
BCS Bardeen Cooper Schrieffer . . . 30
BHZ Bernevig Hughes Zhang . . . 1
TAI topological Anderson insulator . . . 3
SCBA self-consistent Born approximation . . . 61
BiSb bismuth antimonide . . . 1

Chapter 1

Introduction

Since the appearance of the seminal works of [Kane05a, Kane05b, Bernevig06] ten years ago, topological insulators have become one of the most fruitful topics in condensed matter physics [Qi11, Hasan10]. Their most prominent feature is the presence of the conducting edge states that are protected by time-reversal symmetry (TRS) from various kinds of perturbations. The topological nature leads to interesting proposals, such as the existence of Majorana particles [Fu08] in these systems. However, topological insulators are also recognized as potential materials for future technologies such as topological quantum computers [Pachos12] or spintronic devices [Pesin12, Žutić04].

One distinguishes between two main categories of topological insulators, viz. two-dimensional (2D) and three-dimensional (3D) topological insulators. 3D topological insulators, such as bismuth antimonide (BiSb), bismuth selenide and bismuth telluride [Hsieh08] exhibit gapless surface states for which the spin and momentum degrees of freedom are locked to each other. In contrast to the 2D case, there are four $\mathbb{Z}_2$ topological invariants that subdivide 3D topological insulators into 16 phases [Fu07]. These phases can be further arranged into weak and strong topological insulators. For weak topological insulators, the surface states comprise four Dirac points, of which an even number is enclosed by the Fermi surface. In strong topological insulators the Fermi surface encloses an odd number of Dirac points, which renders the surface states robust to disorder.

In this thesis we focus on 2D topological insulators. Two different classes of materials are widely accepted to be 2D topological insulators. One class are the mercury telluride–cadmium telluride semiconductor quantum wells (HgTeQWs), which consist of a layered structure of HgTe sandwiched between layers of HgCdTe [König07]. As a result of the heavy Hg atom, bulk HgTe shows a strong spin-orbit coupling and the s-type Γ_6 band lies below the p-type Γ_8 band. This situation represents an inverted band gap. CdTe features a trivial band gap, the lower lying band is of p-type and the upper lying band of s-type. Both materials exhibit a direct band gap which is at the Γ point. If both materials are brought together, the s-type bands and the p-type bands merge. From symmetry considerations, an effective 2D Hamiltonian, the so called Bernevig Hughes Zhang (BHZ) model, for the quantum well can be derived [Bernevig06]. It shows that in the case of a HgTe layer that is of a critical width of about 6.3nm, gapless, counter-propagating spin-up and spin-down states will form at the circumference of the HgTe layer [Roth09]. The dispersion relation of these states has a linear, Dirac cone like shape. Direct backscattering between the counter propagating states is forbidden as it would require an additional spin flip, a term that would contradict the TRS. This renders the edge states robust with respect to non-magnetic impurities and even geometrical distortions cannot localize

them. They are symmetry protected. A $\mathbb{Z}_2$ topological invariant is usually assigned to distinguish non-interacting ordinary insulators from topological insulators [Moore07]. While the edge states are conducting with a quantized conductance of the conductance quantum, $G_0 = 2e^2/h$, for each mode, the bulk material is still insulating. Similar systems for which a topological phase is found are indium arsenic/gallium antimony (InAs) quantum wells [Liu08, Knez11].

The second class of systems are graphene-like materials with a 2D honeycomb lattice, such as silicene, germanene and stanene. These systems can show an inverted, negative bulk bandgap in the case of strong intrinsic spin-orbit coupling and corresponding helical edge states at the circumference. Unfortunately, this is not the case for graphene itself, for which the spin-orbit coupling is basically vanishing [Min06, Yao07]. The essential features, such as the one-dimensional (1D) edge states, are theoretically captured in the Kane-Mele model, which is a further developed Haldane model [Haldane88] with spin.

Recently, research has focused on various enhancements, new materials and new features of topological insulators. Some of the most recent examples include Majorana modes in antiferromagnetic topological superconductors [Ezawa15], in which a Majorana mode can be generated and moved in a 2D plane by controlling a local electric field. Another experiment using silicon impurity doping to suppress residual bulk conductivity in inverted InAs quantum wells and observing robust helical edge states and distinct conductance plateaus has been reported [Du15]. Topological insulators can also be designed in photonic systems, built from an honeycomb array of microcavities [Nalitov15]. Other possible realizations include transition-metal dichalcogenides under strain [Cazalilla14] or organic lattices [Wang13]. Strong correlations in the context of topological insulators are investigated, for example in topological Kondo insulators [Lobos15].

The basic theories for both classes of 2D topological insulators assume a well-preserved spin quantum number. This inevitably leads to right- and left-moving edge states which are helical, meaning for example right-movers, which are purely spin-up and left-movers, which are purely spin-down. Even though time-reversal symmetry is usually present in experimental setups, this does not guarantee that the spin projection on a fixed axis is a good quantum number [Schmidt12]. This effect is present in most setups, caused for example by Rashba spin-orbit coupling, and can evoke interesting effects [Michetti11, Kainaris14, Rod15]. In an effective 1D model of only the edge states, the concept of a generic helical liquid correctly integrates these additional terms. In a generic helical liquid, the spin eigenstates are associated to generic left- and right-moving states through a momentum dependent rotation matrix B_k. Unitarity and TRS inflict physical constraints on B_k, which can be approximated as a real rotation matrix about some angle θ.

We present in this thesis three systems that deal with different phenomena in topological insulators that are partly caused by a broken spin axis symmetry. In Chapter 2 and Chapter 3, the concept of generic helical liquids plays an important role. In Chapter 4, broken spin symmetry due to Rashba spin-orbit coupling is a key ingredient.

1.1 Summary Chapter 2

Chapter 2 is based on the published manuscript [Orth13]. We consider two generic helical liquids on opposite edges of a narrow 2D topological insulator. Due to an inhomogeneity, for example in an external perpendicular electric field, the two corresponding B_k matrices are dissimilar. The narrow sample allows for several tunnel junctions between the two edges. These tunnel junctions can lead to forward- and backscattering of the edge states,

depending on the external field. In this chapter, we demonstrate the strong impact on electron transport due to the inhomogeneity. Measurement of this effect will allow to draw conclusions on the spin textures of the edge states.

1.2 Summary Chapter 3

Chapter 3 is based on the publication [Orth15a]. We show, using an renormalization group (RG) calculation in Luttinger liquid theory, that the combination of electron-electron interactions with a generic helical liquid generates an umklapp scattering term. This can gap out the edge states of a 2D topological insulator and lead to a Mott insulating phase. If additionally some parts of the edges are covered by superconducting gates, which induce a superconducting order parameter and create a gap as well, exotic non-abelian particles can emerge at the interfaces between these regions. Further investigations show that these bound states pin charges in multiples of half the electron charge and account for a Josephson current with 8π periodicity. The bound states are protected by TRS and are fourfold degenerate. Furthermore, we determine their braiding statistics and present a possible implementation of a braiding scheme.

1.3 Summary Chapter 4

The results of Chapter 4 are currently being published, an e-print version is available [Orth15b]. Bulk disorder plays a prominent role for 2D topological insulators. It can lead to a transition from a trivial phase to a topological phase, known as topological Anderson insulator (TAI). Chapter 4 shows that a TAI exists not only in the BHZ model, but also in the Kane-Mele model. The combination of intrinsic spin-orbit coupling λ_{SO}, staggered sublattice potential λ_ν and Rashba spin-orbit coupling λ_R determine whether the system is a topological insulator, a trivial insulator or a TAI. Interestingly, TAIs are found only at the transition between topological insulators and ordinary insulators for $\lambda_\nu \sim \lambda_{SO}$ and small λ_R and not at the transition to a metallic phase for $\lambda_R \sim \lambda_{SO}$ and small λ_ν. Using an analytical approach we find that the disorder leads to a renormalization of λ_ν and the generation of a new, anisotropic Rashba spin-orbit term λ_{R3}. This term by itself can induce a topological transition in materials which otherwise would be trivial insulators.

Chapter 2

Point Contacts and Localization in Generic Helical Liquids

This chapter is based on the published manuscript:
C. P. Orth, G. Strübi and T.L. Schmidt,
Point contacts and localization in generic helical liquids,
Phys. Rev. B 88, 165315.

2.1 Introduction

A characteristic feature of a 2D topological insulator is the occurrence of two conducting electronic states at its circumference, separating the insulating bulk material from an adjacent ordinary insulator or the vacuum. The states are helical, meaning their spin and momentum degree of freedom are coupled. In an illustrative picture, one can speak of a spin-up electron running clockwise and a spin-down electron counterclockwise around the sample. In an ideal setup, which is subject to a bias voltage, these one-dimensional, counter-propagating edge states lead to a quantized conductance of two times the conductance quantum (G_0) through the sample, as long as the Fermi energy is kept in the bulk bandgap. In the presence of time-reversal symmetry (TRS), the two states show opposite spin-projection quantum numbers (s_z) and form a Kramers pair. Backscattering within these states is suppressed due to the helical nature of the states. In other words: Simple backscattering terms in the Hamiltonian must allow electrons to flip their spin, usually a contradiction to the requirement of TRS. This principle prevents the states to localize and two ballistic modes form along the whole borderline between the topological insulator and its non-conducting surroundings.

There are several mechanisms that can lead to deviations from this ideal behavior. In the simplest case, a magnetic impurity can absorb the surplus of spin in a backscattering event [Maciejko09, Tanaka11], which is necessarily combined with a spin-flipping of an electron. This leads to a finite localization length of the electronic states that depends on the density of magnetic impurities in the sample. Another possibility are inelastic two-particle backscattering processes induced by electron-electron interactions [Kane05a]. Contributions to the Hamiltonian of the form of the umklapp scattering

term [1]$U\psi^\dagger_{U\uparrow}\partial_x\psi^\dagger_{U\uparrow}\psi_{U\downarrow}\partial_x\psi_{U\downarrow}$ are time-reversal invariant and exist for interacting systems. It was shown that these terms are irrelevant under the renormalization group for weak interactions and that the helical edge states are stable with respect to these effects [Xu06, Wu06]. Weak interactions together with impurity scattering and finite temperatures can lead to a decrease in conductance that scales with the temperature as $\delta G \propto T^6$, leading away from the universal value of $2G_0$. Umklapp scattering in the same context can lead to $\delta G \propto T^5$. Furthermore, a breaking of the axial spin symmetry, for example due to spin-orbit coupling terms, combined with weak interactions and impurity scattering can lead to corrections of the order of $\delta G \propto T^4$ [Schmidt12].

The special case of a rather long and narrow two-dimensional topological insulator (length L, width $W \ll L$) may feature new backscattering effects and a non-universal conductance. Especially setups, in which electrons can occasionally tunnel from one edge to the other, allow new ways of backscattering without breaking time-reversal invariance. As long as W is larger than the decay length of the edge states into the bulk, these tunnel processes are exponentially suppressed [Zhou08]. Nevertheless, in the intermediate regime of moderate W with respect to the decay length, stable edge states exist that, at certain positions, are coupled stronger and a finite tunneling amplitude manifests. Such processes may be realized intentionally, for example by suitable gating or by applying lithographic techniques for the sample design [Liu08]. Alternatively, also an accidental realization could be possible by tunneling through charge puddles [Skinner12, Väyrynen13]. Charge puddles exist due to doping or disorder in the bulk topological insulator. Edge state electrons can tunnel to these puddles and a consecutive array of puddles connecting the two edges can allow for transfer processes between the edges. For a dilute dispersal of the puddles and as long as such a process remains elastic, it can be described by a point contact at a certain position. Point contact sample setups for 2D topological insulators have been the subject of several recent publications [Liu11c, Schmidt11, Dolcini11, Lee12, Edge13, Huang13, Romeo14, Klinovaja15, Teo09]. Furthermore, extended junctions have been investigated lately [Dolcetto12, Sternativo14].

The scope of this chapter is to investigate narrow 2D topological insulators whose edge states feature both a broken axial symmetry and several, randomly distributed point contacts. It is based on the published manuscript [Orth13]. One usually uses the term of a broken axial symmetry (or just broken spin symmetry) for Hamiltonians with conserved TRS, but which contain spin-flip processes, so that spin is not a good quantum number anymore. This can be the case for example in topological insulator materials with broken bulk inversion asymmetry, structural inversion asymmetry[Qi11] and Rashba spin-orbit coupling [Rothe10]. An effective framework to describe such systems is the concept of a generic helical liquid [Schmidt12]. A generic helical liquid features two counter-propagating edge states at each edge that still form Kramers doublets. However, a spin quantum number can no longer be associated to the edge states. Instead, one labels them for example by quantum numbers $-, +$ for left- and right-moving particles. In these systems, the spin quantization axis rotates as a function of momentum. The projection of $+, -$ states onto states with a fixed spin axis is specified by a unitary, momentum (k) dependent rotation matrix B_k.

We focus in this chapter on the combination of broken axial symmetry that additionally shows a spatial inhomogeneity, meaning that the edge states of a 2D topological insulator exhibit two different B_k matrices. This, in conjunction with several point contacts between

[1]The notation will be clarified later on. We will come back to this kind of terms in the following chapter about parafermions.

the edges, can lead to spin non-conserving back- and forward scattering between the edge states. Thus we find that the conductance shows a deviation from the universal value of $2G_0$ that is expected for ideal 2D topological insulators. For instance, a mercury telluride–cadmium telluride semiconductor quantum well (HgTeQW) that is exposed to a spatial inhomogeneous, external electric field that is perpendicular to the 2D plane of the topological insulator, can be an experimental realization of such a system. Another mechanism that could lead to two different B_k matrices at the sample edges is a difference in chemical potential between the latter.

The chapter will start by introducing the formalism on the example of two generic helical liquids that are coupled by a single point contact and under the influence of a finite voltage bias V. If only Rashba spin-orbit coupling is taken into account, transport properties depend on a single angle $\theta(\mu)$ which describes the tilt between the spin axis of the two generic helical liquids. Depending on $\theta(\mu)$, the tunneling will lead to forward scattering or backscattering.

If a second tunnel contact is added, interference phenomena will occur. The conductance will now depend also on the microscopic details of both tunnel junctions. Finally, in the last part of this chapter we deal with a quasi infinite chain of random tunnel contacts in a narrow sample. We shall show that the microscopic details of the single contacts average out up to a statistical angle, which can be encoded using $\theta(\mu)$. A conductance deviation of $G \propto 2G_0 e^{-L/\ell}$ is found, even for systems with spin conservation. The localization length ℓ strongly depends on $\theta(\mu)$ and therefore the Rashba spin-orbit coupling strength. This leads to the conclusion that the conductance through a narrow 2D topological insulator can be tuned by an inhomogeneous electric field.

2.2 Hamiltonian description of tunnel contacts between generic helical liquids

The model employed in this chapter is an effective theory of two coupled 1D generic helical liquids [Schmidt12]. It can be deduced from, for example, the Bernevig-Hughes-Zhang model [Bernevig06] for HgTeQWs or the Kane-Mele model [Kane05a] for the honeycomb lattice with strong spin-orbit coupling. The description is valid as long as only low energy degrees of freedom are excited, while the Fermi energy μ is kept in the bulk band gap Δ of the topological insulator. For the HgTeQWs the temperature T used in recent experiments is 2.7K $\widehat{=}$ 0.23meV while the band gap varies strongly with the quantum well width and is about 13meV. A difference of a single monolayer of the quantum well can alter the bulk gap by several meV [König13]. This renders the system susceptible to the random occurrence of charge puddles or a local shift of the Fermi energy to the bulk bands.

The bulk gap traversing edge states exhibit a Dirac cone like dispersion relation, which allows to linearize the kinetic part of the Hamiltonian as

$$H_{kin} = -iv_F \sum_{\eta=U,L} \sum_{\alpha=\pm} \alpha \int_{-\infty}^{\infty} \mathrm{d}x\, \psi^\dagger_{\eta\alpha}(x) \partial_x \psi_{\eta\alpha}(x), \tag{2.1}$$

where v_F denotes the Fermi velocity and η labels the upper ($\eta = U$) and lower ($\eta = L$) edges. The index α labels right-movers ($\alpha = +$) and left-movers ($\alpha = -$). We set $\hbar = e = 1$. The fields ψ are free, second-quantized fields in position representation. Due to the special properties of a generic helical liquid, the states cannot be labeled by the spin quantum number anymore. Therefore, we resort to the direction of movement $+, -$

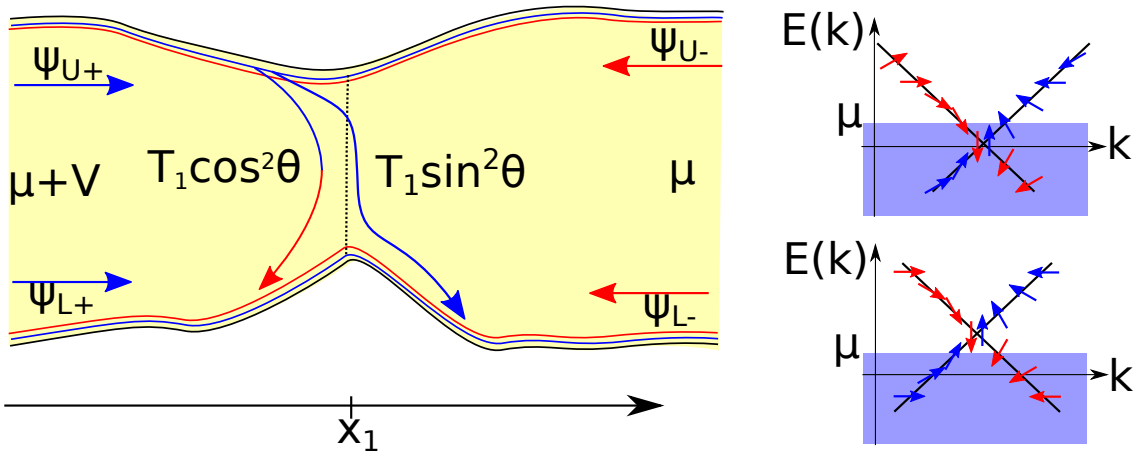

Figure 2.1: (left) Setup of a single point contact between generic helical liquids. The horizontal axis (x) is parallel to the extension of the narrow 2D topological insulator and the figure shows a point-like constriction at $x = x_1$. (right) Spectrum and spin quantization axis for the upper and lower edge states. For a generic helical liquid, the spin quantization axis rotates as a function of momentum. An external field gradient along the y-direction (perpendicular to x, but in the plane of the 2D topological insulator) leads to different quantization axes at the same energy for the upper and lower edge state.

as a well-defined method to label the degrees of freedom. Figure 2.1 shows a layout of the system under consideration. There are two right-moving modes incident from the left, ψ_{U+}, ψ_{L+}, with chemical potential μ and subject to the external voltage V. The counter-propagating states ψ_{U-}, ψ_{L-} are occupied up to the chemical potential μ only. The energies μ and $\mu + V$ are both well inside the bulk gap.

So far, there is no mechanism of backscattering. The transport is ballistic and the Landauer-Büttiker formalism can be applied to calculate the conductance through the sample. In brief, it states that the current through a 1D ballistic conductor is given by the difference in chemical potential times the conductance quantum times the number of channels that contribute to the current. There are two channels[2] in the setup above, leading to the expected result of $I = 2G_0V$ from left to right[3].

2.2.1 Generic helical liquids and time-reversal symmetry

The Hamiltonian (2.1) is expressed in terms of fermionic fields $\psi_{\eta\alpha}(x)$, which we rewrite as a linear combination of the fields in spin-basis $\uparrow, \downarrow$ as follows

$$\begin{pmatrix} \tilde{\psi}_{k,\eta\uparrow} \\ \tilde{\psi}_{k,\eta\downarrow} \end{pmatrix} = B_{k,\eta} \begin{pmatrix} \psi_{k,\eta+} \\ \psi_{k,\eta-} \end{pmatrix}, \tag{2.2}$$

where $B_{k,\eta}$ is a momentum-dependent 2×2 rotation matrix. The index η denotes the upper ($\eta = U$) and lower ($\eta = L$) edge of a sample that extends horizontally along the x-axis. In the case of a spatial inhomogeneous field gradient along the y-direction, it

[2] A channel usually consists of a forward and a backward moving part. Here, these parts are labeled separately but still counted as only one channel on the upper and one channel on the lower edge of the sample.

[3] Using SI-units, $G_0 = e^2/h$ with the electron charge e and Planck constant h. Using $e = \hbar = 1$ yields $G_0 = 1/2\pi$.

is also different for the upper and lower edge. Note that Eq. (2.2) is written using the momentum representation of the fields and becomes non-local if it is written down in the spatial representation. The two representations are connected by a Fourier transform, see Eq. (A.1). The requirement of conserved time-reversal symmetry imposes constraints on the matrix B_k. Additional constraints are given by the unitarity condition $B_k^\dagger B_k = \mathbb{1}$. From this it follows that $B_{k,\eta} = B_{-k,\eta}$, see [Schmidt12] for a derivation and an introduction to generic helical liquids and examples of concrete expressions for $B_{k,\eta}$ for helical edge states in HgTe/CdTe quantum wells in the presence of Rashba spin-orbit coupling.

The time-reversal operator Θ can be chosen such that $\Theta\psi_{k,\eta\alpha}\Theta^{-1} = \alpha\psi_{-k,\eta\bar{\alpha}}$, where $\bar{\alpha} = -\alpha$. Using this definition, the effect of Θ on the Hamiltonian (2.1) is

$$\Theta H_{kin}\Theta^{-1} = iv_F \sum_{\eta=U,L}\sum_{\alpha=\pm} \alpha \int_{-\infty}^{\infty} \mathrm{d}x\, \Theta\psi_{\eta\alpha}^\dagger(x)\Theta^{-1}\partial_x\Theta\psi_{\eta\alpha}(x)\Theta^{-1} \tag{2.3}$$

$$= -iv_F \sum_{\eta=U,L}\sum_{\alpha=\pm} \bar{\alpha} \int_{-\infty}^{\infty} \mathrm{d}x\, \psi_{\eta\bar{\alpha}}^\dagger(x)\partial_x\psi_{\eta\bar{\alpha}}(x) \tag{2.4}$$

$$= H_{kin}, \tag{2.5}$$

i.e. time-reversal symmetry is indeed preserved for the model. The most general form of the matrices $B_{k,\eta}$ is

$$B_{k,\eta} = \begin{pmatrix} \cos(\theta_{k,\eta})e^{i\delta_1} & -\sin(\theta_{k,\eta})e^{i\delta_2} \\ \sin(\theta_{k,\eta})e^{-i\delta_2} & \cos(\theta_{k,\eta})e^{-i\delta_1} \end{pmatrix}, \tag{2.6}$$

where the angle $\theta_{k,\eta}$ and the phases δ_1, δ_2 are functions of momentum and edge index η.

One physical realization to which the theory of a generic helical liquid can be applied are HgTe/CdTe quantum wells with finite Rashba spin-orbit coupling strength and preserved time-reversal symmetry. For this special case, it can be shown that $B_{k,\eta}$ is essentially given by the simpler form

$$B_{k,\eta} = \begin{pmatrix} \cos(\theta_{k,\eta}) & -\sin(\theta_{k,\eta}) \\ \sin(\theta_{k,\eta}) & \cos(\theta_{k,\eta}) \end{pmatrix}. \tag{2.7}$$

Here, $B_{k,\eta}$ can be parametrized by the angle $\theta_{k,\eta}$ only. The right part of Fig. 2.1 shows one possible realization of this spin quantization axis rotation. Based on the Landauer-Büttiker formalism, it was argued at the beginning of Section 2.2 that the conductance does not depend on any of these parameters if no extra terms to the Hamiltonian are added. In the next subsection, we shall show that a single point contact between the upper and lower edges leads to a deviation of the conductance that depends on the difference between the angles $\theta_{k,U} - \theta_{k,L}$ only and that the phases δ_1, δ_2 do not play any role.

In the following, it is assumed at several points that the momentum dependence of $B_{k,\eta}$ is rather weak and that $B_{k,\eta}$ varies only on a large momentum scale $k_0 \gg k_F$. This should be true as, for example, Rashba spin-orbit coupling is small in most materials.

2.2.2 Tunneling between the edge states

The generic helical liquids introduced so far have no means of backscattering and the conductance expected from theory for this system is $2G_0$. Experimentally measurable deviations from this universal conductance value are possible for example if electrons are

allowed to backscatter into states at the opposite edge of the setup. We illustrate such a process in the left part of Fig. 2.1. At the constriction, two scattering processes are possible: an incoming particle can be back-scattered into the state at the opposite edge, or forward scattered. Forward scattering is only possible if the two matrices $B_{k,U}$ and $B_{k,L}$ are distinct for the momentum of the incoming particle. If that is not the case, the two states are orthogonal.

A model to describe such a scattering event is that of a point contact between the two generic helical liquids. In this work, we use the Hamiltonian

$$\begin{aligned} H_j(x) =& \gamma_j \cos(\vartheta_j) \sum_{\sigma=\uparrow,\downarrow} \left[\tilde{\psi}^\dagger_{U\sigma}(x)\tilde{\psi}_{L\sigma}(x) + \text{H.c.}\right] \\ &+ \gamma_j \sin(\vartheta_j) \sum_{\sigma=\uparrow,\downarrow} \left[\tilde{\psi}^\dagger_{U\sigma}(x)\tilde{\psi}_{L-\sigma}(x) + \text{H.c.}\right], \end{aligned} \tag{2.8}$$

with the tunneling coefficient γ_j and the angle ϑ_j that describes the relation between forward- and backscattering. In this form, it is expressed in terms of spin 1/2 electrons $\tilde{\psi}_{U/L\sigma}$ with quantum numbers $\sigma = \uparrow, \downarrow$. The parametrization $\gamma_j \cos(\vartheta_j), \gamma_j \sin(\vartheta_j)$ will become useful in Section 2.3.3. The index j gets a meaning once that several point contacts at different positions x_j are introduced. For a single point contact, the total Hamiltonian reads $H = H_{kin} + H_1(x_1)$. H_{kin} and $H_1(x_1)$ are expressed in two different basis, $\psi_{k,\eta\alpha}$ and $\tilde{\psi}_{k,\eta\sigma}$. This makes a diagonalization of the Hamiltonian non-trivial. A non-equilibrium Keldysh Green's function approach can be applied, which is not part of this thesis. This method gets tedious when extended to several contacts at different positions and will be more useful if electron-electron interactions are taken into account as well[4]. Instead, this chapter relies on a transmission matrix approach, which leads to results even in the limit of arbitrarily many tunnel contacts. However, we use the Keldysh Green's function approach to check the results of the one-contact and two-contact conductances.

It is important to clarify in which limit the approximation of a point contact can be justified. The microscopic extension of the point contact at $x = x_1$ is given by δx_1. If the length δx_1 is small compared to the wavelength of an incident particle wave $1/k_F \gg \delta x_1$, the microscopic details of the contact cannot be resolved and a point-like model with an effective forward- and backscattering amplitude can be justified. For HgTeQWs the Dirac cone that describes the low energy spectrum is located at the Γ-point. Usually this means that $k_F \approx 0$. Using $E_F = v_F k_F \hbar$, $v_F \approx 10^5$m/s and a bandgap of 13meV the variation of k_F inside the gap is about $13\text{meV}/v_F\hbar \approx 2 * 10^8\,\text{m}^{-1}$. This indicates that the approximation of a point-like tunnel contact is valid for contacts which do not extend over distances $\delta x_1 > 5$nm. For temperatures well below the bandgap energy scale and chemical potentials close to the Dirac point larger values of δx_1 are also still possible.

2.3 Scattering matrix theory

2.3.1 Derivation of the full scattering matrix

This subsection is used to derive a general expression of the scattering matrix S for a setup which hosts N point contacts between two generic helical liquids. The scattering matrix can be used for example to calculate observables such as the conductivity. The basic idea

[4]This was done in a so far unpublished work by the author.

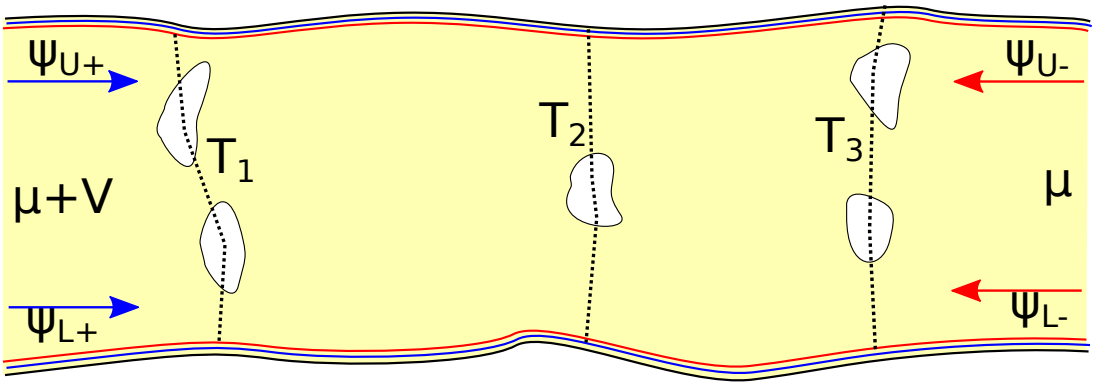

Figure 2.2: A narrow 2D topological insulator in which the two edges are coupled by randomly placed point contacts, realized by several charge puddles at positions x_j.

behind the scattering matrix theory is to find a matrix that connects incoming states to a scattering area to outgoing states[5]. The Hamiltonian of interest is

$$H = H_{kin} + \sum_{j=1}^{N} H_j(x_j), \tag{2.9}$$

where the point contacts are at random positions x_j along the narrow sample. An illustration of this setup is shown in Fig. 2.2. The incoming states in this setup are $\psi_{U+}(x), \psi_{L+}(x)$ for $x < x_1$ and $\psi_{U-}(x), \psi_{L-}(x)$ for $x > x_N$. The outgoing states are $\psi_{U+}(x), \psi_{L+}(x)$ for $x > x_N$ and $\psi_{U-}(x), \psi_{L-}(x)$ for $x < x_1$.

As a first step, we replace the fields $\tilde{\psi}$ by ψ using the $B_{k,\eta}$ matrices. Using two additional Fourier transforms from spatial to momentum representation for the tunneling Hamiltonian part yields

$$H = H_{kin} + \sum_{j=1}^{N} \sum_{\sigma,\sigma'=\uparrow\downarrow} \sum_{\eta=U,L} V_{j,\sigma\sigma'} \frac{1}{L^2} \sum_{k,k'} e^{-ix_j(k-k')} \sum_{\alpha,\beta} \psi^\dagger_{k,\eta\alpha} \left(B^\dagger_{k\eta}\right)^{\alpha\sigma} B^{\sigma'\beta}_{k'\bar{\eta}} \psi_{k',\bar{\eta}\beta}, \tag{2.10}$$

where $V_{j,\sigma\sigma'}$ is kept as a shorthand notation. For the Hamiltonian written in Eq. (2.8), $V_{j,\sigma\sigma'} = \gamma_j \cos(\vartheta_j)$ for spin-conserved tunneling and $V_{j,\sigma\sigma'} = \gamma_j \sin(\vartheta_j)$ for spin-flip tunneling. A vector notation can be introduced to simplify this expression. The state vector is defined as $\psi^\dagger(x) = (\psi^\dagger_{U+}(x), \psi^\dagger_{L+}(x), \psi^\dagger_{U-}(x), \psi^\dagger_{L-}(x))$ and a further Fourier transform of the kinetic part leads to

$$H = v_F \frac{1}{L} \sum_k k\psi^\dagger(k) \left(\sigma_3 \otimes \mathbb{1}\right) \psi(k) + \frac{1}{L^2} \sum_{k,k'} \psi^\dagger_k \mathcal{B}^\dagger_k \Theta(k-k') \mathcal{B}_{k'} \psi_{k'} \tag{2.11}$$

[5] An introduction to scattering matrix theory is given for example in [Bruus04].

with

$$\Theta(k-k') = \sum_j^N V_j e^{-ix_j(k-k')} \tag{2.12}$$

$$\mathcal{B}_k = \begin{pmatrix} B_{k,U}^{1,1} & 0 & B_{k,U}^{1,2} & 0 \\ 0 & B_{k,L}^{1,1} & 0 & B_{k,L}^{1,2} \\ B_{k,U}^{2,1} & 0 & B_{k,U}^{2,2} & 0 \\ 0 & B_{k,L}^{2,1} & 0 & B_{k,L}^{2,2} \end{pmatrix}. \tag{2.13}$$

To understand the form of Θ and $\mathcal{B}_k$ it is helpful at this point to look at the case of a vanishing spin axis rotation. It requires that left-movers (and right-movers) in the upper and lower edge have opposite spin, meaning $\tilde{\psi}_{U\uparrow} = \psi_{U+}$, $\tilde{\psi}_{U\downarrow} = \psi_{U-}$ but also $\tilde{\psi}_{L\uparrow} = \psi_{L-}$, $\tilde{\psi}_{L\downarrow} = \psi_{L+}$. From this the following limiting case is found for the B_k matrices at zero spin rotation $B_{k,U} = \mathbb{1}$ and $B_{k,L} = \sigma_1$ and the $\Theta(k-k')$ as written above. The tunneling matrix V_j is restricted by time-reversal symmetry and a hermiticity condition on the Hamiltonian. Time-reversal symmetry acts on the fields like $\Theta\tilde{\psi}_{\eta,\sigma}(x)\Theta^{-1} = \sigma\tilde{\psi}_{\eta,\bar{\sigma}}$ which, together with the hermiticity condition $V_j^\dagger = V_j$ leads to the form of V_j as

$$V_j = \gamma_j \begin{pmatrix} 0 & \cos(\vartheta_j) & 0 & \sin(\vartheta_j) \\ \cos(\vartheta_j) & 0 & -\sin(\vartheta_j) & \\ 0 & -\sin(\vartheta_j) & 0 & \cos(\vartheta_j) \\ \sin(\vartheta_j) & 0 & \cos(\vartheta_j) & 0 \end{pmatrix}. \tag{2.14}$$

The operators obey the Heisenberg equation of motion

$$\begin{aligned} \partial_t\psi_k(t) =& i\left[H, \psi_k(t)\right] \\ =& iv_F\frac{1}{L}\sum_{k'} k' \left[\psi_{k'}^\dagger(t)\left(\sigma_3\otimes\mathbb{1}\right)\psi_{k'}(t), \psi_k(t)\right] \\ &+ i\frac{1}{L^2}\sum_{k',k''}\left[\psi_{k'}^\dagger(t)\mathcal{B}_{k'}^\dagger\Theta(k'-k'')\mathcal{B}_{k''}\psi_{k''}(t), \psi_k(t)\right] \\ =& -iv_Fk(\sigma_3\otimes\mathbb{1})\psi_k(t) - i\frac{1}{L}\sum_{k'}\mathcal{B}_k^\dagger\Theta(k-k')\mathcal{B}_{k'}\psi_{k'}(t) \end{aligned} \tag{2.15}$$

where the last line is found writing out the sums of the matrix multiplications. To solve the time dependency we apply the Ansatz $\psi_k(t) = \int \frac{\mathrm{d}\omega}{2\pi} e^{-i\omega t}\psi_k(\omega)$ to find

$$\omega\psi_k(\omega) = v_Fk(\sigma_3\otimes\mathbb{1})\psi_k(\omega) + \frac{1}{L}\sum_{k'}\mathcal{B}_k^\dagger\Theta(k-k')\mathcal{B}_{k'}\psi_{k'}(\omega). \tag{2.16}$$

Inserting $\Theta(k-k')$ allows to separate a k independent part ξ_ω^j from the equation in the following way

$$\left[\omega - v_Fk(\sigma_3\otimes\mathbb{1})\right]\psi_k(\omega) = \sum_j^N \mathcal{B}_k^\dagger e^{-ix_jk}\underbrace{\frac{1}{L}\sum_{k'} e^{ix_jk'}V_j\mathcal{B}_{k'}\psi_{k'}(\omega)}_{=\xi_\omega^j}. \tag{2.17}$$

The expression on the left side is the Schrödinger equation of the problem without tunneling, which can be written as $G^{-1}(k,\omega)\psi_k(\omega) = 0$ with the Green's function $G_{\eta\alpha}(k,\omega) = [\omega - \alpha v_F k + i\delta]^{-1}$ where a regularization had to be introduced. This equation can now be solved

$$\psi_k(\omega) = \psi_{k,0}(\omega) + \sum_j^N G(k,\omega)\mathcal{B}_k^\dagger e^{-ix_j k}\xi_\omega^j \tag{2.18}$$

where $\psi_{k,0}(\omega)$ is a general solution of the non-tunneling problem with the constraint $G^{-1}(k,\omega)\psi_{k,0}(\omega) = 0$. The constraint leads to $\psi_{k,0,\eta\alpha}(\omega) = \delta(\omega - \alpha v_F k)\psi_{0,\eta\alpha}(\omega)$ which will become important later on. To finally solve the model, an equation for the ξ_ω^j is derived by inserting $\psi_k(\omega)$ into the definition

$$\xi_\omega^j = \frac{1}{L}\sum_{k'} e^{ix_j k'} V_j \mathcal{B}_{k'} \left[\psi_{k',0}(\omega) + \sum_l^N G(k',\omega)\mathcal{B}_{k'}^\dagger e^{-ix_l k'}\xi_\omega^l\right]. \tag{2.19}$$

We can now define $4N \times 4N$ and $4N \times 4$ matrices

$$\begin{aligned} Q_{jl} &= \frac{1}{L}\sum_{k'} e^{i(x_j - x_l)k'} V_j \mathcal{B}_{k'} G(k',\omega)\mathcal{B}_{k'}^\dagger \\ \zeta_j &= \frac{1}{L}\sum_{k'} e^{ix_j k'} V_j \mathcal{B}_{k'}\psi_{k',0}(\omega) = \frac{1}{v_F} V_j \mathcal{B}_{\omega/v_F} e^{i(\sigma_3\otimes\mathbb{1})x_j\omega/v_F}\psi_0(\omega) \end{aligned}$$

and solve the equation for ξ_ω^j

$$\xi_\omega = (1 - Q)^{-1}\zeta. \tag{2.20}$$

This finally leads to the total result

$$\psi_k(\omega) = \psi_{k,0}(\omega) + \frac{1}{v_F}\sum_{j,l}^N e^{-ix_j k} G(k,\omega)\mathcal{B}_k^\dagger (1-Q)_{jl}^{-1} V_l \mathcal{B}_{\omega/v_F} e^{i(\sigma_3\otimes\mathbb{1})x_l\omega/v_F}\psi_0(\omega) \tag{2.21}$$

and its Fourier transform

$$\begin{aligned} \psi(x,\omega) = \frac{1}{v_F} e^{ix(\sigma_3\otimes\mathbb{1})\omega/v_F}\psi_0(\omega) - \frac{i}{2v_F^2} e^{ix(\sigma_3\otimes\mathbb{1})\omega/v_F} \sum_{j,l}^N \Big[\big(1 + (\sigma_3\otimes\mathbb{1})\mathrm{sign}(x - x_j)\big) \\ \times e^{-i(\sigma_3\otimes\mathbb{1})x_j\omega/v_F}\mathcal{B}_{\omega/v_F}^\dagger (1-Q)_{jl}^{-1} V_l \mathcal{B}_{\omega/v_F} e^{i(\sigma_3\otimes\mathbb{1})x_l\omega/v_F}\psi_0(\omega)\Big] \end{aligned}$$

where the k integration was done for small spin rotation lengths $1/k_0$, a limit described in Subsection 2.2.1.

For the scattering matrix, it is important to distinguish between incoming and outgoing states. Incoming states are those that come from the far left or right side of the sample and have not had the chance to scatter yet, to be more specific they are either right-movers where $x \ll x_i$ or left movers with $x \gg x_i$ (for $i = 1, \ldots, N$). The states are written as

$$\begin{pmatrix} \psi_{U+}^< \\ \psi_{L+}^< \\ \psi_{U-}^> \\ \psi_{L-}^> \end{pmatrix}. \tag{2.22}$$

The outgoing states are either left-movers with $x \ll x_i$ (denoted by $^<$) or right-movers with $x \gg x_i$ (denoted by $^>$) and written as

$$\begin{pmatrix} \psi^>_{U+} \\ \psi^>_{L+} \\ \psi^<_{U-} \\ \psi^<_{L-} \end{pmatrix} = S \begin{pmatrix} \psi^<_{U+} \\ \psi^<_{L+} \\ \psi^>_{U-} \\ \psi^>_{L-} \end{pmatrix} \tag{2.23}$$

where S is the scattering matrix and is defined as the relation between in- and outgoing states. The factor $\big(1 + (\sigma_3 \otimes \mathbb{1})\mathrm{sign}(x - x_j)\big)$ becomes 0 for incoming states and 2 for outgoing states. This yields the following scattering matrix

$$S = 1 - \frac{i}{v_F} \sum_{j,l}^{N} e^{-i(\sigma_3 \otimes \mathbb{1})x_j \omega / v_F} \mathcal{B}^\dagger_{\omega/v_F} (1 - Q)^{-1}_{jl} V_l \mathcal{B}_{\omega/v_F} e^{i(\sigma_3 \otimes \mathbb{1})x_l \omega / v_F} \tag{2.24}$$

Further evaluation Further simplifications are possible in the limit of a small spin rotation length $1/k_0 = \xi$. Q_{ij} can be calculated for $i = j$ using the symmetry condition of $\mathcal{B}_k = \mathcal{B}_{-k}$

$$\frac{V_j}{L} \sum_{k'} \mathcal{B}_{k'} G(k') \mathcal{B}^\dagger_{k'} = \frac{V_j}{L} \sum_{k'} \frac{1}{2} \left[\mathcal{B}_{k'} G(k') \mathcal{B}^\dagger_{k'} + \mathcal{B}_{k'} G(-k') \mathcal{B}^\dagger_{k'} \right] = -\frac{i}{2 v_F} V_j. \tag{2.25}$$

We calculate the off-diagonal elements in the same limit if the tunnel contacts x_i, x_j are separated compared to ξ. This yields

$$\begin{aligned} &\frac{V_j}{L} \sum_{k'} e^{-ik'(x_i - x_j)} \mathcal{B}_{k'} G(k') \mathcal{B}^\dagger_{k'} \\ &\qquad = -\frac{i}{v_F} V_j \mathcal{B}_{\omega/v_F} \left(\frac{1}{2} - (\sigma_3 \otimes \mathbb{1})\mathrm{sign}(x_i - x_j) \right) \mathcal{B}^\dagger_{\omega/v_F} e^{i \frac{\omega}{v_F} |x_i - x_j|}. \end{aligned} \tag{2.26}$$

In summary, we derived the scattering matrix for an arbitrary amount of tunneling contacts between two generic helical liquids in Eq. (2.24). In the following sections, this result will be used to deduce transport properties for a single contact, two contacts, and a chain of N contacts.

2.3.2 Properties of the scattering matrix

This subsection collects general information on the scattering matrix. It derives some very general properties of scattering matrices which can be used as a consistency check of Eq. (2.24). Besides the fact that the scattering matrix has to be unitary, $S^{-1} = S^\dagger$, see for example [Bruus04], it has to suffice some conditions that arise from time reversal invariance. As this symmetry is present in the model, application of the time reversal operator Θ leads to

$$\Theta \psi_{k,\eta\alpha} \Theta^{-1} = \alpha \psi_{-k,\eta\bar{\alpha}} \tag{2.27}$$

$$\Theta \psi^\dagger_{k,\eta\alpha} \Theta^{-1} = \alpha \psi^\dagger_{-k,\eta\bar{\alpha}} \tag{2.28}$$

for each Kramers pair. Furthermore, time reversal exchanges in- and outgoing states and acts as a complex conjugation on complex numbers. Taking the time reversed version of Eq. (2.23) yields

$$\theta \begin{pmatrix} \psi^{>}_{U+} \\ \psi^{>}_{L+} \\ \psi^{<}_{U-} \\ \psi^{<}_{L-} \end{pmatrix} \theta^{-1} = \begin{pmatrix} \psi^{>}_{U-} \\ \psi^{>}_{L-} \\ -\psi^{<}_{U+} \\ -\psi^{<}_{L+} \end{pmatrix} = \theta S \theta^{-1} \theta \begin{pmatrix} \psi^{<}_{U+} \\ \psi^{<}_{L+} \\ \psi^{>}_{U-} \\ \psi^{>}_{L-} \end{pmatrix} \theta^{-1} = S^* \begin{pmatrix} \psi^{<}_{U-} \\ \psi^{<}_{L-} \\ -\psi^{>}_{U+} \\ -\psi^{>}_{L+} \end{pmatrix}. \tag{2.29}$$

A further multiplication by matrices $-i\sigma_2 \otimes \mathbb{1}$ to return to the former state vectors then leads to

$$(i\sigma_2 \otimes \mathbb{1}) \begin{pmatrix} \psi^{<}_{U+} \\ \psi^{<}_{L+} \\ \psi^{>}_{U-} \\ \psi^{>}_{L-} \end{pmatrix} = S^* (i\sigma_2 \otimes \mathbb{1}) \begin{pmatrix} \psi^{>}_{U+} \\ \psi^{>}_{L+} \\ \psi^{<}_{U-} \\ \psi^{<}_{L-} \end{pmatrix} \tag{2.30}$$

which finally results in the condition

$$S = (i\sigma_2 \otimes \mathbb{1})^{-1} S^* (i\sigma_2 \otimes \mathbb{1}) = (\sigma_2 \otimes \mathbb{1}) \left(S^*\right)^{-1} (\sigma_2 \otimes \mathbb{1}). \tag{2.31}$$

We furthermore use the unitarity of S to write it as a block-matrix

$$S = \begin{pmatrix} t & r' \\ r & t' \end{pmatrix}, \qquad t = t'^T, \qquad r' = -r'^T, \qquad r = -r^T. \tag{2.32}$$

This is useful as a sanity check of Eq. (2.24).

2.3.3 A single point contact

In this subsection we apply the result of Eq. (2.24) to the case of a single point contact at $x_1 = 0$ only. For this special case, Q is a 4×4 matrix and given by Eq. (2.25), $Q_{11} = -i/(2v_F)V_1$. The scattering matrix can be simplified as follows

$$S = 1 - \frac{i}{v_F} \mathcal{B}^{\dagger}_{\omega/v_F} (1 - Q_{11})^{-1} V_1 \mathcal{B}_{\omega/v_F}, \tag{2.33}$$

with

$$(\mathbb{1} - Q_{11})^{-1} V_1 = \begin{pmatrix} -\frac{1}{2} i\gamma_1 \sqrt{T_1} & \sqrt{T_1} v_F \cos(\vartheta_1) & 0 & \sqrt{T_1} v_F \sin(\vartheta_1) \\ \sqrt{T_1} v_F \cos(\vartheta_1) & -\frac{1}{2} i\gamma_1 \sqrt{T_1} & -\sqrt{T_1} v_F \sin(\vartheta_1) & 0 \\ 0 & -\sqrt{T_1} v_F \sin(\vartheta_1) & -\frac{1}{2} i\gamma_1 \sqrt{T_1} & \sqrt{T_1} v_F \cos(\vartheta_1) \\ \sqrt{T_1} v_F \sin(\vartheta_1) & 0 & \sqrt{T_1} v_F \cos(\vartheta_1) & -\frac{1}{2} i\gamma_1 \sqrt{T_1} \end{pmatrix}, \tag{2.34}$$

where $\sqrt{T_1} = 4\gamma_1 v_F / (4v_F^2 + \gamma_1^2)$ was used. To calculate the scattering matrix, the assumption that $B_{k,\eta}$ is only given by two angles, one rotating the states in the upper edge and one for the lower edge as in Eq. (2.7), is made again. As mentioned before, one has to be careful with the lower edge as it has to flip the fields for zero rotation. Therefore a constant angle of $\pi/2$ to its $\mathcal{B}_k$ matrix has to be added in the following sense

$$\mathcal{B}_k = \begin{pmatrix} \cos(\theta_U) & 0 & -\sin(\theta_U) & 0 \\ 0 & \cos(\theta_L + \pi/2) & 0 & -\sin(\theta_L + \pi/2) \\ \sin(\theta_U) & 0 & \cos(\theta_U) & 0 \\ 0 & \sin(\theta_L + \pi/2) & 0 & \cos(\theta_L + \pi/2) \end{pmatrix}. \tag{2.35}$$

At this point, some comments about this special form of $B_{k\eta}$ are expedient. The $B_{k\eta}$ matrices could also be written in exponential form as

$$B_{k\eta} = e^{-i\theta_\eta(k)\vec{n}(k)\cdot\vec{\tau}/2} \tag{2.36}$$

where $\vec{\tau}$ is the vector of Pauli matrices, $\theta_\eta(k)$ is some angle and $\vec{n}(k)$ is a unit vector. This exponential describes a rotation of the 2-component spin 1/2 wave-function by an angle $\theta_\eta(k)$ about the axis $\vec{n}(k)$, see for example Ref. [Peskin95] on page 38. The assumption is made that the unit vector $\vec{n}(k)$ is k independent and along the y-axis, this means both perpendicular on the direction of motion (x-axis) and the growth axis of the sample (z-axis). Then one finds the form of the B_k matrix as above (with a factor of two rescaling of the angle). It was shown in Ref. [Schmidt12] that Rashba spin-orbit coupling in the Bernevig-Hughes-Zhang Hamiltonian has this form.

The final result of the scattering matrix using the angle difference $\theta = \theta_U - \theta_L$ reads

$$\begin{aligned} S &= \begin{pmatrix} t & r' \\ r & t' \end{pmatrix} \\ &= \begin{pmatrix} \sqrt{1-T_1} & -i\sqrt{T_1}\sin(\theta+\vartheta_1) & 0 & i\sqrt{T_1}\cos(\theta+\vartheta_1) \\ -i\sqrt{T_1}\sin(\theta+\vartheta_1) & \sqrt{1-T_1} & -i\sqrt{T_1}\cos(\theta+\vartheta_1) & 0 \\ 0 & -i\sqrt{T_1}\cos(\theta+\vartheta_1) & \sqrt{1-T_1} & -i\sqrt{T_1}\sin(\theta+\vartheta_1) \\ i\sqrt{T_1}\cos(\theta+\vartheta_1) & 0 & -i\sqrt{T_1}\sin(\theta+\vartheta_1) & \sqrt{1-T_1} \end{pmatrix}, \end{aligned} \tag{2.37}$$

and meets the general condition of Eq. (2.32). As a first observable, we calculate the conductance $G = G_0 \mathrm{Tr}\left[t^\dagger t\right] = G_0 \mathrm{Tr}\left[t'^\dagger t'\right]$. This yields

$$G = 2G_0\left(1 - T_1\cos^2(\theta+\vartheta_1)\right) \tag{2.38}$$

with G_0 the conductance quantum $G_0 = 1/2\pi$. The angle θ depends on the chemical potential, so that the total current is given by

$$I = \int_\mu^{\mu+V} G(\omega)\,\mathrm{d}\omega \tag{2.39}$$

where V is a voltage difference applied between the left and right side of the contact. The result shows that the conductance depends only on the total angle $\theta_U - \theta_L + \vartheta_1$. This angle determines the fraction of forward to backscattering at the contact. If it is $\pi/2$, all incident particles that cross the point contact are forward scattered and the conductance is $2G_0$. If the angle is 0, all particles are back-scattered, and the conductance is reduced by $2G_0T_1$. As the angle can be tuned by changing for example the chemical potentials, the $\cos^2(\theta)$ behavior could in principle be seen experimentally. This result was to be expected, however, things get more complicated if several contacts are involved.

2.3.4 From the scattering matrix to the transfer matrix

While the scattering matrix S connects incident and out-going states of a scattering region, the transfer matrix connects states left of the region to those right of it. For the setup of Fig. 2.1 it means that it connects $\psi_{U+}(x)$, $\psi_{L+}(x)$, $\psi_{U-}(x)$ and $\psi_{L-}(x)$ for $x < x_1$ to

$\psi_{U+}(x)$, $\psi_{L+}(x)$, $\psi_{U-}(x)$ and $\psi_{L-}(x)$ for $x > x_1$. The states $\psi^{\gtrless}$ are useful again to define the transfer matrix $\mathcal{T}$ by

$$\begin{pmatrix} \psi^{>}_{U+} \\ \psi^{>}_{L+} \\ \psi^{>}_{U-} \\ \psi^{>}_{L-} \end{pmatrix} = \mathcal{T} \begin{pmatrix} \psi^{<}_{U+} \\ \psi^{<}_{L+} \\ \psi^{<}_{U-} \\ \psi^{<}_{L-} \end{pmatrix}. \tag{2.40}$$

It can be straightforwardly obtained by solving a system of linear equations (SLE) from the scattering matrix equation in the right way. It turns out to be very important for the general properties of the transfer matrix that will be used later that a well chosen basis ordering is used in this equation. The transfer matrix for the single contact, obtained from Eq. (2.37), reads (with $j = 1$):

$$\begin{aligned} \mathcal{T}_j(\mu) &= \frac{1}{1 - T_j \cos^2(\theta + \vartheta_j)} \begin{pmatrix} A & B \\ -B^* & A^* \end{pmatrix} \\ A &= \begin{pmatrix} \sqrt{1-T_j} & -i\sqrt{T_j}\sin(\theta+\vartheta_j) \\ -i\sqrt{T_j}\sin(\theta+\vartheta_j) & \sqrt{1-T_j} \end{pmatrix} \\ B &= \cos(\theta+\vartheta_j) \begin{pmatrix} -T_j \sin(\theta+\vartheta_j) & i\sqrt{(1-T_j)T_j} \\ -i\sqrt{(1-T_j)T_j} & T_j \sin(\theta+\vartheta_j) \end{pmatrix}, \end{aligned} \tag{2.41}$$

for the transfer matrix through a single contact which we assume with tunnel amplitude γ_1, ϑ_1 and tunnel probability T_1. The index j is used for an easier generalization to many contacts.

As for the scattering matrix, we obtain the conductance from the diagonal submatrices of the transfer matrix. If λ_j labels the upper left 2×2 submatrix of $\mathcal{T}_j$, the conductance is given by

$$G_j(\mu) = G_0 \mathrm{Tr} \left\{ \left[\left(\lambda_j^* \right)^{-1} \right]^{\dagger} \left(\lambda_j^* \right)^{-1} \right\}. \tag{2.42}$$

We derived this relation from the scattering matrix and its connection to the conductance. Evaluating this leads back to Eq. (2.38) in a straight forward way. The advantage of transfer matrices is that the transfer matrix of two scattering regions can be written as a product of the transfer matrices of the individual regions times a transfer matrix accounting for any phase gains that occur between the scattering regions. This will be exploited in the next section to obtain results for the two point contact case.

2.4 Interferences in the two point contact setup

In the last section, we derived an expression for the transfer matrix for a single contact setup. This result will be extended here to two contacts and richer phenomena due to interference effects will be investigated [Dolcini11, Chu09, Virtanen11, Romeo12]. If more than one contact is considered, the distance between the contacts is a crucial length scale. Let the distance between the contacts at x_1 and x_2 be $\Delta x_2 = x_2 - x_1$, and analogous definitions for the $N - 2$ remaining distances. It is assumed that $\Delta x_j \gg 1/k_F$. This condition, together with $1/k_F \gg \delta x_j$, means that the system is supposed to host well

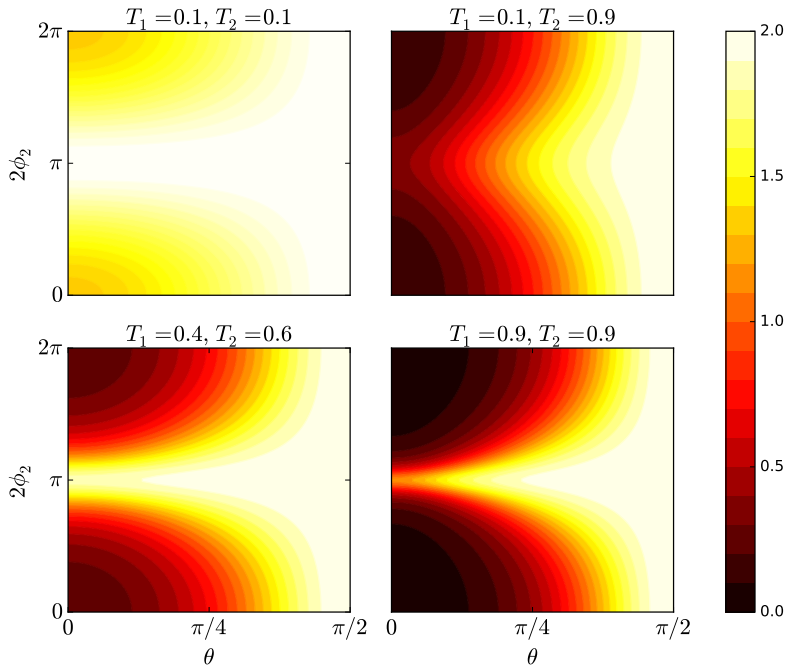

Figure 2.3: Conductance through two point contacts between generic helical liquids as a function of the angle θ between the different spin-quantization axis and the phase $\phi_2 = \Delta x_2 \mu / v_F$. The plots are for spin-conserving tunneling only, meaning $\vartheta_1 = \vartheta_2 = 0$. The unit of conductance is G_0.

defined helical edge states for the most part along the edges. If this limit is not valid, the whole assumption of having helical edge states does not hold anymore and a fully 2D treatment of the system would be necessary.

2.4.1 Transfer matrix for two point contacts

The total transfer matrix through two contacts can be constructed as

$$\tilde{\mathcal{T}}_2 = \mathcal{T}_1 P_2 \mathcal{T}_2, \tag{2.43}$$

where P_2 is a transfer matrix that accounts for the phase that any particle gathers while moving along the edge states between scattering region 1 and 2. For simplicity we assume that it is the same phase for all edge states, $P_2 = \mathrm{diag}(e^{i\phi_2}, e^{i\phi_2}, e^{-i\phi_2}, e^{-i\phi_2})$. If the phase ϕ_j is only due to the distance between the contacts $1, 2$, it is given by $\phi_2 = \Delta x_2 \mu / v_F$. This equation can be evaluated and simplified and finally, the conductance can be extracted from the upper left 2×2 submatrix as written in Eq. (2.42). It yields

$$G(\mu) = 2G_0 \frac{\left\{1 - T_1 \cos^2[\theta(\mu) + \vartheta_1]\right\} \left\{1 - T_2 \cos^2[\theta(\mu) + \vartheta_2]\right\}}{\left|1 + \sqrt{T_1 T_2} \cos\left[\theta(\mu) + \vartheta_1\right] \cos\left[\theta(\mu) + \vartheta_2\right] \, e^{2i\Delta x_2 \mu / v_F}\right|^2}. \tag{2.44}$$

2.4.2 Interference phenomena for two point contacts

$G(\mu)$ is plotted in units of G_0 as a function of the different angles $\theta, \phi_2 = \Delta x_2 \mu / v_F$ in Fig. 2.3. Eq. (2.44) can be read as the product of the conductance through contact 1 times

the conductance through the second contact times an interference term. This expression was also derived by the author using the Green's function formalism based on a Dyson equation, which is so far unpublished and not part of this thesis. Due to the dependence of the angle $\theta(\mu)$ and the phase $\phi_2 = \Delta x_2 \mu / v_F$ on the chemical potential μ, it is possible to tune the conductance and to scan the parameter space illustrated in Fig. 2.3 to some extent.

If the tunneling amplitudes T_1, T_2 are similar, it is always possible to find some length Δx_2 so that $\phi_2 = \pi/2$ and $G(\mu) \approx 2G_0$ for all angles θ, even if $\vartheta_1 = \vartheta_2 = 0$ as in the figure. This is especially the case for strong tunneling, $T_1 = T_2 = 0.9$, which seems to be a contradiction, as backscattering is strong in this limit. This is because at the phase $\phi_2 = \pi/2$ the total phase for a particle going from the first contact to the second contact and back is $2 \times \phi_2 = \pi$. Thus there is destructive interference for all back-scattered particles. The denominator of Eq. (2.44) reaches its minimum and the conductance is maximized at $2G_0$. This effect is independent of the angle $\theta(\mu)$. This can be interpreted as Fabry-Pérot resonances. However, in the case of a large difference in the tunneling strengths T_1, T_2, one contact is suppressed and the system gets similar to the single contact case. Interference plays no important role anymore. This is only true if the difference is significant, as for example $T_1 = 0.1, T_2 = 0.9$. In any case, if the phase ϕ_2 does not lead to destructive interference, $\theta(\mu)$ can be used to tune the system from an insulating to a conducting state.

The conductance depends on the chemical potential in two ways: via $\theta(\mu)$ and through the phases $\phi_2 = \Delta x_2 \mu / v_F$. As mentioned before, we work in the limit $k_0 \gg k_F$. This leads to an expansion of the angle $\theta(\mu) \sim k/k_0 \sim \mu / v_F k_0$. On the other hand, the phase enters with a coefficient $\Delta x_2 / v_F$. Due to the condition $\Delta x_2 \gg 1/k_F \gg 1/k_0$, the phase ϕ_2 is supposed to vary much faster with μ than the angle $\theta(\mu)$. The phase varies with the period of $v_F / \Delta x_2$. Translated back to Si-units, this is $\hbar v_F / \Delta x_2 = 2\text{meV}$ for $v_F = 10^5 \text{m/s}$ and $\Delta x_2 = 200\text{nm}$. The period is therefore within the energy scale of the allowed voltages and chemical potentials and smaller than the bulk bandgap of 13meV. A sweep of the chemical potential through the bandgap will traverse the plots in Fig. 2.3 several times along the y-axis while slowly going to larger θ as well. This results in a periodically varying function for which the amplitude minimum rises slowly with every period for growing μ while the maximum will stay at $2G_0$, see Fig. 2.4 for an illustration. If this behavior can be measured, information about θ can be extracted from the amplitude of the minima.

Another way of tuning the system is to change the Rashba spin-orbit coupling strength. This can be done, for example, by altering an electric field that is perpendicular to the sample. This will result in a different spin rotation length k_0. As k_0 is contained only in $\theta(\mu) \sim k/k_0$, with $k = \mu / v_F$, this change appears exclusively in the cosine terms of Eq. (2.44). The dependence of the conductance minima on $1/k_0$ is shown for small values below $\hbar k_0 v_F = 20\text{meV}$ in Fig. 2.5 by a solid, red line. A fit to a quadratic function is shown in black. As $1/k_0 \sim \lambda_R$ with the Rashba spin-orbit coupling strength λ_R, it is found that the interference minima change with λ_R^2 for small λ_R. This behavior was investigated also numerically on a tight-binding lattice in a yet unpublished work which is not part of this thesis.

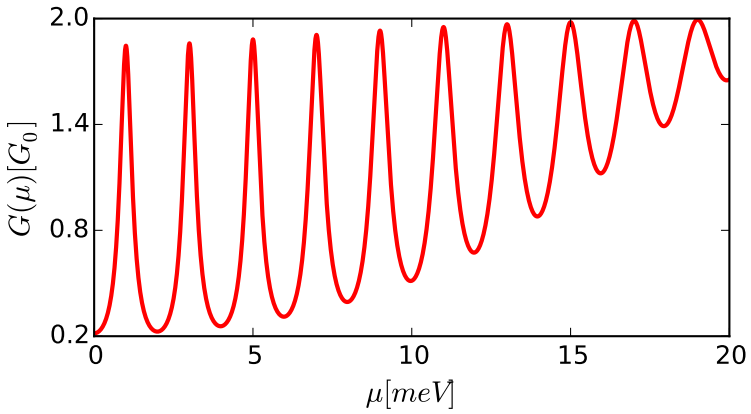

Figure 2.4: Interference pattern in the conductance through two point contacts as a function of the chemical potential μ. The parameters are $\vartheta_1 = 0.4$, $\vartheta_2 = 0.6$, $\hbar v_F/\Delta x_2 = 2\text{meV}/2\pi$ and $\hbar v_F k_0 = 100\text{meV}/2\pi$.

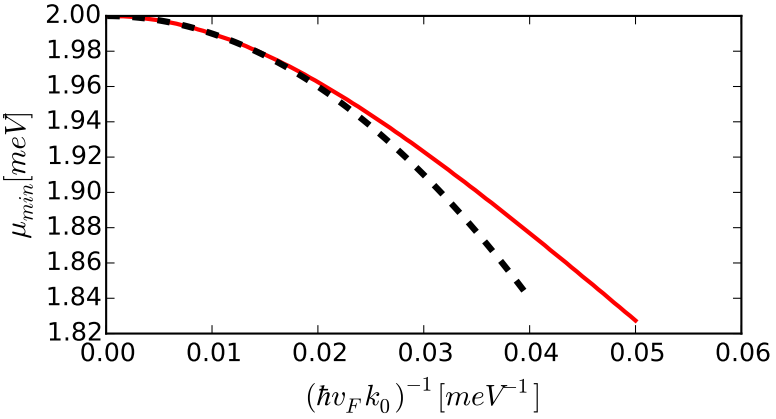

Figure 2.5: Position of the minima at $\mu \approx 2\text{meV}$ in the interference pattern of Fig. 2.4 as a function of the inverse spin rotation length $1/k_0$ (red solid line). The parameters are $\vartheta_1 = 0.4$, $\vartheta_2 = 0.6$ and $\hbar v_F/\Delta x_2 = 2\text{meV}/2\pi$. The black dashed line is a fit to $1/k_0^2$, which is in good agreement with the model for $\hbar v_F k_0 > 100\text{meV}$.

2.5 Generalization of the conductance to a chain of N contacts

The scope of this section is to generalize the results of the last section to a narrow 2D topological insulator with N randomly placed tunnel contacts at x_j, $j = 1, \ldots, N$. Figure 2.2 shows the setup relevant for this section, while the Hamiltonian was already written down in Eq. (2.9) and solved by giving an expression for the exact scattering matrix in Eq. (2.24). The key assumptions are still supposed to be valid, such as $\Delta x_j \gg 1/k_F \gg \delta x_j$, $k_0 \gg k_F$ and that $B_{k\eta}$ are 2×2 rotation matrices. As a first step, we present a recursive transfer matrix scheme to reduce the solution to the single contact scattering matrix. In the second part, averaged quantities are calculated and finally relevant conclusions are drawn.

2.5.1 Constructing the N contact transfer matrix

As it was done already for the two contact setup, the total transfer matrix for N contacts is a product of single contact transfer matrices and transfer matrices that take account of phases gathered in-between. The total transfer matrix for the first j contacts labeled by $\tilde{\mathcal{T}}_j$, while $\mathcal{T}_j$ is just the transfer matrix for the jth contact. Using these definitions, we write down a recursive expression for $\tilde{\mathcal{T}}_j$ as

$$\tilde{\mathcal{T}}_1 = \mathcal{T}_1, \quad \tilde{\mathcal{T}}_j = \tilde{\mathcal{T}}_{j-1} P_j \mathcal{T}_j, \tag{2.45}$$

where again $P_j = \mathrm{diag}\left(e^{i\phi_j}, e^{i\phi_j}, e^{-i\phi_j}, e^{-i\phi_j}\right)$ is the diagonal transfer matrix responsible for the paths in-between. The transfer matrix for N contacts is thus given by

$$\tilde{\mathcal{T}}_N = \mathcal{T}_1 P_2 \mathcal{T}_2 P_3 \ldots P_N \mathcal{T}_N. \tag{2.46}$$

It is assumed again that for the phases $\phi_j = \Delta x_j \mu / v_F$ holds. The full transfer matrix is a complicated function of all individual contact parameters, $\gamma_j, \vartheta_j, \Delta x_j$. It is not meaningful to try to evaluate it exactly for large N. Instead, some information can be obtained using an averaging method described in the next subsection. In order to do this, first some general properties of the transfer matrix have to be derived. The transfer matrix for a single contact was already written down in Eq. (2.41). A close look and a trial and error procedure lead to the following, not straight forward parametrization of the transfer matrix of a single contact,

$$\begin{aligned} \mathcal{T}_j &= \begin{pmatrix} \lambda_j & \rho_j \\ -\rho_j^* & \lambda_j^* \end{pmatrix} \\ \lambda_j &= \begin{pmatrix} a_j & i a_j b_j \\ i a_j b_j & a_j \end{pmatrix}, \quad \rho_j = \begin{pmatrix} c_j & i c_j / b_j \\ -i c_j / b_j & -c_j \end{pmatrix}, \end{aligned} \tag{2.47}$$

where the transfer matrix was expressed by only two complex parameters a_j, c_j and one real parameter b_j. That this reduction is possible is crucial for the calculation in the following subsection. For this, we show that the multiplication of two transfer matrices of the kind of Eq. (2.47) leads to a transfer matrix which has again this form. In more detail, we find

$$\begin{pmatrix} \lambda_1 & \rho_1 \\ -\rho_1^* & \lambda_1^* \end{pmatrix} \begin{pmatrix} \lambda_2 & \rho_2 \\ -\rho_2^* & \lambda_2^* \end{pmatrix} = \begin{pmatrix} \lambda_3 & \rho_3 \\ -\rho_3^* & \lambda_3^* \end{pmatrix} \tag{2.48}$$

with

$$a_3 = \frac{(1-b_1b_2)\left(a_1a_2b_1b_2 + c_1c_2^*\right)}{b_1b_2}$$
$$b_3 = \frac{b_1+b_2}{1-b_1b_2}$$
$$c_3 = \frac{(b_1+b_2)\left(a_1b_1c_2 + b_2c_1a_2^*\right)}{b_1b_2}.$$

As b_1 and b_2 are real, also b_3 has to be real. The matrices P_j cannot be written in this form though, as this would require that $b_j = c_j = 0$ which is ill-defined. However, the product $P_j\mathcal{T}$, where $\mathcal{T}$ is of the form of Eq. (2.47), is again of the form of Eq. (2.47). With these arguments, we have proven recursively that $\tilde{\mathcal{T}}_j$ for all $j = 1, \ldots, N$ has the form of Eq. (2.47).

From any transfer matrix of the form of Eq. (2.47), the dimensionless conductance, which is the conductance divided by G_0, through the first j contacts can be calculated as $\tilde{G}_j = \mathrm{Tr}(t_j^\dagger t_j)$ with $t_j = (\lambda_j^*)^{-1}$. Due to the parametrization a_j, b_j, c_j it is possible to calculate the conductance for j contacts with the help of $\tilde{\mathcal{T}}_{j-1}$, $\mathcal{T}_j$ and P_j. We simplify the result and express it by $\tilde{G}_{j-1}$, G_j and a phase dependent term. This equation reads

$$\tilde{G}_j = \tilde{G}_{j-1}\frac{G_j}{2G_0}\left|1 + \frac{c_{j-1}}{a_{j-1}b_{j-1}}\sqrt{T_j}\cos(\theta+\vartheta_j)e^{-2i\phi_j}\right|^{-2} \tag{2.49}$$

where $G_j = 2G_0 - 2G_0T_j\cos^2(\theta+\vartheta_j)$ and $\tilde{G}_0 = 2$. It will become clear in the next step why $\tilde{G}_j$ is defined in a dimensionless form. The coefficients $a_{j-1}, b_{j-1}, c_{j-1}$ are not properties of the $j-1$th contact only, but complex functions of the parameters of all $j-1$ contacts. It will become important later on that the modulus $v_j = \left|c_j/(a_jb_j)\right|$ is always smaller than 1. This we shall show in appendix B.1.

2.5.2 Disorder average

The expression of Eq. (2.49) still depends on the microscopic parameters T_j, ϑ_j, ϕ_j of all the contacts. The goal is to simplify this equation for the case of large N. Taking the logarithm of this expression yields for the conductance of all N contacts

$$\log\left(\tilde{G}_N\right) = \log(2) + \sum_{k=1}^{N}\left[\log\left(\frac{G_k}{2G_0}\right) - 2\log\left|1 + \frac{c_{k-1}}{a_{k-1}b_{k-1}}\sqrt{T_k}\cos(\theta+\vartheta_k)e^{-2i\phi_k}\right|\right]. \tag{2.50}$$

The next step is to average over all the contacts N. There are two ways of doing the disorder average, resulting in slightly different interpretations.

- The first possibility is that there are M samples, each of equal length and with N tunnel contacts. Especially, without any restriction on the number N, in principle it can also be small. The average is over the samples. The average logarithm of the conductance reads

$$\left\langle \log\left(\tilde{G}_N\right)\right\rangle_{\text{sample}} = \frac{1}{M}\sum_{m=1}^{M}\log\left(\tilde{G}_N^m\right) \tag{2.51}$$

where $\tilde{G}_N^m$ is the dimensionless conductance of the mth sample with N tunnel contacts. With an index m for all the quantities it is found

$$\left\langle \log\left(\tilde{G}_N\right)\right\rangle_{\text{sample}} = \log(2) + \frac{1}{M}\sum_{m=1}^{M}\sum_{k=1}^{N}\left[\log\left(\frac{G_k^m}{2G_0}\right) - 2\log\left|1 + \frac{c_{k-1}^m}{a_{k-1}^m b_{k-1}^m}\sqrt{T_k^m}\cos(\theta+\vartheta_k^m)e^{-2i\phi_k^m}\right|\right]. \tag{2.52}$$

The sum over m can be substituted by an integral over ϕ_k and the constants $r_k = \left|c_{k-1}/(a_{k-1}b_{k-1})\sqrt{T_k}\cos(\theta+\vartheta_k)\right|$. The absolute value part of the expression reads with these definitions

$$\sum_k \int_0^1 \mathrm{d}r \int_0^{2\pi} \mathrm{d}\phi \left[-2\log\left|1 + r_k e^{-2i\phi_k}\right|\right] f_k(r) g_k(\phi), \tag{2.53}$$

where the phases ϕ_k were redefined. The functions $f_k(r), g_k(\phi)$ are not further specified distribution functions. Importantly, $g_k(\phi)$ is assumed to be constant. Because of this, it can be shown numerically that for $r < 1$ this part vanishes while doing the ϕ_k integral. This yields

$$\left\langle \log\left(\tilde{G}_N\right)\right\rangle_{\text{sample}} = \log(2) + \frac{1}{M}\sum_{m=1}^{M}\sum_{k=1}^{N}\log\left(\frac{G_k^m}{2G_0}\right) \tag{2.54}$$

$$= \log(2) + N\left\langle \log\left(1 - T\cos^2(\theta+\vartheta)\right)\right\rangle_{T,\vartheta}, \tag{2.55}$$

where $\langle\rangle_{T,\vartheta}$ is an average over T and ϑ for all contacts and all samples.

- The second possibility is to take a single sample with a large number of point contacts N. This gives the exact logarithm of the conductance

$$\log\left(\tilde{G}_N\right) = \log(2) + \sum_{k=1}^{N}\left[\log\left(\frac{G_k}{2G_0}\right) - 2\log\left|1 + \frac{c_{k-1}}{a_{k-1}b_{k-1}}\sqrt{T_k}\cos(\theta+\vartheta)\right| e^{-2i\phi_k}\right]. \tag{2.56}$$

Due to the large number N, the sum of the second part can be written as an integral over an arbitrary distribution $f(r)$ and a constant distribution $g(\phi)$ as above. This yields

$$\int_0^1 \mathrm{d}r \int_0^{2\pi} \mathrm{d}\phi \left[-2\log\left|1 + re^{-2i\phi}\right|\right] f(r) g(\phi) \tag{2.57}$$

which still vanishes. This leads to

$$\log\left(\tilde{G}_N\right) = \log(2) + N\left\langle \log\left(1 - T\cos^2(\theta+\vartheta)\right)\right\rangle_{T,\vartheta}. \tag{2.58}$$

The difference between the two cases is that in the first case no statement can be made about the total conductance through a single sample. It can strongly vary from sample to sample and only the average over many samples is a meaningful quantity. In the second

case, for large N, the conductance of a single sample will approach a certain value given by

$$G_0 e^{\log(2)+N\langle\log(1-T\cos^2(\theta+\vartheta))\rangle_{T,\vartheta}} = 2G_0 e^{-L/\ell} \tag{2.59}$$

with $\ell = -L/(N\langle\log(1-T\cos^2(\theta+\vartheta))\rangle_{T,\vartheta})$. It only depends on the distribution of the tunnel probabilities and angles ϑ. Because in most experiments there are always several samples produced, a combination of both cases might be necessary.

2.5.3 Discussion and interpretation of the results

We identify the parameter ℓ with the localization length[Delplace12, Anderson80, Pendry94] in the limit of large N,

$$\begin{aligned}\ell &= -\lim_{N\to\infty}\frac{L}{N}\left\langle\log\left(1-T\cos^2(\theta+\vartheta)\right)\right\rangle^{-1}_{T,\vartheta}\\ &= -\frac{1}{n}\left\langle\log\left(1-T\cos^2(\theta+\vartheta)\right)\right\rangle^{-1}_{T,\vartheta},\end{aligned} \tag{2.60}$$

where $n = N/L$ is the contact density. This result shows that the conductance is largest in the case $T_j = 0$ for all j. If this is the case, the logarithm yields 0_- and $\ell = \infty$. The conductance is $2G_0$. In this ideal case, all the transport happens through the two ballistic, helical channels at the sample edges.

In the physical meaningful limit of small $T_j \approx 0$, suppressed spin-flip tunneling $\vartheta_j \approx 0$ and statistically independent variables T and ϑ, the localization length is given by

$$\ell = \frac{1}{n\langle T\rangle\cos^2\left[\theta(\mu)\right]}. \tag{2.61}$$

Tuning the angle $\theta(\mu)$ allows to vary the localization length in the interval $1/n\langle T\rangle < \ell < \infty$. The limit of $\theta = \pi/2$ is that of two ballistic channels again, with conductance $2G_0$. For these settings, tunneling does take place, but due to the angle between the spin quantization axis in the upper and lower edge only forward scattering at each tunnel contact is possible. In the limit of large N the microscopic quantities of a single tunnel contact T_j and ϑ_j do not play a significant role for the total conductance anymore. Only the averaged quantities are important and the conductance depends on their statistics. On the other hand, the origin of θ is global and present all over the sample. It therefore alters the conductance in a relevant way.

2.6 Conclusions

In this chapter we have dealt with narrow 2D topological insulators in which the edge states were coupled through several tunnel contacts. Effects such as Rashba spin-orbit coupling were taken into account by modeling the edge states as generic helical liquids. The model was solved using the equation of motion for the operators and the scattering matrix was derived. Expressions for the conductance through a single contact, two contacts and N contacts were calculated.

While the conductance in a clean sample, without tunnel contacts, is given by the Landauer-Büttiker formalism as $2G_0$, the tunneling allows for backscattering and leads to a reduction of the conductance. In the two contact setup, interference phenomena

become visible in the conductance by changing the chemical potential μ. We found that an inhomogeneity along the plane of the 2D topological insulator can lead to different Rashba spin-orbit coupling strengths (two different momentum-dependent spin quantization axis) at the edges and can have an experimentally tunable effect on the conductance. It was possible to derive a compact expression for the conductance in the case of N contacts. In this case, only statistically relevant quantities determine the conductance. Especially, we obtained that it is tunable by changing the angle between the two different edge state spin quantization axis, $\theta(\mu)$.

The assumptions necessary for the calculation to be valid are that all relevant energies are inside the bulk bandgap and that the helical edge states form a good set of basis states for the calculation. An open question is whether a large enough electric field gradient can be applied to have a measurable effect on the conductance without breaking these assumptions. Furthermore, is it possible in a real setup of a narrow 2D topological insulator to host tunnel contacts as described in this work, possibly due to charge puddles in the bulk? And are there other, possibly competing effects due to a field gradient on the conductance? In principle, the dependence $1/\cos^2(\theta)$ of the conductance on θ could lead to a good signature to identify this effect. However, current experiments seem to still lack the precision to measure the conductance in a topological insulator with sufficient quality, see for example [Wiedmann15] where only conductances of half the expected value were measured. This deviation from the theoretical value is usually explained by the large size of the sample, which promotes inelastic backscattering. Similar disturbing influences have to be expected for narrow 2D topological insulator samples as well. However, most effects that reduce the conductance should not depend on an external electric field gradient in a significant way.

Chapter 3

Non-Abelian Parafermions in Time-Reversal Invariant Interacting Helical Systems

This chapter is based on the published manuscript:
C. P. Orth, R.P. Tiwari, T. Meng and T.L. Schmidt,
Non-Abelian parafermions in time-reversal-invariant interacting helical systems,
Phys. Rev. B 91, 081406.

3.1 Introduction

As the previous chapter of this thesis, this chapter deals with 2D topological insulators as HgTeQWs, and their distinguishing features, first and foremost the 1D helical edge states at their circumference. The time-reversal invariance always plays a crucial role in these systems, especially since it is the main mechanism that protects the edge states from elastic backscattering. The helical nature in combination with the stability of the edge states and the depletion of the bulk material at the Fermi energy leads to a line of interesting phenomena. In general the combination of a 1D helical liquid and a superconductor was predicted to host exotic zero energy bound states such as Majorana fermions [Braunecker12, Schmidt13, Fu08, Fu09, Oreg10, Lutchyn10] and parafermions [Clarke13, Lindner12, Klinovaja15]. These states show characteristic features as for example non-Abelian exchange statistics, which could play an important role for topological quantum computation [Das Sarma06, Nayak08]. First signs of these excitations have already been found in 1D nanowires, coupled to superconductors [Mourik12, Deng12, Das12].

While ideas for experimental setups that host Majorana fermions at the edges of 2D topological insulators can be found in the literature of the last years, concepts about parafermions are still lacking. The two works about parafermions cited above are for fractional quantum hall edge states in proximity to ferromagnets and superconductors. One point for criticism on these setups is the requirement of magnetic fields and superconductivity, two effects that exclude each other to some extent. In these works, the edges of a fractional quantum hall (FQH) insulator with filling factor $\nu = 1/m$, where m is an integer, are arranged in proximity to superconductors and consecutive ferromagnets. Each of

these materials will induce a gap in the FQH edge states. The authors then show that the interface between each two gapped regions on the 1D fractional edge state hosts a bound state which is a non-Abelian anyon, named parafermion. The reason is that the two induced gaps are of different sign, which will become very clear in the language of Luttinger liquids, as will be shown later on. Using an analogy to topological insulators, one can say that the gap induced by the superconductor is topologically nontrivial, while the gap induced by the ferromagnet is topologically trivial. We will discuss another possibility for a system that hosts parafermions in this chapter. The setup consists of a 2D topological insulator such as HgTeQW or InAs heterostructures in proximity to a superconductor. This will induce a nontrivial gap in the edge states that depends on the induced pair potential Δ.

Another part of the edge state shows a strong umklapp scattering, a term that will lead to a trivial gap. This region is hereafter termed Mott insulating region [Ueda13, Sela11]. Umklapp scattering is a Coulomb interaction process that scatters two right-movers into two left-movers and vice versa. Such a process is in general allowed if the chemical potential is at the Dirac point of the 2D topological insulator edge states. In contrast to the FQH setups, time-reversal symmetry is fully preserved in this model but still we find bound states that go beyond Majorana fermions. A similar setup was discussed recently by [Zhang14]. Other proposals about time-reversal invariant parafermions have been made for fractional topological insulators, [Levin09, Klinovaja14], which lack experimental realization so far.

This chapter is structured as follows. In the first section we will discuss the system and related terms of the Hamiltonian in general. Special focus is put on the umklapp scattering term and a RG procedure is derived in the framework of Luttinger liquids that shows how this term can be created from single-particle backscattering and generic helical liquids, which have been explained in section 2.2. The RG-flow equations are derived which show that the generated term is relevant in the RG sense for strong electron-electron interactions. If relevant, the created umklapp scattering term will open up a gap in the 2D topological insulator edge states that depends on the umklapp scattering strength g_{um}.

In section 3.3, it will be shown that two adjacent gapped regions of the topological insulator edge states, one by Δ, one by g_{um}, lead to a zero-energy bound state at their interface. This state is interpreted as a parafermion. These findings will then be used as arguments to introduce spin and charge operators S_i and Q_i that act within the ground state manifold, spanned by the parafermions. Finally, a protocol will be presented that allows to braid two neighboring bound states.

3.2 Induced gaps in the edge state spectra of 2D topological insulators

The goal of this section is to put the derivations and arguments of the following sections about parafermions on a solid theoretical basis. The system is introduced and the Hamiltonian is discussed. The necessary framework to understand most of the calculations presented here is that of Luttinger liquids and bosonization. The theory is understood to be known by the reader and only those steps are performed explicitly that are novel to the best knowledge of the author. Introductions to Luttinger liquids can be found in [Giamarchi03, vonDelft98].

3.2.1 Density-density interaction and helical edge states

The 1D edge states of a 2D topological insulator are usually described by a linearized [Bernevig06, Kane05a] Hamiltonian

$$H_0 = -iv_F \sum_{\sigma=\uparrow\downarrow} \sigma \int \mathrm{d}x \psi_\sigma^\dagger(x) \partial_x \psi_\sigma(x), \tag{3.1}$$

with the Fermi velocity v_F and the right-moving spin-up particles $\psi_\uparrow$ and left-moving spin-down particles $\psi_\downarrow$. In contrast to the previous chapter, here, we will discuss only a single edge and it is assumed that the other edges of the sample are sufficiently far away to prevent any interactions or tunneling between them.

However, in general density-density kind of interactions between the particles is always present within a single edge. While it was shown that this does not influence the conductance [Maslov95, Ponomarenko95, Safi95] it can have an influence on the single-particle spectral function for example, which was found to show a power law behavior in carbon nanotubes [Ishii03]. The Hamiltonian reads

$$H_{int} = \frac{1}{2} \int \mathrm{d}x \, \mathrm{d}y \rho(x) U(x-y) \rho(y), \tag{3.2}$$

with the interaction strength $U(x)$ and the density operator $\rho = \rho_\uparrow + \rho_\downarrow = \sum_\sigma \psi_\sigma^\dagger \psi_\sigma$. Following standard bosonization, the Hamiltonian $H_0 + H_{int}$ can be diagonalized as

$$H_{LL} = \frac{v}{2\pi} \int \mathrm{d}x \left[K \left(\partial_x \theta\right)^2 + \frac{1}{K} \left(\partial_x \phi\right)^2 \right], \tag{3.3}$$

with the Luttinger liquid parameter $K = (1 + 2U_0/\pi v_F)^{-1}$ and the sound velocity $v = v_F/K$. It actually turns out that the derivation of Eq. (3.3) is not straight forward. Especially the bosonization of the kinetic energy part of the Hamiltonian can be tricky. The methods to do this transformation correctly are also needed for later calculations in this chapter, so we decided to do the derivation in detail in the appendix B.2. As commonly done, even though not strictly required within the Luttinger liquid theory, the interaction is of short range only, $U(x) = U_0 \delta(x)$. The canonically conjugate bosonic fields $\phi(x), \theta(x)$ follow the commutation relation $[\phi(x), \theta(y)] = -i\pi\Theta(x-y)$ and are connected to the fermionic fields through the bosonization identity $\psi_\sigma(x) = U_\sigma e^{-i\sigma\phi(x) + i\theta(x)}/\sqrt{2\pi a}$. The parameter a is the short distance cutoff. The Klein factors are defined to be of Majorana-kind, meaning that $U_\uparrow = U_\uparrow^\dagger$ and $U_\downarrow = U_\downarrow^\dagger$. Klein factors account for the right anti-commutation relations between fermions of different species and allow a transition between different N-particle Hilbert spaces [vonDelft98]. The bosonic operators ϕ, θ alone cannot take this into account.

The edge states in 2D topologically insulators are protected from the effects of weak electron interactions. In this limit, a fermionic theory might yield qualitative correct results. For sufficiently strong electron interactions however, Luttinger liquid theory allows to take the interaction into account exactly. The price one has to pay for this is that the spectrum has to be linear, while non-linear deviations would lead to dispersion [Imambekov12] and a finite lifetime of the bosonic excitations.

Time-reversal symmetry plays an important role in this thesis, so in this part we shall define the time-reversal operator and show its effect on the Hamiltonian. For fermions,

one possibility to define the time-reversal operator Θ, which has to be an anti-unitary operator, is

$$\begin{aligned}\Theta\psi_\sigma(x)\Theta^{-1} &= \sigma\psi_{-\sigma}(x)\\ \Theta\psi_{k,\sigma}\Theta^{-1} &= \sigma\psi_{-k,-\sigma}.\end{aligned} \tag{3.4}$$

There are several ways how to deduce the time-reversal operator for the bosonic fields ϕ, θ from this. One possibility is to let Θ act on the Klein factors in the way $\Theta U_\sigma \Theta^{-1} = \sigma U_{-\sigma}$. This way, the Klein factors take account of the required negative sign of $\Theta^2 = -1$. A second option is to define $\Theta U_\sigma \Theta^{-1} = U_{-\sigma}$, $\Theta\phi(x)\Theta^{-1} = \phi(x)+\pi/2$ and $\Theta\theta(x)\Theta^{-1} = -\theta(x)+\pi/2$. In this chapter, we choose the second option to keep the Klein factors as simple as possible so that they can be omitted for certain steps.

The Hamiltonian of Eq. (3.3) transforms under time-reversal as

$$\begin{aligned}\Theta H_{LL}\Theta^{-1} &= \frac{v}{2\pi}\int \mathrm{d}x \left[K\left(\partial_x \Theta\theta\Theta^{-1}\right)^2 + \frac{1}{K}\left(\partial_x\Theta\phi\Theta^{-1}\right)^2\right]\\ &= H_{LL},\end{aligned} \tag{3.5}$$

and is therefore time-reversal symmetric.

3.2.2 Helical edge states in proximity to a superconductor

It was proposed that a 2D topological insulator, which is in close proximity to an s-wave superconductor, hosts edge states that may be described by an effective 1D model with an induced superconducting pairing potential Δ [Fu09]. The mechanism would be that the edge states extend to some degree into the superconductor and inherit its pairing potential Δ_0. The relation between Δ and Δ_0 depends on the coupling between the two materials. This will open up a gap in the edge states. The work by Fu and Kane furthermore assumes that by breaking time-reversal symmetry, a mass term can be induced in the edge states at the remaining part of the topological insulator circumference as well. This could be due to a Zeeman field or proximity to a magnetic material. They show that this would lead to two Majorana fermions as bound states at the interfaces between the two gapped regions. The strength of Δ was also estimated numerically for a tight-binding model, which yields that $\Delta \approx 0.5\Delta_0$ [Black-Schaffer11, Khaymovich11].

Experimental evidence about an induced superconducting gap was found in [Hart14, Pribiag15]. In the first work, a HgTeQW was put between two superconducting electrodes forming a Josephson junction. The carrier density of the quantum well can be tuned with a top gate V_G from the TI (bulk insulating) regime to the normal conducting regime (chemical potential inside the bulk band). A current I is driven from one gate to the other. The measurements suggest that Cooper pairs are induced into the quantum well edge states and are stable over distances of 800nm. This indicates that a proximity induced superconducting gap is indeed possible. Further details about a proximity effect of a superconductor into an ordinary Fermi gas can be found for example in [Volkov95].

In the Bardeen Cooper Schrieffer (BCS) theory of superconductivity [Bardeen57] the pairing potential is given by operators of the kind $\psi_\sigma\psi_{-\sigma}$ and $\psi^\dagger_\sigma\psi^\dagger_{-\sigma}$. We therefore write the induced pairing in the edge states as

$$H_\Delta = \int \mathrm{d}x \left[\Delta\psi^\dagger_\uparrow(x)\psi^\dagger_\downarrow(x) + \mathrm{H.c.}\right] \tag{3.6}$$

for the fermionic fields. It can be easily seen that this Hamiltonian together with the kinetic part has off-diagonal terms in the Nambu spinor basis $(\psi_\uparrow, \psi_\downarrow, \psi_\downarrow^\dagger, -\psi_\uparrow^\dagger)$ and that its spectrum will be gapped. This term can be transformed to the bosonic basis in a straight-forward way, which yields

$$\begin{aligned} &|\Delta| \int \mathrm{d}x \left[e^{i\delta} U_\uparrow^\dagger U_\downarrow^\dagger e^{i\phi(x) - i\theta(x)} e^{-i\phi(x) - i\theta(x)} + \text{H.c.} \right] \\ =&\tilde{\Delta} U_\downarrow U_\uparrow \int \mathrm{d}x \sin\left[2\theta(x) - \delta\right] \end{aligned} \tag{3.7}$$

with $\tilde{\Delta} = |\Delta| / \pi a$, the superconducting phase δ and a definition that the Klein factors are of Majorana kind, $U_\uparrow = U_\uparrow^\dagger$ and $U_\downarrow = U_\downarrow^\dagger$. It was used that emerging commutators will cancel in this expression. The gap in the bosonic picture is hidden in the several minima of the sine function. For large enough $\tilde{\Delta}$, θ gets locked to one of the minima for all x. It is more or less just a constant. The Hamiltonian is again time-reversal symmetric for $\delta = 0$, because $\sin[2(-\theta + \pi/2)] = \sin(2\theta)$.

A ferromagnet in proximity to 2D topological insulator edge states has a similar effect as a superconductor, in the sense that it will also create a gap in their spectrum. The defining part of the Hamiltonian of such a magnetic insulator reads

$$H_M = \int \mathrm{d}x \left[M(x) \psi_\uparrow^\dagger(x) \psi_\downarrow(x) + \text{H.c.} \right]. \tag{3.8}$$

The appendix B.3 shows a derivation for topological insulator edge states gapped by a magnetic insulator and a superconductor. At the interface, the wave function in the two regions is matched and an analytical expression for a bound state, which is a Majorana mode, is found. This calculation is done in the fermionic basis as interaction effects do not play a role. The goal of this chapter is to investigate a similar system, in which the ferromagnet is replaced by a strongly correlated region, which also creates a gap in the edge state spectrum.

3.2.3 Helical edge states with strong umklapp scattering

Another Hamiltonian that is time-reversal symmetric and sometimes present in interacting systems is that of umklapp scattering. It is interesting for this thesis because, as it will be shown later on, it can open up a gap in the edge states as well. It is given by

$$H_{um} \propto \int \mathrm{d}x e^{-4ik_F x} \psi_\uparrow^\dagger (\partial_x \psi_\uparrow^\dagger)(\partial_x \psi_\downarrow) \psi_\downarrow + \text{H.c.}. \tag{3.9}$$

Umklapp scattering is the process of two left-moving states that are scattered into two right-moving ones with opposite spins and vice versa. This interaction process is allowed by time-reversal symmetry, as one can see as follows if the H.c. is written out

$$\Theta H_{um} \Theta^{-1} \propto \int \mathrm{d}x e^{+4ik_F x} \psi_\downarrow^\dagger (\partial_x \psi_\downarrow^\dagger)(\partial_x \psi_\uparrow) \psi_\uparrow + \text{H.c.} = H_{um}. \tag{3.10}$$

Unlike the terms H_0, H_{int} however, umklapp scattering breaks a symmetry called axial spin symmetry. Axial spin symmetry is related to the operator $N_\sigma = \int \mathrm{d}x \rho_\sigma$, which is basically the total number of spin-σ fermions. One finds that $[H_{int}, N_\sigma]$ and $[H_0, N_\sigma]$ vanish, but

$[H_{um}, N_\sigma] \neq 0$. Umklapp scattering does not conserve the total number of spin-up and spin-down. Consequently, an open question that we try to solve in this subsection is if and how H_{um} can be generated in realistic systems.

This question inevitably leads back to a true 2D treatment of the system. A HgTeQW for example can be described by the BHZ model. The latter is block diagonal in spin-space and therefore conserves also N_σ. It can host 1D edge states only that show axial spin symmetry. Off-diagonal blocks arise for example due to structural inversion asymmetry, generated by an external electric field perpendicular to the sample. This causes Rashba spin-orbit coupling that conserves time-reversal symmetry but breaks the axial spin symmetry [Rothe10]. Other systems of 2D topological insulators can show the same effect, such as InAs heterostructures, [Liu08] and silicene, [Liu11a, Liu11b].

The broken axial spin symmetry in the 2D model is linked directly to a broken axial spin symmetry in the effective 1D edge state models used in this work. It can be described using the concept of generic helical liquids, as discussed in Chapter 2.2. For the effective 1D model, the strength of the axial spin symmetry breaking term is given by k_0. It can be calculated numerically for HgTeQWs, InAs heterostructures or topological insulators on the honeycomb lattice, [Schmidt12]. As was shown in Chapter 2, to lowest orders in $1/k_0$ the matrix B_k that contains the symmetry breaking terms can be expressed as

$$B_k \approx \begin{pmatrix} 1 & -k^2/k_0^2 \\ k^2/k_0^2 & 1 \end{pmatrix} \tag{3.11}$$

The matrix B_k can be used to diagonalize the effective Hamiltonian Eq. (3.1) by using the basis ψ_α with $\alpha = +, -$ instead of ψ_σ with $\sigma =\uparrow, \downarrow$. It connects the states through $\psi_{\alpha,k} = \sum_\sigma B_k^{\alpha\sigma}\psi_{\sigma,k}$. Physically, ψ_+ (ψ_-) are right-movers (left-movers).

If Eq. (3.2) is expressed using the $\psi_\pm$ basis, additionally to density-density interaction terms also single-particle backscattering terms and umklapp scattering terms are created. These terms are discussed in some detail in the following. The transformed interaction Hamiltonian reads

$$H_{int} = \frac{1}{L^3}\sum_{kk'q}\sum_{\alpha\beta\alpha'\beta'} U^{\alpha\alpha'}_{\beta\beta'}(q,k,k')\psi^\dagger_\alpha(k)\psi_\beta(k-q)\psi^\dagger_{\alpha'}(k')\psi_{\beta'}(k'+q), \tag{3.12}$$

with

$$U^{\alpha\alpha'}_{\beta\beta'}(q,k,k') = \frac{1}{2}U(q)\left[B_k^\dagger B_{k-q}\right]^{\alpha\beta}\left[B_{k'}^\dagger B_{k'+q}\right]^{\alpha'\beta'}. \tag{3.13}$$

Density-density interaction

Density-density interaction terms are of the form $\rho_\alpha\rho_\beta$ and appear in all kind of α, β combinations. In detail, they read

$$\begin{aligned} H^\rho_{int} = &\frac{1}{L^3}\sum_{kk'q}\sum_{\alpha\alpha'} U^{\alpha\alpha'}_{\alpha\alpha'}(q,k,k')\psi^\dagger_\alpha(k)\psi_\alpha(k-q)\psi^\dagger_{\alpha'}(k')\psi_{\alpha'}(k'+q) \\ &+ \frac{1}{L^3}\sum_{kk'q}\sum_{\alpha} U^{\alpha\bar\alpha}_{\bar\alpha\alpha}(q,k,k')\psi^\dagger_\alpha(k)\psi_{\bar\alpha}(k-q)\psi^\dagger_{\bar\alpha}(k')\psi_\alpha(k'+q) \end{aligned} \tag{3.14}$$

where $\bar{\alpha} = -\alpha$. Assuming that $k/k_0 \ll 1$, so that we can use the approximation of Eq. (3.11) and that $U(q) = U_0$, i.e., the interaction is local, leads to

$$H^{\rho}_{int} = \frac{U_0}{L^3} \sum_{kk'q} \sum_{\alpha\alpha'} \psi^{\dagger}_{\alpha}(k)\psi_{\alpha}(k-q)\psi^{\dagger}_{\alpha'}(k')\psi_{\alpha'}(k'+q) + \frac{U_0}{L^3} \sum_{kk'q} \sum_{\alpha} \frac{1}{k_0^4} \alpha(2kq - q^2)\bar{\alpha}(-2k'q - q^2)\psi^{\dagger}_{\alpha}(k)\psi_{\bar{\alpha}}(k-q)\psi^{\dagger}_{\bar{\alpha}}(k')\psi_{\alpha}(k'+q). \quad (3.15)$$

The last line is fourth order in momenta, so it can only give a minor momentum-dependent correction to the first line. It corresponds to interaction terms which conserve the numbers of right- and left-movers but which are less RG-relevant than density-density interactions. Therefore, it can be ignored and one obtains approximately

$$H^{\rho}_{int} = \frac{U_0}{L} \sum_{q} \sum_{\alpha\alpha'} \rho_{\alpha}(-q)\rho_{\alpha'}(q). \quad (3.16)$$

In real space, this means

$$H^{\rho}_{int} = U_0 \int dx \sum_{\alpha\alpha'} \rho_{\alpha}(x)\rho_{\alpha'}(x), \quad (3.17)$$

or in bosonized form, using the total density $\rho = \rho_+ + \rho_- = -(1/\pi)\partial_x\phi$

$$H^{\rho}_{int} = \frac{U_0}{\pi^2} \int dx (\partial_x\phi)^2. \quad (3.18)$$

Therefore, the sum of kinetic terms and density-density interaction terms can be written as

$$\begin{aligned} H_{kin} + H^{\rho}_{int} &= \frac{v_F}{2\pi} \int dx \left[(\partial_x\theta)^2 + \left(1 + \frac{2U_0}{\pi v_F}\right) (\partial_x\phi)^2 \right] \\ &= \frac{v}{2\pi} \int dx \left[K(\partial_x\theta)^2 + \frac{1}{K}(\partial_x\phi)^2 \right], \end{aligned} \quad (3.19)$$

with the definitions of the renormalized sound velocity and the Luttinger parameter as

$$\begin{aligned} K &= \left(1 + \frac{2U_0}{\pi v_F}\right)^{-1/2} \\ v &= \frac{v_F}{K}. \end{aligned} \quad (3.20)$$

For repulsive interactions ($U_0 > 0$), one has $0 < K < 1$ and $v > v_F$ as expected. As usual, the Luttinger Hamiltonian can be diagonalized by rescaling the fields to $\tilde{\phi} = \phi/\sqrt{K}$ and $\tilde{\theta} = \sqrt{K}\theta$,

$$H_{kin} + H^{\rho}_{int} = \frac{v}{2\pi} \int dx \left[(\partial_x\tilde{\theta})^2 + (\partial_x\tilde{\phi})^2 \right]. \quad (3.21)$$

This Hamiltonian is mentioned here, because all normal ordering operations below will be with respect to the eigenmodes $\tilde{\theta}(x)$ and $\tilde{\phi}(x)$ of the Luttinger Hamiltonian of the interacting system. As it could be guessed already, the density-density correction due to the B_k matrices is captured in the Luttinger liquid framework already.

Umklapp terms

Next is to proceed with the umklapp terms. There are only two which are related by hermitian conjugation, so

$$\begin{aligned} H_{int}^{um} &= \frac{1}{L^3}\sum_{kk'q} U_{--}^{++}(q,k,k')\psi_+^\dagger(k)\psi_-(k-q)\psi_+^\dagger(k')\psi_-(k'+q) + \text{H.c.} \\ &= \frac{U_0}{L^3}\sum_{kk'q}[B_k^\dagger B_{k-q}]^{+-}[B_{k'}^\dagger B_{k'+q}]^{+-}\psi_+^\dagger(k)\psi_-(k-q)\psi_+^\dagger(k')\psi_-(k'+q) + \text{H.c.} \\ &\approx -\frac{U_0}{L^3}\frac{1}{k_0^4}\sum_{kk'q} q^2(2k-q)(2k'+q)\psi_+^\dagger(k)\psi_-(k-q)\psi_+^\dagger(k')\psi_-(k'+q) + \text{H.c.}. \end{aligned} \tag{3.22}$$

As expected, the amplitude of this process vanishes for $q = 0$, as well as for $q = 2k$ and $q = -2k'$, because these cases would involve scattering between Kramers partners, and these have no overlap. Therefore, it can be seen already that these processes are quartic in the momenta, and will always create four derivatives when Fourier transformed to real space. In contrast, if there was a finite Fermi momentum $k_F \neq 0$, a term in real space could be generated which contains k_F^2 and two derivatives. However, for $k_F = 0$, a Fourier transformation inevitably leads to a term containing four spatial derivatives.

The conclusion is that the pure Hamiltonian H_{int}^{um} for $k_F = 0$ does not contain a term $\propto \psi_+^\dagger(\partial_x\psi_+^\dagger)(\partial_x\psi_-)\psi_-$. Nevertheless, such a term may still be generated from RG if one starts with single-particle backscattering.

Single-particle backscattering

The last category of terms that appears are single-particle backscattering terms of the form $\psi_\alpha^\dagger\psi_{\bar\alpha}\rho_\alpha$. We show in this paragraph which of the terms are important and how to bosonize the related Hamiltonian. The single-particle backscattering terms are

$$H_{int}^{spb} = \frac{2}{L^3}\sum_{kk'q}\sum_{\alpha\alpha'} U(q)[B_k^\dagger B_{k-q}]^{\alpha\alpha}[B_{k'}^\dagger B_{k'+q}]^{\alpha'\bar\alpha'}\psi_\alpha^\dagger(k)\psi_\alpha(k-q)\psi_{\alpha'}^\dagger(k')\psi_{\bar\alpha'}(k'+q), \tag{3.23}$$

where some symmetries of $U_{\beta\beta'}^{\alpha\alpha'}$ and relabeling were exploited[1]. For local interactions and small $1/k_0$ one finds

$$H_{int}^{spb} = -\frac{2U_0}{k_0^2L^2}\sum_q\sum_\alpha \rho_\alpha(-q)\sum_{\alpha'k'}\alpha' q(2k'+q)\psi_{\alpha'}^\dagger(k')\psi_{\bar\alpha'}(k'+q). \tag{3.24}$$

The factor $q(2k'+q)$ shows that the term vanishes for $q = 0$ and $k' = -q/2$. This means that the processes $(k_+, k'_+) \to (k_+, k'_-)$ as well as $(k_+, k'_+) \to (k_+ + 2k', -k'_-)$ are forbidden, which is expected because both involve scattering between Kramers partners which is

[1]During this procedure it becomes necessary to commute a single-particle backscattering term $\psi_\alpha^\dagger\psi_{\bar\alpha}$ past a density term $\psi_{\alpha'}^\dagger\psi_{\alpha'}$, which leads to a nontrivial commutator that gives an additional chemical potential term (a term containing only two fermion operators). However, this term is spurious and is an artifact of starting with a fermionic Hamiltonian which is not normal-ordered. Therefore, in the following such terms will be discarded.

forbidden by time-reversal symmetry. The last line suggests shifting one momentum sum to $\tilde{k} = k' + q/2$. Then, using the Fourier transforms from Eq. (A.1) one finds

$$H_{int}^{spb} = -\frac{2U_0}{k_0^2 L^2} \int dx dx_1 dx_2 \sum_{\alpha\alpha'} \alpha' \rho_\alpha(x) \psi_{\alpha'}^\dagger(x_1) \psi_{\bar{\alpha}'}(x_2) \sum_{q\tilde{k}} 2q\tilde{k} e^{iq(x-x_1/2-x_2/2)} e^{i\tilde{k}(x_1-x_2)}. \tag{3.25}$$

This suggests using center-of-mass and relative coordinates, $y_1 = (x_1 + x_2)/2$ and $y_2 = x_1 - x_2$,

$$\begin{aligned}
H_{int}^{spb} &= -\frac{4U_0}{k_0^2 L^2} \int dx dy_1 dy_2 \sum_{\alpha\alpha'} \alpha' \rho_\alpha(x) \psi_{\alpha'}^\dagger(y_1 + y_2/2) \psi_{\bar{\alpha}'}(y_1 - y_2/2) \sum_{q\tilde{k}} q\tilde{k} e^{iq(x-y_1)} e^{i\tilde{k}y_2} \\
&= \frac{4U_0}{k_0^2} \int dx dy_1 dy_2 \sum_{\alpha\alpha'} \alpha' \rho_\alpha(x) \psi_{\alpha'}^\dagger(y_1 + y_2/2) \psi_{\bar{\alpha}'}(y_1 - y_2/2) \partial_x \partial_{y_2} \delta(x - y_1) \delta(y_2) \\
&= \frac{4U_0}{k_0^2} \int dx dy_1 dy_2 \sum_{\alpha\alpha'} \alpha' [\partial_x \rho_\alpha(x)] \partial_{y_2} \left[\psi_{\alpha'}^\dagger(y_1 + y_2/2) \psi_{\bar{\alpha}'}(y_1 - y_2/2) \right] \delta(x - y_1) \delta(y_2) \\
&= \frac{2U_0}{k_0^2} \int dx \sum_{\alpha\alpha'} \alpha' \rho'_\alpha(x) \left[\psi_{\alpha'}^{\dagger'}(x) \psi_{\bar{\alpha}'}(x) - \psi_{\alpha'}^\dagger(x) \psi'_{\bar{\alpha}'}(x) \right].
\end{aligned} \tag{3.26}$$

This leads to

$$H_{int}^{spb} = \frac{2U_0}{k_0^2} \int dx [\partial_x \rho(x)] \left(\psi_+^{\dagger'} \psi_- - \psi_+^\dagger \psi'_- - \psi_-^{\dagger'} \psi_+ + \psi_-^\dagger \psi'_+ \right), \tag{3.27}$$

where $\rho = \rho_+ + \rho_-$. "Naive" bosonization, i.e., without taking care of proper normal-ordering, would lead to

$$\begin{aligned}
H_{int}^{spb} &\propto \int dx [\partial_x^2 \phi(x)] \left\{ (i\partial_x \varphi_+ + i\partial_x \varphi_-) e^{2i\phi} - (i\partial_x \varphi_- + i\partial_x \varphi_+) e^{-2i\phi} \right\} \\
&\propto \int dx [\partial_x^2 \phi(x)] [\partial_x \theta(x)] \sin[2\phi(x)],
\end{aligned} \tag{3.28}$$

with $\varphi_\sigma(x) = \sigma\phi(x) - \theta(x)$. This term has the same symmetries as the linear Rashba Hamiltonian ($\propto \partial_x \theta \cos(2\phi)$), but it contains in addition the operator $\partial_x^2 \phi(x)$ which reduces its scaling dimension.

To correctly bosonize this term, it is convenient to use a point-split expression, as was done already in the Appendix B.2 for the kinetic part of the Hamiltonian. The point-splitting process essentially removes any divergences from the operators and gathers them in a prefactor. In this way, it is possible to derive the correct cutoff dependency of the prefactor, which will become important in the RG-procedure to follow. We drop the Klein factors because they are not supposed to make any physical difference in the following. The point-splitted Hamiltonian is written as

$$\begin{aligned}
H_{int}^{spb} = \frac{2U_0}{k_0^2} \int dx \lim_{x_{1,2,3,4} \to x} \partial_{x_1} \sum_\alpha \left[\psi_\alpha^\dagger(x_1) \psi_\alpha(x_2) + \psi_\alpha^\dagger(x_2) \psi_\alpha(x_1) \right] \\
\times \partial_{x_3} \sum_\beta \beta \left[\psi_\beta^\dagger(x_3) \psi_{\bar{\beta}}(x_4) - \psi_\beta^\dagger(x_4) \psi_{\bar{\beta}}(x_3) \right].
\end{aligned} \tag{3.29}$$

The calculation is quite lengthy and technical, so it will be done in Appendix B.3.4. The bosonized version of the single-particle backscattering Hamiltonian reads

$$H_{int}^{spb} = -\lambda v_F a \left(\frac{2\pi a}{L}\right)^K \int dx \, {}^*_*(\partial_x^2\phi)(\partial_x\theta)\sin[2\phi(x)]{}^*_*, \tag{3.30}$$

it reveals a cutoff dependency of a^{K-1}, which cannot be obtained from the "naive" bosonization approach. As required, this term still respects time-reversal symmetry, as one can show using $\Theta\partial_x^2\phi\Theta^{-1} = \partial_x^2\phi$, $\Theta\partial_x\theta\Theta^{-1} = -\partial_x\theta$ and $\sin[2\Theta\phi\Theta^{-1}] = \sin[2\phi+\pi] = -\sin[2\phi]$. We introduced the parameter λ during the bosonization process. It is dimensionless and given by $\lambda = 12U_0/(\pi^2 v_F k_0^2 a^2)$. In the following part, it will be used as the small parameter for the RG-procedure. In the non-interacting limit, $K \to 1$ and H_{int}^{spb} is independent of a ($\lambda \propto a^{-2}$), which is a good indication that the bosonization was done correctly. For small spin-axis rotation, $1/k_0 \to 0$ and the single-particle backscattering disappears, as it should do. The same holds for $U_0 \to 0$. These remarks close the discussion about emergent terms due to generic helical liquids and interactions. What follows is an RG-analysis of the single-particle backscattering, which finally leads to the generation of a relevant umklapp scattering term.

How umklapp scattering is generated

In subsection 3.2.3 some umklapp terms were generated already. However, it was argued that these terms always contain four derivatives. They have a reduced scaling dimension compared to the term of Eq. (3.9) and will always remain renormalization group irrelevant. The first order RG equation of these terms would simply be $dg_{um}/d\ell \propto -4K$.

We will argue in this subsection how a relevant umklapp scattering term of the form of Eq. (3.9) is generated, which contains only two derivatives. A first look at the umklapp scattering Hamiltonian Eq. (3.9) and at the single-particle backscattering Eq. (3.27) reveals already a major analogy. The umklapp term is essentially two times the $\psi_\beta^\dagger\psi_{\bar\beta}$ part of the single-particle backscattering. Here, we shall show that the first one is generated in second order RG from the the last one. The derivation is quite technical again, and a major part is banished to the appendix. Basic ideas about the RG theory can be found for example in [Cardy96]. As a start, the following operator equation is written down

$$\begin{aligned}
&{}^*_*(\partial_{x_1}^2\phi)(\partial_{x_1}\theta)\sin[2\phi(x_1,t_1)]{}^*_*\,{}^*_*(\partial_{x_2}^2\phi)(\partial_{x_2}\theta)\sin[2\phi(x_2,t_2)]{}^*_* \\
\approx &-\sum_{\alpha,\beta=\pm}\frac{1}{4}\left(a+i(x_2^- - x_1^-)\right)^{\alpha\beta K}\left(a-i(x_2^+-x_1^+)\right)^{\alpha\beta K}\left(\frac{2\pi}{L}\right)^{2\alpha\beta K} \\
&\Big[-16K^2\left(\partial_{x_1}^2 g_{++}\right)^2\left(\partial_{x_1}g_{-+}\right)^2 + 4\alpha\beta K\left(\partial_{x_1}^2 g_{++}\right)^3 + 4\alpha\beta K\left(\partial_{x_1}g_{-+}\right)^2\left(\partial_{x_1}^4 g_{++}\right) \\
&+ 8\alpha\beta K\left(\partial_{x_1}g_{-+}\right)\left(\partial_{x_1}^2 g_{++}\right)\left(\partial_{x_1}^3 g_{-+}\right) - \left(\partial_{x_1}^4 g_{++}\right)\left(\partial_{x_1}^2 g_{++}\right) - \left(\partial_{x_1}^3 g_{-+}\right)^2\Big] \\
&\times {}^*_*e^{i\alpha 2\phi(x_1,t_1)+i\beta 2\phi(x_2,t_2)}{}^*_* =: g(a),
\end{aligned} \tag{3.31}$$

with the definitions

$$\begin{aligned}
g_{\alpha\beta} &= -\frac{\alpha}{4}\log\left[1-e^{-(a+i(x_2-vt_2-x_1+vt_1))\frac{2\pi}{L}}\right] - \frac{\beta}{4}\log\left[1-e^{-(a-i(x_2+vt_2-x_1-vt_1))\frac{2\pi}{L}}\right] \\
x_i^\pm &= x_i \pm vt_i.
\end{aligned} \tag{3.32}$$

The equation contains already an essential part of the results: two single-particle backscattering terms normal ordered yield the expression $:e^{i\alpha 2\phi(x_1,t_1)+i\beta 2\phi(x_2,t_2)}:$, which is something like an umklapp scattering term, times a complicated, cutoff dependent prefactor. The equation is derived in Appendix B.4.

To summarize, the system under consideration consists of the Luttinger liquid Hamiltonian of Eq. (3.3) for fermions of a generic, interacting helical liquid. The combined effect of a generic helical liquid together with the interaction furthermore leads to a single-particle backscattering term, which is not part of the Hamiltonian of Eq. (3.3) so far. In the following, this term will be treated as a perturbation and the second order RG-equations will be derived. For the RG treatment, we use the expectation value

$$Z = \langle T e^{-i\int_{-\infty}^{\infty} \mathrm{d}t_1 V(t_1)} \rangle_0. \tag{3.33}$$

Z denotes the usual real-time partition function and $\langle A\rangle_0$ is the expectation value $\langle A\rangle_0 = \langle A e^{-itH_0}\rangle$ of the operator A in the unperturbed system (index 0) and the vacuum. $V(t)$ is the perturbation, in this case the bosonized single-particle backscattering Hamiltonian, while H_0 is the Luttinger liquid Hamiltonian. The partition function is expanded for small perturbations

$$\begin{aligned}
Z \approx& Z_0 - i\int_{-\infty}^{\infty} \mathrm{d}t \langle V(t)\rangle_0 - \frac{1}{2}\int_{-\infty}^{\infty}\mathrm{d}t\int_{-\infty}^{\infty}\mathrm{d}t' \langle V(t)V(t')\rangle_0 \\
=& Z_0 + i\lambda v_F a \left(\frac{2\pi a}{L}\right)^K \int_{-\infty}^{\infty}\mathrm{d}t \int dx \langle :(\partial_x^2\phi)(\partial_x\theta)\sin[2\phi(x)]: \rangle_0 \\
&- \frac{1}{2}\lambda^2 v_F^2 a^2 \left(\frac{2\pi a}{L}\right)^{2K} \int_{-\infty}^{\infty} \mathrm{d}t_1\,\mathrm{d}t_2\,\mathrm{d}x_1\,\mathrm{d}x_2 \\
&\times \langle :(\partial_{x_1}^2\phi_1)(\partial_{x_1}\theta_1)\sin[2\phi_1]: :(\partial_{x_2}^2\phi_2)(\partial_{x_2}\theta_2)\sin[2\phi_2]: \rangle_0,
\end{aligned} \tag{3.34}$$

with the shorthand notation $\phi_i = \phi(x_i,t_i)$, $\theta_i = \theta(x_i,t_i)$, so the operators are now time and space dependent and the interaction picture is used. The small, dimensionless parameter that was expanded for is λ. The second order term contains just the operator expression that was treated in Eq. (3.31).

The basic idea of the RG calculation is that any expectation value must be independent of the exact value of the cutoff, in this case the short distance cutoff a. One therefore rescales the cutoff, as for example in an exponential form $a(\ell) = ae^{\ell}$, and demands that Z stays independent of that change. Usually, this will only be the case if one additionally rescales the coupling parameters as well, here λ. For the expanded Z in perturbation theory, this even implies that every order in λ of Z has to stay constant with respect to a shift of a. The procedure is best illustrated using only the first order of Eq. (3.34). With the rescaling $a \to a(1+d\ell)$ and $\lambda \to \lambda + d\lambda$ one obtains the equation

$$\begin{aligned}
&i\lambda v_F a \left(\frac{2\pi a}{L}\right)^K \int_{-\infty}^{\infty}\mathrm{d}t \int dx \langle :(\partial_x^2\phi)(\partial_x\theta)\sin[2\phi(x)]: \rangle_0 \\
=& i(\lambda+d\lambda)v_F a(1+d\ell)\left(\frac{2\pi a(1+d\ell)}{L}\right)^K \int_{-\infty}^{\infty}\mathrm{d}t \int dx \langle :(\partial_x^2\phi)(\partial_x\theta)\sin[2\phi(x)]: \rangle_0.
\end{aligned} \tag{3.35}$$

It is now straight forward to extract the condition

$$\lambda a^{K+1} = (\lambda+d\lambda)a^{K+1}(1+d\ell)^{K+1} \approx \lambda a^{K+1} + d\lambda a^{K+1} + \lambda a^{K+1}(K+1)d\ell, \tag{3.36}$$

where the equation was linearized for infinitesimal $d\lambda, d\ell$ in the last step. From this, the first order RG flow equation for the coupling λ follows

$$\frac{d\lambda}{d\ell} = -(K+1)\lambda. \tag{3.37}$$

At this point, several comments should be made. The first is the interpretation of the result Eq. (3.37). As $0 < K \leq 1$, the term $K+1$ is always positive and the right hand side prefactor of the flow equation is always negative. Integrating the flow equation, this means that for growing ℓ, λ has to shrink. In other words, if the short distance cutoff a gets increased, so only lower energies are taken into account, the coupling strength λ gets reduced. This is the characteristic of an irrelevant coupling[2]. However, it will be shown that the single-particle backscattering is a *dangerously irrelevant* coupling as it will generate other terms that turn out to be relevant. Second is that for a correct RG treatment, the coupling constant λ has to be dimensionless. This ensures that physical units stay independent during the procedure. Without this requirement, there would be more flexibility to choose λ, especially there would not be the need to put an additional a^{-2} dependence into its definition and this factor would appear in the RG flow equation and the prefactor would read $-(K-1)$ and could thus become positive.

For the second order in λ RG equations, one starts with the Eq. (3.31), which appears below a x_1, x_2, t_1, t_2 integral. It comes together with a prefactor $\lambda^2 a^2 a^{2K}$. Both parts depend on the cutoff a. To formalize this, the function $g(a)$ is defined by the right hand side of Eq. (3.31). So far, the exact dependency on a of $g(a)$ does not matter, $g(a)$ however is independent of λ. The RG step can be done already in this simple form and will read

$$\lambda^2 a^{2K+2} g(a) = (\lambda + d\lambda)^2 a^{2K+2} (1+d\ell)^{2K+2} g\left(a(1+\ell)\right), \tag{3.38}$$

where only the a dependence from the integrand was taken into account. Any dependence of the integral boundaries will be covered later. The linearization of this equation leads to

$$\lambda^2 g(a) = \lambda^2 g(a) + \lambda^2 (2K+2) d\ell g(a) + \lambda^2 g'(a) a d\ell + 2\lambda d\lambda g(a), \tag{3.39}$$

which is equivalent to

$$0 = \lambda(2K+2)g(a) + \lambda g'(a) a + 2\frac{d\lambda}{d\ell} g(a). \tag{3.40}$$

This expression contains the first order RG equation again, which makes two terms vanish. What remains is

$$0 = g'(a). \tag{3.41}$$

This is a condition that cannot be made true using only λ or ℓ[3]. That this term was generated means that the RG was not complete and an essential part is still missing. This term can only be canceled if a new term is generated in the Hamiltonian, which is zero in the beginning of the RG flow, but grows with growing ℓ. First, we examine the generated term a bit closer. The integration of Eq. (3.31) over x_2, t_2 can be approximated. As the operator product is normal ordered, it will not diverge anymore for $x_2 \to x_1$ and $t_2 \to t_1$. On the other hand, it is expected to drop exponentially for large $x_2 - x_1$ respectively

[2]The negative factor $-(K+1)$ is what defines that a coupling is irrelevant in the RG sense.

[3]Only for $\lambda = 0$, when this term would not exist. But this is the trivial limit.

$t_2 - t_1$. This suggests that it is a reasonable approximation to evaluate the second integral for $x_2 = x_1$ and $t_2 = t_1$ with the width ia^2/v_F. The factor i can be obtained from similar calculations where this integral can be done exactly. That it has to appear can be guessed because x_i and a always appear in the combination $a + i(x_2 - vt_2)$ in Eq. (3.31). The rest is determined by demanding the correct dimensions. With $x_2 = x_1, t_2 = t_1$, which implies that $\alpha = \beta$ to keep the operator expression, one obtains

$$\begin{aligned} g(a) \approx & \sum_\alpha \frac{8\pi^6}{L^6}\left(\frac{2a\pi}{L}\right)^{2K} e^{2a\pi/L}\left(e^{2a\pi/L}-1\right)^{-6} {}^*_*\, e^{i\alpha 4\phi(x_1,t_1)}\, {}^*_* \\ & \times\left[-e^{6a\pi/L}+e^{4a\pi/L}(4K-3)+K-e^{2a\pi/L}(1-6K+2K^2)\right] \\ = & \frac{16\pi^6}{L^6}\left(\frac{2a\pi}{L}\right)^{2K} e^{2a\pi/L}\left(e^{2a\pi/L}-1\right)^{-6} {}^*_* \cos\left(4\phi(x_1,t_1)\right) {}^*_* \\ & \times\left[-e^{6a\pi/L}+e^{4a\pi/L}(4K-3)+K-e^{2a\pi/L}(1-6K+2K^2)\right]. \end{aligned} \tag{3.42}$$

Linearization for $a \to a(1 + d\ell)$ and keeping only the lowest order terms in a/L yields

$$g(a) \approx -\frac{1}{8a^6}\left(\frac{2a\pi}{L}\right)^{2K}\left[1+2d\ell(K-3)\right]\left(5-11K+2K^2\right) {}^*_* \cos\left(4\phi(x_1,t_1)\right) {}^*_*. \tag{3.43}$$

The K-dependent factor can still be written in a nicer way, $(5-11K+2K^2) = (2K-1)(K-5)$. With this, the extra term that is generated in second order reads

$$Z_c = \frac{i\lambda^2 v_F}{4a^2}\left(\frac{2\pi a}{L}\right)^{4K}\int dx_1 \int_{-\infty}^{\infty} dt_1 d\ell(K-3)(2K-1)(K-5)\langle {}^*_* \cos\left(4\phi(x_1,t_1)\right) {}^*_*\rangle_0. \tag{3.44}$$

This equation contains an operator which can be used for an educated guess on the term that is generated. In first order expansion, it should contain the operator ${}^*_* \cos\left(4\phi(x_1,t_1)\right) {}^*_*$. Furthermore, there is a factor of a^{4K-2}. To cancel this term, an umklapp term (sine-Gordon term) is added to the Hamiltonian of the form

$$H_{\rm um} = \frac{v_F}{L^2}\underbrace{\frac{\tilde{V}_{\rm um}}{v_F a^2}}_{g_{\rm um}}\left(\frac{2\pi a}{L}\right)^{4K-2}\int dx\, {}^*_* \cos[4\phi(x) - 4k_F x]\, {}^*_* \tag{3.45}$$

where $g_{\rm um}$ is dimensionless and $k_F = 0$. This term in first order RG should cancel the generated term. To see this we treat this term in first order RG. Expanding the partition function

$$\begin{aligned} Z_{um} &= Z_{0,um} - i\int_{-\infty}^{\infty} dt \langle H_{um}(t)\rangle_0 \\ &= Z_{0,um} - i\frac{v_F}{L^2} g_{\rm um}\left(\frac{2\pi a}{L}\right)^{4K-2}\int dx \int_{-\infty}^{\infty} dt \langle {}^*_* \cos[4\phi(x)]\, {}^*_*\rangle_0 \end{aligned} \tag{3.46}$$

and changing the cutoff and coupling constant $g_{\rm um} \to g_{\rm um} + dg_{\rm um}$, $a \to a(1 + d\ell)$. This must not only fulfill this first order RG equation, but also cancel the additional term Z_c

that was generated above. For clarity, the whole thing written down explicitly reads

$$\begin{aligned}
&-i\frac{v_F}{L^2}g_{\mathrm{um}}\left(\frac{2\pi a}{L}\right)^{4K-2}\int dx\int_{-\infty}^{\infty}dt\langle {}^{*}_{*}\cos[4\phi(x)-4k_Fx]{}^{*}_{*}\rangle_0\\
=&-i\frac{v_F}{L^2}\left(g_{\mathrm{um}}+dg_{\mathrm{um}}\right)\left(\frac{2\pi a}{L}\right)^{4K-2}\left(1+(4K-2)d\ell\right)\int dx\int_{-\infty}^{\infty}dt\langle {}^{*}_{*}\cos[4\phi(x)]{}^{*}_{*}\rangle_0\\
&+\frac{i\lambda^2v_F}{4a^2}\left(\frac{2\pi a}{L}\right)^{4K}\int dx_1\int_{-\infty}^{\infty}dt_1d\ell(K-3)(K-5)(2K-1)\langle {}^{*}_{*}\cos\left(4\phi(x_1,t_1)\right){}^{*}_{*}\rangle_0.
\end{aligned}\tag{3.47}$$

From this the following equation can be extracted

$$\begin{aligned}
&\frac{1}{L^2}\left(dg_{\mathrm{um}}+g_{\mathrm{um}}(4K-2)d\ell\right)\left(\frac{2\pi a}{L}\right)^{4K-2}\\
=&\frac{\lambda^2}{4a^2}\left(\frac{2\pi a}{L}\right)^{4K}(K-3)(K-5)(2K-1)d\ell.
\end{aligned}\tag{3.48}$$

Which is rewritten as

$$\frac{dg_{\mathrm{um}}}{d\ell}=-2g_{\mathrm{um}}(2K-1)+\lambda^2\pi^2(K-3)\left(2K-1\right)\left(K-5\right).\tag{3.49}$$

Please note that this expression does not depend on a (this is not trivial). This indicates that the right dimensionless coupling constants have been chosen before. If a dependency on a remained in the RG flow equation, it would mean that the differential equation for g_{um} depends on the initial condition a, the cutoff which the RG flow starts from. At the first glance, it may be a bit strange that Eq. (3.49) does not vanish in the non-interacting limit for $K=1$. However, a closer look reveals that in that limit $\lambda=0$ and, by construction, $g_{\mathrm{um}}(\ell=0)=0$. So $g_{\mathrm{um}}(\ell)=0$ in the $K=1$ case. The two special points $K=3,5$ for which the inhomogeneous part of the equation vanishes are not of interest here, as they require attractive interactions, $K>1$. The point $K=1/2$ though, is worth discussing. At this point, $g_{\mathrm{um}}(\ell)=0$ and umklapp scattering is a marginal perturbation. For larger $1/2<K<1$, the left-hand side of Eq. (3.49) is always negative and umklapp scattering stays irrelevant. For strong repulsive interactions $K<1/2$, umklapp scattering turns out to be a relevant perturbation. This is the interesting limit that this chapter will build on in the following.

As furthermore $\lambda(\ell)$ will flow with ℓ, the RG flow of g_{um} is not trivial. It is plotted for some values of K in Fig. 3.1 In the regime $1/2<K<1$ it first increases, due to the finite initial condition of λ, and then drops to 0 as it gets suppressed by the $-2g_{\mathrm{um}}(2K-1)$ term. For $K<1/2$, the λ contribution dies out fast, but then an exponential increase is activated, caused by the g_{um} proportional term. For that regime, umklapp scattering was created as a relevant perturbation, caused by the dangerously irrelevant single-particle backscattering terms. The coupling g_{um} will flow towards the strong coupling fixed point. The field ϕ will be pinned to one of the minima of the $\cos(4\phi)$ term in Eq. (3.45).

In the following, we will argue that the generated umklapp scattering furthermore leads to a gap in the edge state spectrum. Using the initial conditions $\lambda(\ell=0)=\lambda_0$ and $g_{\mathrm{um}}(\ell=0)=0$ the RG flow equations can be solved. The solution reads

$$\begin{aligned}
\lambda(\ell)&=\lambda_0e^{-(K+1)\ell}\\
g_{\mathrm{um}}(\ell)&=-\frac{(2K-1)\gamma\lambda_0^2}{8-4K}e^{(2-4K)\ell}\left(e^{2(K-2)\ell}-1\right)\approx-\frac{(1-2K)\gamma\lambda_0^2}{8-4K}e^{(2-4K)\ell}
\end{aligned}\tag{3.50}$$

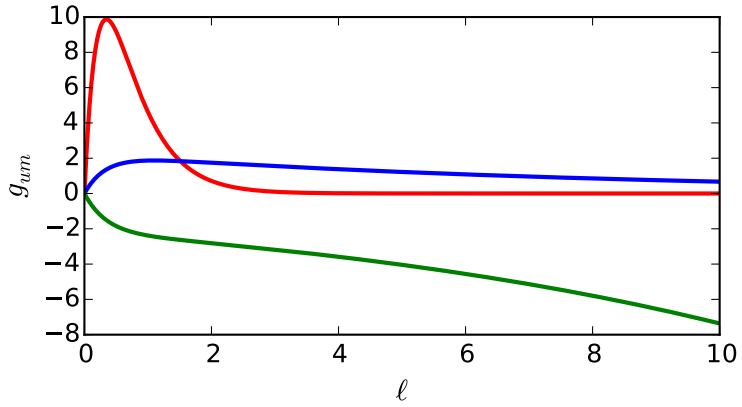

Figure 3.1: Solution of the RG flow equation for $g_{\rm um}$. The initial condition for λ was chosen as $\lambda(\ell = 0) = 1$. The solution is shown for $K = 1$ (red), $K = 0.53$ (blue) and $K = 0.47$ (green). While the solutions for $K > 1/2$ approach 0 for large ℓ, the one for $K < 1/2$ escapes to $-\infty$ and the perturbation is therefore relevant.

with the shorthand notation $\gamma := 2\pi^2(5-K)(3-K)$ and in the last line the approximation $\ell \gg 1$ was taken to show the asymptotic behavior for $K < 2$. The bare coupling constant was defined by

$$\lambda_0 = \frac{12U_0}{\pi^2 v_F k_0^2 a^2}, \tag{3.51}$$

where the cutoff a should be given by the inverse of the bulk band gap. For a system with large size L and at zero temperature, the RG flow can be continued until $\left|g_{\rm um}(\ell^*)\right| \approx 1$ as there is no other scale that would stop the flow. This leads to

$$e^{\ell^*} = \left(\frac{8-4K}{(1-2K)\gamma\lambda_0^2}\right)^{1/(2-4K)}. \tag{3.52}$$

The next step is to estimate the energy gap created in the spectrum by the umklapp term. The Hamiltonian with umklapp term is approximated as follows,

$$\begin{aligned} H &= \int dx \left\{ \frac{vK}{2\pi}[\partial_x\theta(x)]^2 + \frac{v}{2\pi K}[\partial_x\phi(x)]^2 + \frac{vg_{\rm um}}{a^2}\cos[4\phi(x)] \right\} \\ &\approx \int dx \left\{ \frac{vK}{2\pi}[\partial_x\theta(x)]^2 + \frac{v}{2\pi K}[\partial_x\phi(x)]^2 - \frac{8vg_{\rm um}}{a^2}\phi^2(x) \right\}. \end{aligned} \tag{3.53}$$

In order to estimate the gap, one can proceed as in Ref. [Giamarchi03], see the Eq. (2.153). The idea is to write down the action in Fourier space and identify the energy cost on an excitation with momentum zero. The gap is found to be of the order

$$M = \frac{4v}{a}\sqrt{\pi K|g_{\rm um}|}. \tag{3.54}$$

Therefore, at the end of the RG flow when $|g_{\rm um}(\ell^*)| = 1$ one has $M(\ell^*) \approx 4\sqrt{\pi K}v/a$. The true gap of the system is then of the order

$$M(\ell = 0) \approx e^{-\ell^*}\frac{v}{a} = \frac{v}{a}\left(\frac{(1-2K)\gamma\lambda_0^2}{8-4K}\right)^{1/(2-4K)}. \tag{3.55}$$

To obtain numerical values for this, one first has to estimate the bare λ_0. Using Eq. (3.20) to express U_0/v_F in terms of K (although strictly speaking Eq. (3.20) is only correct for weak interactions),

$$\frac{2U_0}{\pi v_F} = \frac{1}{K^2} - 1 \tag{3.56}$$

which leads to

$$\lambda_0 = \frac{6}{\pi k_0^2 a^2}\left(\frac{1}{K^2} - 1\right). \tag{3.57}$$

The single-particle backscattering strength is thus determined by the dimensionless parameters K and $k_0 a$. It seems reasonable to use $1/a \approx 0.01/\text{Å}$ [Qi11] and $K = 0.4$. The parameter $k_0 a$ is harder to estimate. Assuming that the spin axis rotation is very weak, e.g., $k_0 a \approx 10$. This leads to

$$\lambda_0 = \frac{6}{\pi(10)^2}\left(\frac{1}{0.4^2} - 1\right) \approx 1 \times 10^{-3}. \tag{3.58}$$

This result yields for $v \approx 5.5 \times 10^5 \text{m/s}$ and $a \approx 100\text{Å}$,

$$M(\ell = 0) \approx \frac{v}{a}\left(\frac{2\pi^2(5-K)(3-K)(1-2K)\lambda_0^2}{8-4K}\right)^{1/(2-4K)} \approx 3.9\,\text{Kelvin} = 0.24\,\text{meV}. \tag{3.59}$$

The equation however suggests that this value scales strongly with λ_0 and K, which are both quantities for which no good numerical values are accessible. Yet the necessary parameters seem to be close to those that are achievable in modern experiments.

3.3 Interface bound states

In the last section, we established the basics to investigate a more complicated setup. Figure 3.2 shows the edge of a 2D topological insulator with alternating superconducting (blue) and Mott insulating (green) regions. These regions can be formed for example by gates or adjacent superconducting materials. The superconductors induce a superconducting pairing which gaps the corresponding topological insulator edge states. In the same way, the strong interaction that is present in the green regions leads to a gap, which forms the Mott insulating areas. At the interfaces bound states emerge. In this section, a single interface between two such regions is examined analytically.

The full Hamiltonian in the bosonized form of a single interface is given by an interacting Luttinger liquid Hamiltonian over the whole system length and a strongly interacting part for $x > 0$ and a part with induced superconductivity for $x < 0$. The interaction strength K and sound velocity v are spatially dependent, but assumed to be constant at least within each region $x \gtrless 0$. They are defined as $K(x) = K_M\Theta(x) + K_S\Theta(-x)$ and $v(x) = v_M\Theta(x) + v_S\Theta(-x)$ with the step-function $\Theta(x)$. For simplicity, the regions are assumed to extend to $\pm\infty$. The Hamiltonian reads

$$\begin{aligned} H = &\frac{1}{2\pi}\int_{-\infty}^{\infty} dx \left\{ v(x)K(x) \,{}^{*}_{*}\, [\partial_x\theta(x)]^2 \,{}^{*}_{*} + \frac{v(x)}{K(x)} \,{}^{*}_{*}\, [\partial_x\phi(x)]^2 \,{}^{*}_{*} \right\} \\ &+ \tilde{\Delta}\int_{-\infty}^{0} dx \sin[2\theta(x)] + \tilde{g}_{um}\int_{0}^{\infty} dx \cos[4\phi(x)], \end{aligned} \tag{3.60}$$

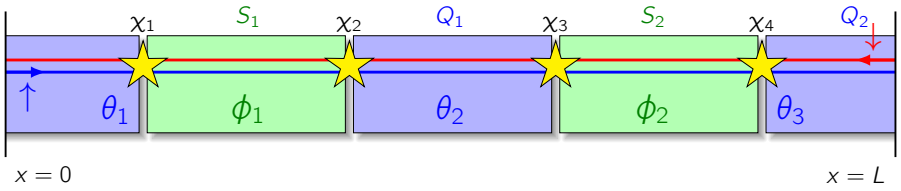

Figure 3.2: Alternating Mott insulating and superconducting regions (green and blue sections) with periodic boundary conditions. The fields ϕ and θ are pinned in the superconducting (θ_i) and Mott insulating (ϕ_i) sections. There are four emergent bound states, labeled by χ_i. The two helical edge states are indicated by the thin red and blue line.

where the induced superconducting pairing ($\tilde{\Delta} = \Delta/(\pi a)$) and umklapp scattering ($\tilde{g}_{\mathrm{um}} = v_F g_{\mathrm{um}}/a^2$) were discussed in the last section. All possible constant phases inside the cosine and sine functions were dropped as they can be compensated by a redefinition of the fields. It was shown already that the $\cos(4\phi)$ term is relevant for $K_M < 1/2$. In an alike way, it can be shown that the $\sin(2\theta)$ term is relevant as well within its region for $K_S > 1/2$ only [Gangadharaiah11]. For large enough $\tilde{\Delta}$ and $\tilde{g}_{\mathrm{um}}$, both terms pin the fields θ and ϕ within each region to the minima of the sin and cos potentials.

Despite this evident contradiction, $K_S > 1/2$, $K_M < 1/2$ inside the same topological insulator, an experimental realization can be possible. Assuming a topological insulator with a natural $K < 1/2$. Then, the proximity to a superconductor can lead to a strong screening of interactions, effectively increasing K inside the region with induced superconductivity to a value $K_S > 1/2$. For example an interacting helical liquid that interacts with a nearby superconductor with interaction strength $U_{sc}(x) = U_{sc}\delta(x)$ will increase K from K_M to $K_S = K_M[1 - K_M^2 U_{sc}^2/(\pi v_M)^2]^{-1/2} > K_M$ (supplemental material of [Orth15a]).

The pinning of the fields to the minima of the cosine and sine functions allows to use a mean-field approximation. In this, the term $\cos(4\phi(x))$ is expanded around one of the minima $\phi_m = \langle\phi(x)\rangle = (2m+1)\pi/4$ for $x > 0$. In the same sense, θ is expanded as $\theta_n = (n + 1/2)\pi$ around the minima of the sine term for $x < 0$. In principle, tunneling between the different minima is possible, but it is suppressed by the order of the system length L and temperature T. This effect is therefore neglected henceforth. The fields are redefined to minimize the potentials by

$$\begin{aligned} \theta(x) &\to \theta(x) + \theta_n \\ \phi(x) &\to \phi(x) + \phi_m, \end{aligned} \tag{3.61}$$

which leaves the kinetic part of the Hamiltonian invariant and the commutator $[\phi(x), \partial_y\theta(y)] = i\pi\delta(x-y)$ still holds. Expansion around $\theta \approx 0$ and $\phi \approx 0$ leads to the quadratic Hamiltonian

$$\begin{aligned} H =& \frac{1}{2\pi}\int dx \left\{ v(x)K(x)[\partial_x\theta(x)]^2 + \frac{v(x)}{K(x)}[\partial_x\phi(x)]^2 \right\} \\ &+ 2\tilde{\Delta}\int_{x<0} dx[\theta(x)]^2 + 8\tilde{g}_{\mathrm{um}}\int_{x>0} dx[\phi(x)]^2, \end{aligned} \tag{3.62}$$

where constant terms have been dropped.

3.3.1 A differential equation for Green's functions

The following steps transform this Hamiltonian to a form that allows extraction of a differential equation for the Green's functions. Using the canonical momentum $\Pi(x) =$

$\partial_x\theta(x)/\pi$ the real-time action can be derived as

$$\mathcal{S}[\theta,\phi] = \int dtdx \left[(\partial_t\phi)\Pi - \mathcal{H}\right]. \tag{3.63}$$

The corresponding action in imaginary time is given by using the analytic continuation. Defining $S = -i\mathcal{S}|_{t\to -i\tau}$, we find

$$\begin{aligned} S[\theta,\phi] &= (-i)^2 \int d\tau dx \left[i(\partial_\tau\phi)\Pi - \mathcal{H}\right] \\ &= \int d\tau dx \left[-i(\partial_\tau\phi)\Pi + \mathcal{H}\right], \end{aligned} \tag{3.64}$$

where $\mathcal{H}$ is the Hamiltonian density. Note that this is the *Hamiltonian* action, so it depends on both ϕ and θ [Altland10]. Usually, it is possible to perform the path integral over $\theta(x)$, and thus obtain the Lagrangian action, which depends only on $\phi(x)$. However, here the action depends explicitly on $\theta(x)$, so this is not so easy. It is therefore expedient to stick to the Hamiltonian representation.

Introducing x-dependent pairing amplitudes $\tilde{\Delta}(x)$ (interaction strength $\tilde{g}_{\rm um}(x)$) which vanish in the interaction region (superconducting region), we write the action as

$$\begin{aligned} S[\theta,\phi] = \int d\tau dx \Big\{ &- \frac{i(\partial_\tau\phi)(\partial_x\theta)}{\pi} + \frac{v(x)K(x)}{2\pi}[\partial_x\theta(x)]^2 + \frac{v(x)}{2\pi K(x)}[\partial_x\phi(x)]^2 \\ &+ 2\tilde{\Delta}(x)\theta^2(x) + 8\tilde{g}_{\rm um}(x)\phi^2(x)\Big\}. \end{aligned} \tag{3.65}$$

Furthermore, integration by parts yields,

$$\begin{aligned} S[\theta,\phi] = &\frac{1}{2\pi}\int d\tau dx \Big\{ 2i\phi\partial_\tau\partial_x\theta - \theta(x)\partial_x[v(x)K(x)\partial_x]\theta(x) - \phi(x)\left[\partial_x\frac{v(x)}{K(x)}\partial_x\right]\phi(x) \\ &+ 4\pi\tilde{\Delta}(x)\theta^2(x) + 16\pi\tilde{g}_{\rm um}(x)\phi^2(x)\Big\}. \end{aligned} \tag{3.66}$$

Under the integral, the first term can be written as $2\phi\partial_\tau\partial_x\theta = \phi\partial_\tau\partial_x\theta + \theta\partial_\tau\partial_x\phi$. With the vector notation

$$\Phi = \begin{pmatrix}\phi(x)\\ \theta(x)\end{pmatrix} \tag{3.67}$$

the action finally becomes

$$S[\Phi] = \frac{1}{2\pi}\int d\tau dx \Phi^T D\Phi \tag{3.68}$$

where

$$D = \begin{pmatrix} -\partial_x\frac{v(x)}{K(x)}\partial_x + 16\pi\tilde{g}_{\rm um}\Theta(x) & i\partial_\tau\partial_x \\ i\partial_\tau\partial_x & -\partial_x v(x)K(x)\partial_x + 4\pi\tilde{\Delta}\Theta(-x)\end{pmatrix}. \tag{3.69}$$

Therefore, the differential equation for the imaginary-time Green's function

$$G(x,x',\tau,\tau') = -\langle T_\tau\Phi(x,\tau)\Phi(x',\tau')\rangle \tag{3.70}$$

which should be interpreted as a 2×2 matrix in (ϕ, θ) space, is given by

$$DG(x, x', \tau, \tau') = \delta(x - x')\delta(\tau - \tau'). \tag{3.71}$$

The procedure in the following will be as this: first, we shall derive a solution to this differential equation separately for the Mott insulating and the superconducting region. The solutions are finally matched to find the Green's function for the interface. A subsequent refermionization allows to gain information on the bound states at the interface.

3.3.2 Green's functions in the strongly interacting region

In this subsection, we will derive the solution to the differential equation

$$\begin{pmatrix} -\frac{v_M}{K_M}\partial_x^2 + 16\pi\tilde{g}_{\mathrm{um}} & i\partial_\tau\partial_x \\ i\partial_\tau\partial_x & -v_M K_M \partial_x^2 \end{pmatrix} G(x, x', \tau, \tau') = \delta(x - x')\delta(\tau - \tau'). \tag{3.72}$$

The starting point is an Ansatz for the homogeneous part, meaning a solution for $x \neq x'$. For simplicity, set $x' = \tau' = 0$. To find an ansatz, the following Fourier transform is useful

$$G^{L/R}(x, \tau) = \frac{1}{L\beta} \sum_k \sum_{\omega_n} e^{-i\omega_n \tau} e^{ikx} G^{L/R}(k, i\omega_n), \tag{3.73}$$

where L (R) means $x < 0$ $(x > 0)$. This yields

$$\begin{pmatrix} \frac{v_M}{K_M}k^2 + 16\pi\tilde{g}_{\mathrm{um}} & i\omega_n k \\ i\omega_n k & v_M K_M k^2 \end{pmatrix} G^{L/R}(k, i\omega_n) = 0. \tag{3.74}$$

These four equations can be solved in a non-trivial way only for some values of k. One possibility is $k = 0$, which leads to

$$\begin{aligned} 16\pi\tilde{g}_{\mathrm{um}} G^{L/R}_{\phi\phi}(0, i\omega_n) &= 0 \\ 16\pi\tilde{g}_{\mathrm{um}} G^{L/R}_{\phi\theta}(0, i\omega_n) &= 0 \end{aligned}$$

but does not give any restriction on the components $G^{L/R}_{\theta\phi}(0, i\omega_n), G^{L/R}_{\theta\theta}(0, i\omega_n)$. Another solution is for $k \neq 0$, which yields the conditions

$$\begin{aligned} k_\pm &= \pm\frac{1}{v_M}\sqrt{-16\pi\tilde{g}_{\mathrm{um}} K_M v_M - w_n^2} \\ G^{L/R}_{\theta\phi}(k_\pm, i\omega_n) &= -i\frac{\omega_n}{v_M K_M k_\pm} G^{L/R}_{\phi\phi}(k_\pm, i\omega_n) \\ G^{L/R}_{\theta\theta}(k_\pm, i\omega_n) &= -i\frac{\omega_n}{v_M K_M k_\pm} G^{L/R}_{\phi\theta}(k_\pm, i\omega_n). \end{aligned} \tag{3.75}$$

These are the only values of k with a non-trivial solution. Inserting these three solutions into Eq. (3.73) we find the Ansatz (staying in the ω_n picture)

$$\begin{aligned}
G^{L/R}_{\phi\phi}(x,i\omega_n) =& \frac{1}{L}e^{ik_+x}G^{L/R}_{\phi\phi}(k_+,i\omega_n)+\frac{1}{L}e^{ik_-x}G^{L/R}_{\phi\phi}(k_-,i\omega_n)\\
G^{L/R}_{\theta\phi}(x,i\omega_n) =& -i\frac{\omega_n}{Lv_MK_Mk_+}e^{ik_+x}G^{L/R}_{\phi\phi}(k_+,i\omega_n)-i\frac{\omega_n}{Lv_MK_Mk_-}e^{ik_-x}G^{L/R}_{\phi\phi}(k_-,i\omega_n)\\
&+\frac{1}{L}G^{L/R}_{\theta\phi}(0,i\omega_n)\\
G^{L/R}_{\phi\theta}(x,i\omega_n) =& \frac{1}{L}e^{ik_+x}G^{L/R}_{\phi\theta}(k_+,i\omega_n)+\frac{1}{L}e^{ik_-x}G^{L/R}_{\phi\theta}(k_-,i\omega_n)\\
G^{L/R}_{\theta\theta}(x,i\omega_n) =& -i\frac{\omega_n}{Lv_MK_Mk_+}e^{ik_+x}G^{L/R}_{\phi\theta}(k_+,i\omega_n)-i\frac{\omega_n}{Lv_MK_Mk_-}e^{ik_-x}G^{L/R}_{\phi\theta}(k_-,i\omega_n)\\
&+\frac{1}{L}G^{L/R}_{\theta\theta}(0,i\omega_n).
\end{aligned}\tag{3.76}$$

It turns out to be essential at this point to take also the $k=0$ solutions into account. This can be verified as well by comparing the solution to a method that uses a direct inversion of the matrix D to obtain the Green's function. The first condition one has to demand is that the solution does not diverge for $x\to\pm\infty$. For small $i\omega_n$, meaning inside the bandgap, k_- is negative imaginary. This means that $e^{ik_-(\infty)}$ diverges. To circumvent this, one has to set $G^L_{\phi\phi}(k_+,i\omega_n)=0$, $G^R_{\phi\phi}(k_-,i\omega_n)=0$, $G^L_{\phi\theta}(k_+,i\omega_n)=0$, $G^R_{\phi\theta}(k_-,i\omega_n)=0$. This results in six unknown coefficients.

We derive four more equations from the full inhomogeneous differential equation by integrating it in a small interval around $x'=0$. This yields

$$\int_{-\epsilon}^{\epsilon}dx\begin{pmatrix}-\frac{v_M}{K_M}\partial_x^2+16\pi\tilde{g}_{\mathrm{um}} & \omega_n\partial_x\\ \omega_n\partial_x & -v_MK_M\partial_x^2\end{pmatrix}G(x,i\omega_n)=\mathbb{1}.\tag{3.77}$$

If G is bounded in this interval, the equation can be integrated to obtain the following relations

$$\begin{aligned}
-\frac{v_M}{K_M}\partial_x\left[G^R_{\phi\phi}(x,i\omega_n)-G^L_{\phi\phi}(x,i\omega_n)\right]_{x=0}+\omega_n\left[G^R_{\theta\phi}(x=0,i\omega_n)-G^L_{\theta\phi}(x=0,i\omega_n)\right]&=1\\
w_n\left[G^R_{\phi\phi}(x=0,i\omega_n)-G^L_{\phi\phi}(x=0,i\omega_n)\right]-v_MK_M\partial_x\left[G^R_{\theta\phi}(x,i\omega_n)-G^L_{\theta\phi}(x,i\omega_n)\right]_{x=0}&=0\\
-\frac{v_M}{K_M}\partial_x\left[G^R_{\phi\theta}(x,i\omega_n)-G^L_{\phi\theta}(x,i\omega_n)\right]_{x=0}+\omega_n\left[G^R_{\theta\theta}(x=0,i\omega_n)-G^L_{\theta\theta}(x=0,i\omega_n)\right]&=0\\
w_n\left[G^R_{\phi\theta}(x=0,i\omega_n)-G^L_{\phi\theta}(x=0,i\omega_n)\right]-v_MK_M\partial_x\left[G^R_{\theta\theta}(x,i\omega_n)-G^L_{\theta\theta}(x,i\omega_n)\right]_{x=0}&=1.
\end{aligned}\tag{3.78}$$

These are essentially two decoupled systems of equations, for the $\phi\phi$, $\theta\phi$ components and for the $\phi\theta$,$\theta\theta$ components. For simplicity one can focus on the first one only. Inserting the ansatz and demanding continuity of the Green's functions lead to the remaining unknowns. The continuity can be motivated because a jump in θ or ϕ would result in an unphysical accumulation of charge or current at $x=0$. Putting everything together leads finally to the Green's functions, which read

$$G_{\phi\phi}(x,i\omega_n)=\frac{K_M}{2v_Mk_+}e^{ik_+|x|}\tag{3.79}$$

$$G^{L/R}_{\theta\phi}(x,i\omega_n)=-i\,\mathrm{sign}(x)\frac{\omega_n}{2v_M^2k_+^2}e^{ik_+|x|}+\frac{1}{L}G^{L/R}_{\theta\phi}(0,i\omega_n).\tag{3.80}$$

Here, $G^{L/R}_{\theta\phi}(0, i\omega_n)$ are two x-independent integration constants which are coupled by the equation

$$G^R_{\theta\phi}(0, i\omega_n) - G^L_{\theta\phi}(0, i\omega_n) = i\frac{\omega_n L}{v_M^2 k_+^2}. \tag{3.81}$$

As k_+ is positive imaginary for energies $i\omega_n < \sqrt{16\pi\tilde{g}_{\mathrm{um}} K_M v_M}$ the solution decays exponentially for $x \neq x' = 0$. In the limit of large energies, it is a plane wave. Also the $\theta\phi$ components are non-zero.

3.3.3 Green's functions in the region with induced superconductivity

The methodology to calculate the Green's functions for a region with induced superconductivity is the same as was used in the last subsection for the Mott insulating regions. The differential equation reads

$$\begin{pmatrix} -\frac{v_S}{K_S}\partial_x^2 & i\partial_\tau\partial_x \\ i\partial_\tau\partial_x & -v_S K_S \partial_x^2 + 4\pi\tilde{\Delta} \end{pmatrix} G^S(x, x', \tau, \tau') = \delta(x - x')\delta(\tau - \tau'), \tag{3.82}$$

where the index S indicates the restriction to the superconducting region. Possible wave vectors are $k_S = 0$ and $k_{S,\pm} = \pm\frac{1}{v_S}\sqrt{-\tilde{\Delta}\frac{v_S}{K_S} - \omega_n^2}$. The ansatz for the Green's function reads

$$\begin{aligned} G^S_{\phi\phi}(x, i\omega_n) &= \frac{1}{L} e^{ik_{S-}x} G^S_{\phi\phi}(k_{S-}, i\omega_n) + \frac{1}{L} G^S_{\phi\phi}(0, i\omega_n) \\ G^S_{\theta\phi}(x, i\omega_n) &= i\frac{v_S}{K_S}\frac{k_{S-}}{\omega_n}\frac{1}{L} e^{ik_{S-}x} G^S_{\phi\phi}(k_{S-}, i\omega_n), \end{aligned} \tag{3.83}$$

where it was used already that the system of equations is decoupled, as in the last subsection. The calculation will stop at this point, as this is all that will be needed for the following and a purely superconducting system is of no interest here. What remains to do is use the proper boundary conditions and demand continuity of the Green's function and matching of the left/right solutions.

3.3.4 Green's functions of a Mott insulating/superconducting interface

The results of the two last subsections will be combined here to calculate the Green's function at the interface between a Mott insulating region and one with induced superconductivity. The interface is located at $x = 0$ and the ansatz for the left and right regions will be matched at the interface. Proper boundary conditions then lead to the correct Green's function. Again, for simplicity $x' = 0$. G^M denotes the Green's function in the Mott insulating area and G^S in the region with induced superconductivity. Eq. (3.71) is then integrated for small ϵ around $x = 0$ as follows

$$\begin{pmatrix} -\frac{v_M}{K_M}\partial_x & \omega_n \\ \omega_n & -v_M K_M \partial_x \end{pmatrix} G^M(x, i\omega_n)|_{x=0} - \begin{pmatrix} -\frac{v_S}{K_S}\partial_x & \omega_n \\ \omega_n & -v_S K_S \partial_x \end{pmatrix} G^S(x, i\omega_n)|_{x=0} = \mathbb{1}. \tag{3.84}$$

We insert the two different ansatz from the last subsection in this equation. Furthermore, divergencies at $\pm\infty$ have to be avoided. This will lead to a linear system of four

equations for the eight unknown components $G^M_{\phi\phi}(k_{M+}, i\omega_n)$, $G^M_{\phi\theta}(k_{M+}, i\omega_n)$, $G^M_{\theta\phi}(0, i\omega_n)$, $G^M_{\theta\theta}(0, i\omega_n)$, $G^S_{\phi\phi}(k_{S-}, i\omega_n)$, $G^S_{\phi\phi}(0, i\omega_n)$, $G^S_{\phi\theta}(k_{S-}, i\omega_n)$ and $G^S_{\phi\theta}(0, i\omega_n)$. The remaining four equations are obtained from demanding continuity of the Green's functions. The system of equations can be solved using a computer algebra system. The result reads (this is for $x = 0$ where the Mott Green's function is by construction the same as the superconducting Green's function)

$$G_{\phi\phi}(x=0, i\omega_n) = \frac{i}{\frac{\sqrt{-16\pi v_M K_M \tilde{g}_{\mathrm{um}} - \omega_n^2}}{K_M} - \frac{\omega_n^2}{\sqrt{-4\pi v_S K_S \tilde{\Delta} - K_S^2 \omega_n^2}}} \tag{3.85}$$

$$\begin{aligned} G_{\phi\theta}(x=0, i\omega_n) &= G_{\theta\phi}(x=0, i\omega_n) \\ &= \frac{K_M \omega_n}{K_M \omega_n^2 - \sqrt{-16\pi v_M K_M \tilde{g}_{\mathrm{um}} - \omega_n^2}\sqrt{-4\pi v_S K_S \tilde{\Delta} - K_S^2 \omega_n^2}} \end{aligned} \tag{3.86}$$

$$G_{\theta\theta}(x=0, i\omega_n) = \frac{i}{-\frac{K_M \omega_n^2}{\sqrt{-16\pi v_M K_M \tilde{g}_{\mathrm{um}} - \omega_n^2}} + \sqrt{-4\pi v_S K_S \tilde{\Delta} - K_S^2 \omega_n^2}}. \tag{3.87}$$

In principle, a solution is also possible for finite x, x', it will just be far more complex and exponentially suppressed for energies below the gap. The functions are continuous around $\omega_n = 0$. A physical interpretation of the Green's functions in the bosonic picture is not intuitive and does not reveal much about the bound states. Only that there is a non-vanishing solution at $\omega_n = 0$ for the diagonal parts $\phi\phi$ and $\theta\theta$.

3.3.5 Fermionic Green's function at the interface

The Green's function of Fermionic particles is in general distinct from the bosonic Green's function and ideally offers greater physical insight into the nature of the bound state at the interface. The same holds for the fermionic and bosonic density of states, which can be obtained from the Green's function. Both functions are connected through the bosonization identity. The bosonic Green's functions were calculated for the non-interacting fields ϕ and θ, so refermionization is straight forward. The imaginary time fermionic GF for right-movers is defined as

$$G_{RR}(x, x', \tau, \tau') = -\langle T_\tau \psi_R(x, \tau) \psi_R^\dagger(x', \tau') \rangle. \tag{3.88}$$

The first step is to use the bosonization identity and the important relation $\langle e^A \rangle = \exp\left[\frac{1}{2}\langle A^2 \rangle\right]$ which is valid because the system is still bilinear in the bosonized fields. This yields for $\tau > \tau'$ at at the interface with $x = x' = 0$

$$\begin{aligned} G_{RR}(x, x', \tau, \tau') &= -\frac{1}{2\pi a}\langle U_R U_R^\dagger e^{-i\varphi_R(\tau,x)} e^{i\varphi_R(\tau',x')} \rangle \\ &= -\frac{1}{2\pi a}\langle e^{-i\varphi_R(\tau,x)+i\varphi_R(\tau',x')} \rangle e^{\left[\varphi_R(\tau,x), \varphi_R(\tau',x')\right]/2} \\ &= -\frac{1}{2\pi a} e^{-\frac{1}{2}\langle \left[-\varphi_R(\tau,x)+\varphi_R(\tau',x')\right]^2 \rangle} e^{\left[\varphi_R(\tau,x), \varphi_R(\tau',x')\right]/2} \\ &= -\frac{1}{2\pi a} e^{-\frac{1}{2}\langle \varphi_R(\tau,x)^2 \rangle - \frac{1}{2}\langle \varphi_R(\tau',x')^2 \rangle + \langle \varphi_R(\tau,x)\varphi_R(\tau',x') \rangle}. \end{aligned} \tag{3.89}$$

This holds because we can write $\varphi_R(\tau, x) = \varphi_R(x + iv\tau)$, $\varphi_L(\tau, x) = \varphi_L(x - iv\tau)$, which allows to calculate the commutator. For $\tau < \tau'$ we find

$$G_{RR}(x, x', \tau, \tau') = \frac{1}{2\pi a} e^{-\frac{1}{2}\langle\varphi_R(\tau,x)^2\rangle - \frac{1}{2}\langle\varphi_R(\tau',x')^2\rangle + \langle\varphi_R(\tau',x')\varphi_R(\tau,x)\rangle}. \tag{3.90}$$

These two results can be combined into one for any τ, τ'

$$G_{RR}(x, x', \tau, \tau') = -\frac{1}{2\pi a}\mathrm{sign}(\tau - \tau') e^{-\frac{1}{2}\langle\varphi_R(\tau,x)^2\rangle - \frac{1}{2}\langle\varphi_R(\tau',x')^2\rangle + \mathrm{sign}(\tau-\tau')\langle T_\tau\varphi_R(\tau,x)\varphi_R(\tau',x')\rangle}. \tag{3.91}$$

To translate this into the bosonic Green's function one has to transform to the fields θ, ϕ. This is done by

$$\begin{aligned}\langle T_\tau\varphi_R(\tau, x)\varphi_R(\tau', x')\rangle &= \langle T_\tau\left[\phi(x,\tau) - \theta(x,\tau)\right]\left[\phi(x',\tau') - \theta(x',\tau')\right]\rangle \\ &= -G_{\phi\phi}(x, x', \tau, \tau') - G_{\theta\theta}(x, x', \tau, \tau') + G_{\phi\theta}(x, x', \tau, \tau') + G_{\theta\phi}(x, x', \tau, \tau').\end{aligned} \tag{3.92}$$

From now on, we will use the simplified notation $\tau' = 0$. Care has to be taken with respect to the Fourier transforms as the Green's functions are not ordinary diagonal Green's functions. Assuming the τ integration was restricted to the range $\int_{-\beta}^{\beta} d\tau$ one has the following Fourier transform

$$\begin{aligned} f(\tau) &= \frac{1}{\beta}\sum_{n=-\infty}^{\infty} e^{-i\pi n\tau/\beta} f(i\omega_n) \\ f(i\omega_n) &= \frac{1}{2}\int_{-\beta}^{\beta} d\tau f(\tau) e^{in\pi\tau/\beta} \\ \omega_n &= n\pi/\beta \end{aligned} \tag{3.93}$$

for the bosonic Green's function. This definitions are more general than the restriction to fermionic or bosonic Matsubara frequencies ($(2n+1)\pi/\beta$ or $2n\pi/\beta$) only and should give the correct result in both ways. With these transforms of the bosonic Green's function and the ordinary fermion Matsubara transformation for G_{RR} we obtain

$$\begin{aligned} G_{RR}(i\omega_n) &= \int_0^\beta d\tau e^{i\omega_n\tau} G_{RR}(\tau) \\ &= -\frac{1}{2\pi a}\int_0^\beta d\tau e^{i\omega_n\tau} e^{-\frac{1}{2}\langle\varphi_R(\tau)^2\rangle - \frac{1}{2}\langle\varphi_R(0)^2\rangle + \langle T_\tau\varphi_R(\tau)\varphi_R(0)\rangle} \\ &= -\frac{1}{2\pi a} e^{-\langle\varphi_R(0)^2\rangle}\int_0^\beta d\tau e^{i\omega_n\tau} e^{-G_{\phi\phi}(\tau) - G_{\theta\theta}(\tau) + G_{\phi\theta}(\tau) + G_{\theta\phi}(\tau)} \\ &= -\frac{1}{2\pi a} e^{-\langle\varphi_R(0)^2\rangle}\int_0^\beta d\tau e^{i\omega_n\tau} e^{\frac{1}{\beta}\sum_{m=-\infty}^{\infty} e^{-i\pi m\tau/\beta}\left[-G_{\phi\phi}(i\omega_m) - G_{\theta\theta}(i\omega_m) + G_{\phi\theta}(i\omega_m) + G_{\theta\phi}(i\omega_m)\right]}. \end{aligned} \tag{3.94}$$

During the calculation it was used that $\langle\varphi_R(\tau)^2\rangle$ is a τ independent constant because the system is time translation invariant.

Now, all of the ingredients are there needed to calculate the fermionic Green's function in principle. However, analytic evaluation of the integrals is hard to impossible. Before some numerical approximations are done that allow to evaluate the integrations to some

extent, a brief look on the other Green's function, G_{LL}, is useful. It will become clear immediately that all that has to be done to obtain G_{LL} is to change the sign of ϕ during the calculation. This leads instantly to

$$\begin{aligned} &G_{LL}(i\omega_n) \\ &= -\frac{1}{2\pi a} e^{-\langle\varphi_L(0)^2\rangle} \int_0^\beta d\tau e^{i\omega_n\tau} e^{\frac{1}{\beta}\sum_{m=-\infty}^{\infty} e^{-i\pi m\tau/\beta}\left[-G_{\phi\phi}(i\omega_m)-G_{\theta\theta}(i\omega_m)-G_{\phi\theta}(i\omega_m)-G_{\theta\phi}(i\omega_m)\right]}. \end{aligned} \tag{3.95}$$

The sum of bosonic Green's functions can be calculated using Eq. (3.85). One finds

$$\begin{aligned} &G_{\phi\phi}(i\omega_m) + G_{\theta\theta}(i\omega_m) - G_{\phi\theta}(i\omega_m) - G_{\theta\phi}(i\omega_m) \\ &= -\frac{2K_M\omega_m + \sqrt{16\pi\tilde{g}_{\mathrm{um}} v_M K_M + \omega_m^2} + K_M K_S \sqrt{4\pi\tilde{\Delta} v_S/K_S + \omega_m^2}}{K_M\omega_m^2 - K_S\sqrt{16\pi\tilde{g}_{\mathrm{um}} v_M K_M + \omega_m^2}\sqrt{4\pi\tilde{\Delta} v_S/K_S + \omega_m^2}}. \end{aligned} \tag{3.96}$$

This behaves to some part asymptotically as $1/m$ or as $1/|m|$ for large m. Separating these two cases and using that the sum runs from $-\infty$ to ∞ together with the fact that $\int_{m_0}^{\infty} \cos(x)/x\,\mathrm{d}x$ and $\int_{m_0}^{\infty} \sin(x)/x\,\mathrm{d}x$ converge for $m_0 > 0$ one can show that the sum converges. For $\tau = 0$, we find $\sum_m 1/|m| \to \infty$. This appears with a negative sign in the integral expression, which yields $e^{-\infty/\beta} \to 0$, the integrand vanishes. The function of Eq. (3.96) varies slowly with m for realistic parameters. For finite τ, it is instructive to numerically evaluate the function $\sum_{m=1}^{\infty} \cos(\pi\tau x)/x \approx \text{const} = 0$ for $\tau > 0.2$. A similar behaviour can also be found if the complete expression is evaluated numerically for realistic parameters. This suggests to approximate the integrand as $\int_0^\beta \mathrm{d}\tau e^{i\omega_n\tau}(1 - e^{-\tau/\beta})$. This finally leads to

$$\begin{aligned} G_{RR}(i\omega_n) &\propto \int_0^\beta \mathrm{d}\tau e^{i\omega_n\tau}\left(1 - e^{-\tau/\beta}\right) \\ &= \frac{1}{i\omega_n}\left(e^{i\omega_n\beta} - 1\right) - \frac{1}{i\omega_n - 1/\beta}\left(e^{i\omega_n\beta - 1} - 1\right) \\ &= -\frac{2}{i\omega_n}\delta_{n,odd} - \frac{1}{i\omega_n - 1/\beta}\left(e^{in\pi - 1} - 1\right) \end{aligned} \tag{3.97}$$

and with analytical continuation

$$G_{RR}(\omega) \propto -\frac{2}{\omega + i0_+} - \frac{1}{\omega + i0_+ - 1/\beta}\left(\pm e^{-1} - 1\right). \tag{3.98}$$

Where 0_+ is infinitesimal positive and $\delta_{n,odd}$ is 1 only if n is odd. The second contribution diverges for $\omega = 1/\beta$. It can be understood in some way as a reminiscent of the states at the edges of the band gap even though it is related here only to the inverse temperature β. The first term appears only for $n =$ odd, which is true only for fermionic Matsubara frequencies. It has a pole at $\omega = 0$ which is well inside the band gap of the gapped edge states. This single pole can be interpreted as the zero-energy bound state searched for in this chapter.

3.4 Ground states and bound state operators

In the last sections we showed how an umklapp scattering term is generated, how this umklapp scattering as well as induced superconductivity can lead to gaps in the edge

state spectrum of 2D topological insulators and finally, how zero-energy bound states are formed at the interfaces of such regions. In this and the following sections, we shall built on these results by introducing effective operators that act on the bound states and that will be used to implement a protocol to braid the states. It is found that the bound states fulfill parafermionic exchange statistics.

The system under consideration in this section consists of $2N^4$ alternating regions with an induced superconducting gap and a Mott insulating gap, illustrated in Fig. 3.2. The boundary conditions of this system are assumed to be periodic. An analog formalism was used in [Lindner12], which serves as a guideline for some parts of this section, even though it was derived for a rather different system based on fractional quantum hall edge states.

3.4.1 Ground state degeneracy

As a first step, the ground state and its degeneracy have to be discussed. This will be the space the bound states live in. Taken from Fig. 3.2, the system starts with a induced superconducting region between $x = 0$ and $x = x_1$ where the first interface is located, pinning the field $\theta(x) = \theta_1$ to the sine function of the Hamiltonian, which is of the form of Eq. (3.62). This is followed by a Mott insulating region between $x = x_1$ and $x = x_2$ which pins $\phi(x) = \phi_1$ and so on. The system ends again at length $x = L$ with the last superconducting region, which pins $\theta(x) = \theta_{N+1}$. In every Mott insulating region, the fields ϕ can be pinned to one out of four different minima. All of these lead to a ground state with the same energy. Straight forward counting would lead to 4^N different degenerate ground states. However, more care has to be taken. First, all transitions between the different minima due to a finite temperature or a finite length of the several regions are suppressed. These transitions would otherwise reduce the ground state degeneracy. The question remaining is to what extend the ground states are still coupled, keeping in mind that the fields do not commute, $[\phi(x), \theta(y)] = -i\pi\Theta(x - y)$.

To determine the ground state degeneracy from a more solid mathematical base, we construct the following operators

$$\begin{aligned} \pi S_i &= \theta_{i+1} - \theta_i, & \pi Q_i &= \phi_{i+1} - \phi_i, \\ \pi S_{tot} &= \theta(L^-) - \theta(0^+), & \pi Q_{tot} &= \phi(L^-) - \phi(0^+), \end{aligned} \tag{3.99}$$

for $i = 1, \ldots, N-1$. The positions 0^+ and L^- are to be understood to be infinitesimal larger than 0 and infinitesimal smaller than L. From bosonization theory, it is known that the derivative of $\phi(x)$ is related to the charge density operator. Therefore, Q_i can be associated with the charge in the i-th Mott insulating region. In the same way, S_i can be associated with the spin in the i-th superconducting region. These values are fixed together with the pinning of θ_i, ϕ_i as the Hamiltonian $\psi_\uparrow^\dagger(x)\psi_\downarrow^\dagger(x)$ of the induced superconductivity preserves the spin quantum number and umklapp scattering $\psi_\uparrow^\dagger(\partial_x\psi_\uparrow^\dagger)(\partial_x\psi_\downarrow)\psi_\downarrow$ preserves the charge quantum number. S_{tot} and Q_{tot} are the total spin and charge of the system (spins are measured in units of the electron spin $\hbar/2$ and charges in units of the electron charge e). While in each superconducting region the spin is preserved, the charge is conserved only by modulo 2. The same holds for the Mott insulating regions, in which the spin is conserved modulo 4. Moreover, the charge in the Mott insulating regions is quantized in half integers. This, at the first glance physically puzzling, statement can be made plausible already by also taking into account a second Mott insulating region

[4] So there are $2N$ interfaces.

which could host the second half of an electron. The only physical requirement is that Q_{tot} is quantized in integers. The half integer quantization originates in the fact that the umklapp term can be refermionized, which means expressed by fermionic operators again using the refermionization formula $\tilde{\psi}^\dagger_\pm \propto e^{\pm 2i\phi - \theta/2}$. The refermionization leads to $\cos(4\phi) \propto \tilde{\psi}^\dagger_+ \tilde{\psi}_- + \text{H.c.}$. Since $[N, \tilde{\psi}^\dagger_\pm(x)] = \tilde{\psi}^\dagger_\pm(x)/2$, with the particle number operator N, the new fermions carry the charge $e/2$ only.

With the help of the operators S_i, Q_i the following sets of operators are constructed

$$\begin{aligned}&\{e^{i\pi S_1/2}, \ldots, e^{i\pi S_{N-1}/2}, e^{i\pi S_{tot}/2}, e^{i\pi Q_{tot}}\},\\ &\{e^{i\pi Q_1}, \ldots, e^{i\pi Q_{N-1}}, e^{i\pi S_{tot}/2}, e^{i\pi Q_{tot}}\}.\end{aligned} \tag{3.100}$$

The Appendix B.5 shows that within one set all these operators commute with the Hamiltonian and with each other. Looking at the pinned fields θ_i and ϕ_i, one finds that all operators $e^{i\pi S_i/2}$, $e^{i\pi Q_i}$ have the four eigenvalues $1, i, -1, -i$. These correspond to the spins $s_i \in 0, 1, 2, 3$ and charges $q_i \in 0, \frac{1}{2}, 1, \frac{3}{2}$. The same holds for Q_{tot} and S_{tot}. Due to the vanishing commutation relations of the fields within the sets, all eigenvalues within one set are good quantum numbers. This essentially means that the ground state would be $4^{N-1} \times 4 \times 4 = 4^{N+1}$ times degenerate. This degeneracy can be understood as the internal degeneracy of the bosonized Hamiltonian. However, as mentioned already there are some physical constraints as well. Demanding a total integer charge, the degeneracy is reduced by a factor of 2. The same will restrict also the allowed total spin quantum numbers by an additional factor of 2. This way, the total ground state degeneracy would be 4^N. The same value is obtained, independent which set of operators was used. The states can be labeled for example by $|q_1, \ldots, q_{N-1}, s_{tot}, q_{tot}\rangle$ or $|s_1, \ldots, s_{N-1}, s_{tot}, q_{tot}\rangle$ where s_i (q_i) is the eigenvalue of $e^{i\pi S_i/2}$ ($e^{i\pi Q_i}$). In the special case of a single junction, the degeneracy is therefore fourfold.

3.4.2 Construction of bound state operators

In this subsection, we construct bound state operators that allow moving within the space spanned by the degenerate ground states. It will be shown that these operators follow $\mathbb{Z}_4$ parafermionic exchange statistics.

A closer examination reveals that the operators Q_j transfer spins between the adjacent sections, assuming one is working in the spin basis with quantum numbers s_i. This can be seen, because

$$\begin{aligned}e^{i\pi S_j/2} e^{i\pi Q_j} &= e^{-i\pi/2} e^{i\pi Q_j} e^{i\pi S_j/2}\\ e^{i\pi S_{j+1}/2} e^{i\pi Q_j} &= e^{i\pi/2} e^{i\pi Q_j} e^{i\pi S_{j+1}/2}\end{aligned} \tag{3.101}$$

therefore

$$\begin{aligned}e^{i\pi S_j/2} e^{i\pi Q_j} |s_j, s_{j+1}\rangle =& e^{-i\pi/2} e^{i\pi Q_j} e^{i\pi S_j/2} |s_j, s_{j+1}\rangle\\ =& e^{-i\pi/2} e^{i\pi Q_j} e^{i\pi s_j/2} |s_j, s_{j+1}\rangle\\ =& e^{i\pi(s_j-1)/2} e^{i\pi Q_j} |s_j, s_{j+1}\rangle.\end{aligned} \tag{3.102}$$

In words, this equation means that the eigenvalue of S_j for the state $e^{i\pi Q_j}|s_j, s_{j+1}\rangle$ is given by $s_j - 1$. On the other hand, the eigenvalue of S_{j+1} on the same state will be $s_{j+1} + 1$.

Using this, one can additionally construct raising and lowering operators in the same way as

$$\hat{S}_j = \prod_{k=j}^{N-1} e^{-i\pi Q_k}, \qquad \hat{Q}_j = \prod_{k=1}^{j} e^{i\pi S_k/2}. \tag{3.103}$$

These operators consecutively move a spin (charge) from the right (left) end of the sample to a certain segment j. A spin (charge) is therefore effectively created in that section. To create excitations with electronic quantum numbers, one has to combine these operators in the following way

$$\chi_{2j-1} = \hat{S}_j \hat{Q}_{j-1} T_Q T_S, \qquad \chi_{2j} = e^{i\pi/4} \hat{S}_j \hat{Q}_j T_Q T_S, \tag{3.104}$$

where T_Q and T_S increase the total charge and the total spin, respectively. They act on the states as $T_Q|q_{tot}\rangle = |(q_{tot}+1) \mod 2\rangle$ and $T_S|s_{tot}\rangle = |(s_{tot}+1) \mod 4\rangle$. $\hat{Q}_j$ is similar to a Jordan-Wigner string. It ensures the right anticommutation relations. To determine the properties of these operators, one needs the following commutation relation (for $n \in \mathbb{Z}_4$)

$$\begin{aligned} \hat{S}_j^n e^{i\pi S_j/2} &= e^{-in\pi/2} e^{i\pi S_j/2} \hat{S}_j^n \\ [\hat{S}_j, \hat{S}_k] &= 0 \end{aligned} \tag{3.105}$$

which follows from letting both sides act on the ground state basis. All other commutators are trivial, $[\hat{S}_j, e^{i\pi S_k/2}] = 0$ for $j \neq k$, and $[e^{i\pi S_j/2}, T_Q] = 0$ as well as $[\hat{S}_j, T_Q] = 0$. From this, we determine the properties of the operators. For example, the n-th power yields

$$\begin{aligned} \chi_{2j}^n &= e^{i\pi n/4} \left[\hat{S}_j T_Q \hat{Q}_j\right]^n = e^{i\pi n/4} T_Q^n \hat{Q}_{j-1}^n \left[\hat{S}_j e^{i\pi S_j/2}\right]^n \\ &= e^{i\pi n/4} T_Q^n \hat{Q}_{j-1}^n e^{-i\pi/2} e^{i\pi S_j/2} \hat{S}_j^2 e^{i\pi S_j/2} (\ldots)^{n-2} \\ &= e^{i\pi n/4} T_Q^n \hat{Q}_{j-1}^n e^{-i\pi/2} e^{-2i\pi/2} \left[e^{i\pi S_j/2}\right]^2 \hat{S}_j^3 e^{i\pi S_j/2} (\ldots)^{n-3} \\ &= e^{i\pi n/4} T_Q^n \hat{Q}_{j-1}^n e^{-i\pi/2 \sum_{k=1}^n k} \left[e^{i\pi S_j/2}\right]^n \hat{S}_j^n \\ &= e^{i\pi n/4} e^{-i\pi n(n+1)/4} T_Q^n \hat{Q}_j^n \hat{S}_j^n \\ &= e^{-i\pi n^2/4} T_Q^n \hat{Q}_j^n \hat{S}_j^n. \end{aligned} \tag{3.106}$$

A similar result holds also for the odd positions

$$\chi_{2j-1}^n = T_Q^n \hat{Q}_{j-1}^n \hat{S}_j^n. \tag{3.107}$$

The special case $n = 4$ therefore yields

$$\chi_{2j}^4 = \chi_{2j-1}^4 = 1. \tag{3.108}$$

This result reveals the special character of the constructed states and the operators that create them. Unlike Majorana Fermions, which are their own anti-particles and the squared of their creation operator gives unity, [Kitaev01], the χ operators yield unity

if taken to the power of 4. Furthermore, calculating the squared of these operators

$$\begin{aligned}
\chi_{2j}^2 &= -\left(\prod_{k=1}^{j} e^{i\pi S_k}\right)\hat{S}_j^2 \\
\chi_{2j-1}^2 &= \left(\prod_{k=1}^{j-1} e^{i\pi S_k}\right)\hat{S}_j^2 \\
\left[\chi_{2j}^2\right]^\dagger &= -[\hat{S}_j^2]^\dagger\left(\prod_{k=1}^{j} e^{-i\pi S_k}\right) = -\hat{S}_j^2\left(\prod_{k=1}^{j} e^{i\pi S_k}\right) = -e^{-4i\pi/2}\left(\prod_{k=1}^{j} e^{i\pi S_k}\right)\hat{S}_j^2 \\
&= \chi_{2j}^2 \\
\left[\chi_{2j-1}^2\right]^\dagger &= [\hat{S}_j^2]^\dagger\left(\prod_{k=1}^{j-1} e^{-i\pi S_k}\right) = \hat{S}_j^2\left(\prod_{k=1}^{j-1} e^{i\pi S_k}\right) = \left(\prod_{k=1}^{j-1} e^{i\pi S_k}\right)\hat{S}_j^2 \\
&= \chi_{2j-1}^2,
\end{aligned} \tag{3.109}$$

it is found that these are hermitian. To better understand these operators, it makes sense to have a look at the commutation relations between different operators as well. Assuming $j < k$ without loss of generality one calculates

$$\chi_{2j}^n\chi_{2k}^m = e^{-i\pi n^2/4}T_Q^n\left(\prod_{x=1}^{j} e^{in\pi S_x/2}\right)\hat{S}_j^n e^{-i\pi m^2/4}T_Q^m\left(\prod_{x=1}^{k} e^{im\pi S_x/2}\right)\hat{S}_k^m. \tag{3.110}$$

The important part of this expression (assuming $j < k$) is the following (all other operators commute with the following line),

$$e^{in\pi S_j/2}\underbrace{\hat{S}_j^n e^{im\pi S_j/2}}_{e^{-i\pi nm/2}e^{im\pi S_j/2}\hat{S}_j^n}e^{im\pi S_k/2}\hat{S}_k^m = e^{-i\pi nm/2}e^{im\pi S_j/2}e^{im\pi S_k/2}\hat{S}_k^m e^{in\pi S_j/2}\hat{S}_j^n. \tag{3.111}$$

This leads to

$$\chi_{2j}^n\chi_{2k}^m = e^{-i\pi nm/2}\chi_{2k}^m\chi_{2j}^n \tag{3.112}$$

and similarly $\chi_{2j-1}^n\chi_{2k-1}^m = e^{-i\pi nm/2}\chi_{2k-1}^m\chi_{2j-1}^n$. For the mixed commutators, one obtains the same result. Therefore, for $j < k$, one finds in general $\chi_j^n\chi_k^m = e^{-i\pi nm/2}\chi_k^m\chi_j^n$ for $j, k = 1, \ldots, 2N-2$. In particular, this means that these operators satisfy $\mathbb{Z}_4$ parafermionic exchange statistics,

$$\chi_j\chi_k = e^{-i\pi/2}\chi_k\chi_j \qquad (\text{for } j < k). \tag{3.113}$$

The main conclusions of this section can be summarized as follows. We found that a setup with periodic boundary conditions of $2N$ alternating regions with induced superconductivity or strong interactions has a ground state which is 4^N fold degenerate. Creation operators χ_k can be defined that create a particle with electronic quantum numbers at the interface k while the total energy is not altered. Instead, the operators χ_k allow transitions within the ground state manifold. Application of an operator χ_k is cyclic, in the sense that an application of 4 times the same operator leads back to the original ground

state, $\chi_k^4 = 1$. Non-trivial processes appear when several positions j, k are considered. In this case, the operators χ_j, χ_k follow parafermionic exchange statistics with a phase $\pm i\pi/2$. The created particles are always fixed to the interfaces, as an electronic particle isolated in a superconducting or Mott insulating region would increase the total energy. The following section will deepen the discussion on the bound states and show that they follow non-Abelian braiding relations.

3.5 Braiding operators

With regards to new technological applications of quantum physics and especially topological insulators, such as quantum computation, braiding operations on the states of a physical system become vital [Nayak08]. For example, particles that follow non-Abelian braiding statistics, referred to as non-Abelian anyons hereafter, can lead to quantum computation that can be protected from a certain kind of errors. Especially of interest are systems that support universal topological quantum computation [Freedman02].

In contrast to 3D, in 2D more complex symmetries of a many-body wavefunction with respect to interchange of two indistinguishable particles than just $\pm$ for bosons and fermions can exist. In both cases, an interchange can be understood as an adiabatic transformation of the system such that two particles exchange and the system ends up in exactly the same configuration as it was in before the exchange. During this exchange, which takes a certain time, the wavefunction acquires a phase. In 3D, this phase can only be $\pi/2$ or π, because two consecutive exchanges have to yield the same wavefunction again. There is no meaning of moving one particle around another, or rather, any such procedure can be mapped on the case where the particles do not move at all. This is different in 2D, the process of two particles exchanging twice can have non-trivial consequences for the wavefunction. This section should not introduce the notation, formalism and physical relevance of braiding any further but instead apply the general theory to the system discussed during this chapter and introduce a braiding scheme for the Hamiltonian of interest.

The system discussed so far was an effective 1D model. In 1D, braiding is not possible as two particles cannot be moved around each other or exchanged at all without touching each other. This issue can be solved by realizing that the 1D edge states live on a 2D plane. One can introduce artificial couplings to the Hamiltonian that extend the 1D model to a higher dimension. An example is a tunneling operator of the kind

$$H_{ij} = -t_{ij}\chi_i\chi_j^\dagger + \text{H.c.}, \tag{3.114}$$

which transfers a particle from the interface i to the interface j. Usually, these processes are exponentially suppressed, due to the large distances between the interfaces. However, one can imagine an advanced system geometry that employs gates to bring two interfaces closer together. Figure 3.3 illustrates such a setup. A 2D topological insulator (green), with movable edge states in the vertical direction, is put on top of several gates (blue). The topological insulator can be extended or shrunken in the vertical direction. The eight gates are used to locally switch the superconducting proximity effect on (dark blue) and off (light blue). If switched off, the edge states are supposed to be in the Mott insulating phase. Each interface between a region with induced superconductivity and a Mott insulating one hosts a bound state (yellow stars). By switching the gates on and off, the bound states can be moved along the edges of the topological insulator. For the initial setup, as in

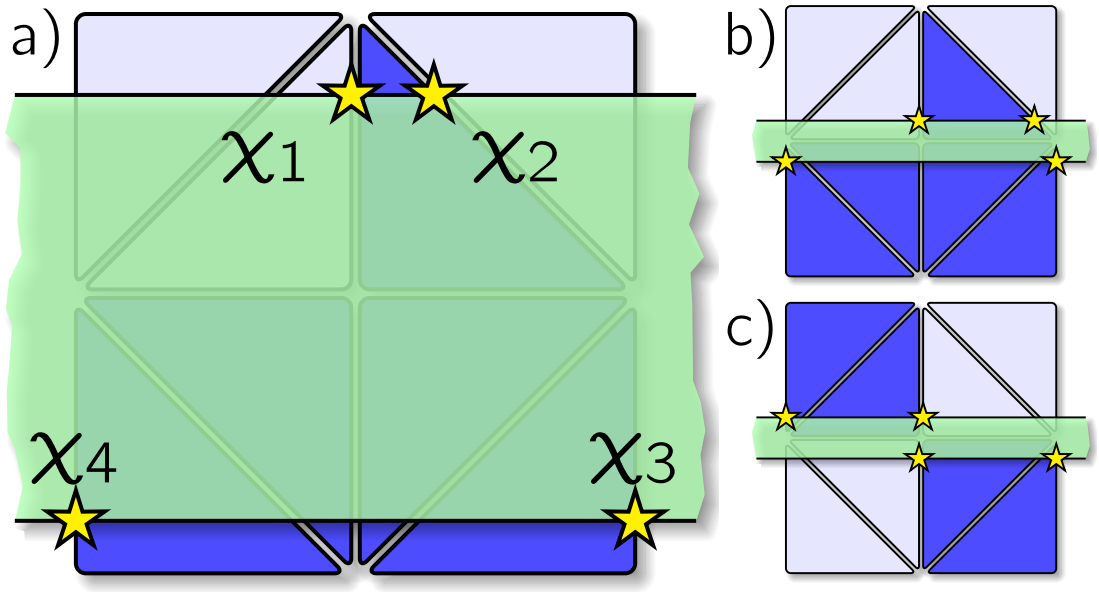

Figure 3.3: A 2D topological insulator which width can be tuned vertically (green) and eight gates for locally switching the proximity effect on (dark blue) and off (light blue). This allows the implementation of the braiding protocol for the bound states χ_i. In (a), the bound states χ_1 and χ_2 are coupled by a local tunneling Hamiltonian. It is furthermore possible to couple χ_2 and χ_3 or χ_2 and χ_4 by deforming the edge states, as shown in (b) and (c), respectively.

part a) of Fig. 3.3, the two states χ_1 and χ_2 are close together and coupled by a tunneling Hamiltonian

$$H_{12} = -t_{12}\chi_1\chi_2^\dagger + \text{H.c.}. \tag{3.115}$$

It is now possible to define a braiding scheme as follows

$$\begin{aligned} H_1 &= (1-\lambda_1)H_{12} + \lambda_1 H_{23}, \\ H_2 &= (1-\lambda_2)H_{23} + \lambda_2 H_{24}, \\ H_3 &= (1-\lambda_3)H_{24} + \lambda_3 H_{12}. \end{aligned} \tag{3.116}$$

Here, the tunnel Hamiltonians are defined as in Eq. (3.114). This scheme is used to braid the bound states χ_3 and χ_4. The variables $\lambda_{1/2/3}$ are varied in an adiabatic way to encode the transformation of the system Hamiltonian. Initially, $H_2 = H_3 = 0$ and $\lambda_1 = 0$. This way, only coupling between χ_1 and χ_2 is possible, as in Fig. 3.3 a). With an adiabatic increase of λ_1 from $0 \to 1$ tunneling between χ_2 and χ_3 is now possible, Fig. 3.3 b). The Hamiltonian is equivalent to H_2 for $\lambda_2 = 0$. Setting $H_1 = 0$ and letting $\lambda_2 \to 1$ finally couples χ_2 and χ_4. And as a last step, χ_1 and χ_2 are coupled again to return the system to the original setup, as it is important that the Hamiltonian in the first and last steps are identical.

To show that this protocol indeed is a prescription for non-Abelian braiding, one has to show that operators that implement the braiding operation satisfy the Yang-Baxter equations. This is a necessary and sufficient condition. This consideration was done in details in [Lindner12] for the edge states of a fractional quantum hall insulator and an

analogous calculation can be done for the setup considered in this chapter. It is again possible to define time evolution operators U_n that connect the initial and final states of all three steps, governed by H_1, H_2 and H_3. One finds that the initial and final states are connected through three phases $\gamma_n(s_3)$

$$U_n|\Psi_i^n(s_3)\rangle = e^{i\gamma_n(s_3)}|\Psi_f^n(s_3)\rangle, \tag{3.117}$$

for $n = 1, 2, 3$. Here, s_3 is the eigenvalue of the operator $e^{i\pi S_3/2}$. It is a good quantum number as this operator commutes with all tunneling Hamiltonians. A recursive equation for the phases can be derived and finally, one obtains the following expression for the evolution operator of a full braiding process

$$U_{34}|\Psi_i^1\rangle = \exp\left[\frac{i\pi}{4}(s_3 - s)^2\right]|\Psi_i^1\rangle, \tag{3.118}$$

where $s = s_1 + s_2 + s_3$. This shows that the braiding scheme changes the state only by a phase. A similar result is well known from exchanging Majorana bound states: for the four states $\gamma_{1,2,3,4}$ grouped into two fermions as $c_1 = \gamma_1 + i\gamma_2$ and $c_2 = \gamma_3 + i\gamma_4$, braiding γ_1 and γ_2 changes the wave function when expressed in the basis of eigenstates of $c_1^\dagger c_1$ and $c_2^\dagger c_2$, only by a phase. In contrast, braiding γ_2 and γ_3 would generate a nontrivial rotation in the four-dimensional ground state subspace.

This suggests that the operator U_{34} acts in a nontrivial way in a different basis, and indeed one finds

$$U_{34} = \frac{e^{i\pi/4}}{2}\sum_{p=0}^{3}\exp\left[-\frac{i\pi p^2}{4}\right]\left(\hat{Q}_1^\dagger\hat{Q}_2\right)^p \tag{3.119}$$

for the charge basis. The same method can be generalized to arbitrary interfaces, resulting in $U_{k,k'}$. With the help of commutation relations one arrives at

$$U_{2k-1,2k}U_{2k,2k+1}U_{2k-1,2k} = U_{2k,2k+1}U_{2k-1,2k}U_{2k,2k+1}, \tag{3.120}$$

whereas the operators commute if they do not involve nearest neighbors, $[U_{j,j+1}, U_{k,k+1}] = 0$ for $|j - k| > 1$. This completes the proof that the Yang-Baxter equations are satisfied. The equations basically state that the consecutive braiding of three states in the order $1 \leftrightarrow 2$, $2 \leftrightarrow 3$, $1 \leftrightarrow 2$ is the same as braiding in the order $2 \leftrightarrow 3$, $1 \leftrightarrow 2$, $2 \leftrightarrow 3$. That the braid group is non-Abelian is obvious because of $U_{2k-1,2k}U_{2k,2k+1} \neq U_{2k,2k+1}U_{2k-1,2k}$. Using combinations of nearest neighbor braiding operations, braiding for arbitrary interface bound states becomes possible.

The section is closed with a remark on the universality of the considerations above. The derivations require only that the adiabatic path that the Hamiltonian follows to accomplish a braid operation follows certain symmetries. It does not depend on the exact microscopic details of the Hamiltonian, and the results should therefore be applicable to a wide range of experimental realizations. The only important aspects are which interfaces couple at each stage of the process.

3.6 Josephson effect

The fact that charge is quantized in units of $e/2$ has an interesting effect on the Josephson effect. Considering a setup of two regions with induced superconductivity and a Mott

insulating region with length L in-between. The induced pairing amplitudes for the left and right superconductors are Δ_0 and $\Delta_0 e^{i\delta\phi_{SC}}$. Here, $2\Delta_0$ represents the superconducting gap induced in both superconducting regions at the chemical potential. Additionally, δ_{SC} labels the phase difference between the superconducting regions. Taking the limit $L \to \infty$ will prevent any tunneling and the fields are fixed to the four degenerate minima of the $\cos(4\phi)$ terms of the Mott insulator, see Eq. (3.60). The Josephson current vanishes. If the length L is finite, tunneling of quasiparticles with charge $e/2$ is possible. Section 3.4.1 contains an argument why the Mott regions show a half-integer quantization.

Tunneling of $e/2$ charges corresponds to tunneling between the four neighboring minimas of the $\cos(4\phi)$ potential. Assuming that the tunneling amplitude between all of the minimas is the same, t, and the superconducting phase difference can furthermore be absorbed into the tunneling amplitude by a gauge transformation, the tunneling Hamiltonian can be expressed as

$$\mathcal{H}_{JJ} = -\begin{pmatrix} 0 & te^{i\delta\phi_{SC}/4} & 0 & te^{-i\delta\phi_{SC}/4} \\ te^{-i\delta\phi_{SC}/4} & 0 & te^{i\delta\phi_{SC}/4} & 0 \\ 0 & te^{-i\delta\phi_{SC}/4} & 0 & te^{i\delta\phi_{SC}/4} \\ te^{i\delta\phi_{SC}/4} & 0 & te^{-i\delta\phi_{SC}/4} & 0 \end{pmatrix}. \tag{3.121}$$

This is to be understood in the basis $\phi = \{\pi/4, 3\pi/4, 5\pi/4, 7\pi/4\}$. Diagonalization of this Hamiltonian is straight forward and yields the eigenvalues $\pm 2t\cos(\delta\phi_{SC}/4), \pm 2t\sin(\delta\phi_{SC}/4)$. The Josephson current can then be calculated as $I_{JJ}(\delta\phi_{SC}) \propto d\langle\mathcal{H}_{JJ}\rangle/d\delta\phi_{SC}$. This shows that the Josephson current has a periodicity of 8π, as was found also in [Zhang14]. This is in contrast to the results of a periodicity of 4π as was found in [Fu09] for the simpler structure of an superconductor/quantum-spin-Hall-insulator/superconductor junction. Other related results were found also in [Clarke13] for fractional quantum Hall states with a $4m\pi$ periodicity, where $1/m$ is the filling factor.

3.7 Conclusions

In this chapter a novel physical setup was investigated which realizes non-Abelian parafermions. The system consists of a 2D topological insulator edge which is gapped out by alternating regions of strong interactions or superconductivity.

Effects such as structural inversion asymmetry or external electric fields lead to Rashba spin-orbit coupling in the topological insulator edge states. We showed that in combination with electron-electron interactions these effects generally lead to umklapp scattering. An RG treatment in the bosonized language was used to derive second order RG equations for the umklapp scattering Hamiltonian. Interestingly, it turns out that umklapp scattering becomes relevant for strong repulsive interactions, with Luttinger liquid parameter $K < 1/2$, even though the generating term stays irrelevant for all K. A gap is opened in the edge state spectrum.

On the other hand, if the edge states are in close proximity to a superconductor, a superconducting gap is induced in the edge state spectrum [Fu08, Hart14]. By refermionizing the bosonic Green's functions we could show that the interface between an edge state region gapped out by induced superconductivity and one gapped out by strong interactions host a zero energy bound state. This is encoded in a simple pole $G(\omega) \propto 1/(\omega + i\delta)$ in the fermionic interface Green's function.

Furthermore, we introduced a model that contains $2N$ of such alternating regions. The ground state degeneracy of this system was determined and we found it to be 4^N. The states can be labeled either by a set of spin quantum numbers or charge quantum numbers. In the latter case, however, it turns out that the charge is not quantized as integers, but in units of $e/2$. This has consequences also for a Josephson current through only one Mott insulating region. For this we found that the current will be 8π-periodic. Moreover, the bound states that were found follow non-Abelian braiding statistics.

In comparison to other proposed setups that host non-Abelian parafermions, such as fractional quantum Hall edge states with induced superconductivity, the setup introduced in this chapter does not require external magnetic fields. This can be positive for possible experimental realizations as magnetic fields and superconductivity prohibit each other to a great extent. For the same reason, we propose a new layout of a braiding scheme that allows braiding using only a small amount of gates. In general, for braiding gates are necessary to tune the outline of the topological insulator and to switch on and off the superconducting proximity effect. The system might therefore become useful for future realizations of quantum computation.

Chapter 4

Topological Anderson Insulator in the Kane-Mele Model

This chapter is based on the published manuscript:
C. P. Orth, T. Sekera, C. Bruder and T.L. Schmidt,
The topological Anderson insulator phase in the Kane-Mele model,
ArXiv e-prints: 1512.03233

4.1 Introduction

2D topological insulators [Hasan10, Qi11] comprise manifold interesting effects and new phenomena. Their most characteristic features, such as edge states protected by time-reversal symmetry, promise possible applications in quantum computation. However, the experimental realization of 2D topological insulators has so far been difficult and only a few materials, such as HgTeQW [König07], are known to show the effect. Of particular importance for topological insulators is a large spin-orbit coupling strength. Only if this is the case in a certain material, it may feature an inverted bandgap and a non-trivial topological invariant is found.

All the more surprising, it was discovered for the BHZ model that even if the clean system has parameters such that it is in a topologically trivial state, adding disorder can tune the system to a topologically non-trivial state [Li09]. This disorder induced topological phase was named TAI. TAIs exhibit the same robust conductance quantization of $2G_0 = 2e^2/h$ as ordinary 2D topological insulators [Prodan11]. This purely numerical discovery on a tight-binding version of the BHZ model was later confirmed independently [Jiang09]. An analytical description was derived by [Groth09] using an effective medium theory and the self-consistent Born approximation (SCBA).

In this analytical approach, the effect can be understood as a renormalization of both the topological mass m and the chemical potential μ_S in the sample with disorder strength W. For certain values of the model parameters, the renormalized topological mass $\bar{m}$ can change sign with increasing W. The nature of the disorder potential plays a crucial role as well. While random, uniformly distributed on-site energies (Anderson disorder) can renormalize a positive m to become negative, it was shown that this is not possible for certain kinds of bond disorder [Song12, Lv13], as it leads only to positive corrections to

m.

If the disorder strength is increased even further, the TAI phase vanishes again and the system becomes insulating. The reason could be due to tunneling events across the bulk [Chen12], which become possible by emergent percolating states in the bulk [Girschik15].

Moreover, similar phenomena were found also for 3D topological insulators [Guo10] or can be generated by periodically varying potentials [Fu14] or phonons [Garate13]. In the same line, different models that show topological effects, such as the Haldane model, were analyzed and a TAI phase was found [Xing11]. For another well known model for topological insulators on a honeycomb lattice, the Kane-Mele model [Kane05a, Kane05b], a TAI phase was not discovered so far. In this chapter we solve this open question by showing numerically that the Kane-Mele model supports the TAI phase. Even though both a finite Rashba spin-orbit strength λ_R and a staggered sublattice potential λ_ν can render the system topologically trivial, only for finite λ_ν a TAI phase can be observed. With an analytical derivation we shall shed light on the fact why this is the case. We furthermore find that the spin-orbit coupling strength λ_{SO} does not renormalize with an increasing disorder potential.

As the effect of TAI requires rather strong disorder strengths, an experimental realization of this topological phase is going to be challenging. Proposals exist to realize the effect using optical [Titum15] or acoustical systems [Yang15]. Furthermore, it was considered lately that disorder in the Kane-Mele model can arise due to random adatoms [Weeks11, Jiang12]. One of the main sources for disorder, for example in graphene, originates from the surface that the graphene flake is deposited on [Ando06, Ishigami07, Fratini08, Varlet15].

This chapter is structured as follows. In the first section, we discuss the underlying tight-binding model. This is succeeded by the presentation of numerical results of the TAI phase and finally, a theoretical understanding is given on the basis of the Born approximation.

4.2 Tight-binding formulation of the Kane-Mele model

For the following numerical evaluations and analytical derivations, this chapter is restricted to the Kane-Mele model as a convenient tool that shows a topologically non-trivial phase. It is used for example to describe graphene. Initially, graphene was treated as a possible topological insulator for low enough temperatures [Kane05a]. This was, however, a too optimistic prediction as it was later realized that the spin-orbit coupling strength in graphene is by some orders of magnitude smaller than what was assumed in these first works. Even though this led to a small dent in the popularity of the Kane-Mele model compared to the BHZ model, which describes topological insulators made of HgTeQWs, the Kane-Mele model is still an interesting framework to investigate topological phases in general. Furthermore, it is expedient to describe not only graphene, but also silicene [Aufray10, Kara12], germanene [Dávila14] and stanene [Zhu15], which are candidates for topological insulators as well. Compared to graphene, the latter materials all exhibit a buckled structure which is contained in the Kane-Mele model as a staggered sublattice potential. This is of special interest for this chapter, as this term turns out to be important for the observability of the TAI phase in the Kane-Mele model.

The Kane-Mele model describes a hexagonal honeycomb lattice of identical atoms, usually group-IV elements of the periodic table. In a tight-binding formulation it can be

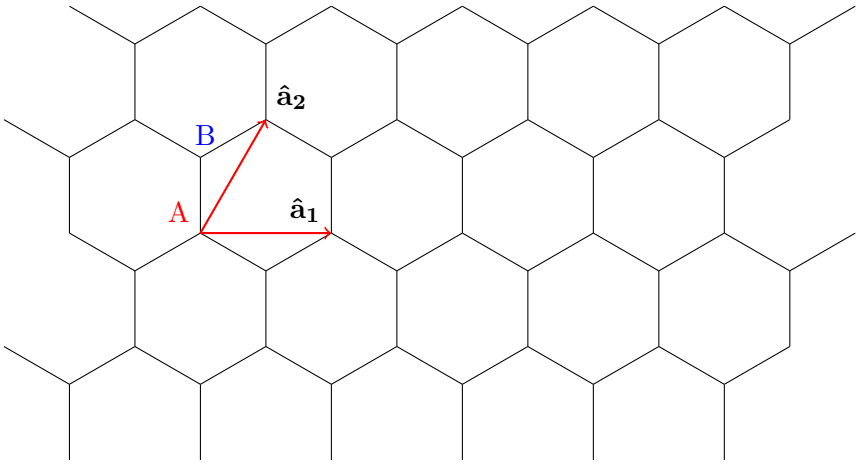

Figure 4.1: Honeycomb lattice of the Kane-Mele model. Primitive lattice vectors are $\hat{\mathbf{a}}_1$ and $\hat{\mathbf{a}}_2$. The basis atoms are A and B for the two sublattices. The lattice constant is a, the nearest neighbor distance $a/\sqrt{3}$.

written as

$$H = t\sum_{\langle ij\rangle} c_i^\dagger c_j + i\lambda_{SO}\sum_{\langle\langle ij\rangle\rangle} \nu_{ij} c_i^\dagger s^z c_j + i\lambda_R \sum_{\langle ij\rangle} c_i^\dagger \left(\mathbf{s}\times\hat{\mathbf{d}}_{ij}\right)_z c_j + \sum_i \left(\mu_S + \lambda_\nu \xi_i\right) c_i^\dagger c_i, \tag{4.1}$$

for vanishing chemical potential μ_S. We label the lattice as illustrated in Fig. 4.1. A and B are the two basis atoms of the primitive cell and $\hat{\mathbf{a}}_1$, $\hat{\mathbf{a}}_2$ the primitive lattice vectors. The operators $c_i^\dagger$ (c_i) create (annihilate) an electron at the i-th site. Nearest neighbor hopping is encoded by the tunneling amplitude t, which is used as the unit of energy in the following, if not mentioned explicitly otherwise. The sum $\sum_{\langle ij\rangle}$ denotes a sum over nearest neighbors and $\sum_{\langle\langle ij\rangle\rangle}$ over second nearest neighbors. The vector $\mathbf{s} = (s^x, s^y, s^z)$ contains the Pauli matrices and the vectors $\hat{\mathbf{d}}_i, \hat{\mathbf{d}}_j$ are unit vectors along the bonds that the electron traverses from site i to j. The coefficient $\nu_{ij} = (2/\sqrt{3})(\hat{\mathbf{d}}_i \times \hat{\mathbf{d}}_j)_z = \pm 1$ is either 1 for second nearest neighbor hopping that does a left turn or -1 for right turns. Additionally, Rashba spin-orbit coupling is included, with coupling strength λ_R and $\hat{\mathbf{d}}_{ij}$ is the unit vector parallel to the bond that connects site i and j. The aforementioned staggered sublattice potential strength is λ_ν with $\xi_i = 1$ for sublattice A atoms and $\xi_i = -1$ for sublattice B. A finite chemical potential μ_S can be applied as well. The lattice constant is given by a.

4.2.1 Band structure

The band structure of the Kane-Mele model is well known [Kane05b] and will not be discussed much further at this point. One of the main features of the model is a topologically non-trivial gap for suitable system parameters. While λ_ν will force the system to an ordinary insulating phase, λ_R rather pushes the system to a metallic phase. The spin-orbit coupling λ_{SO} however, leads to an inverted bandgap and a topological insulator. The three parameters are in competition. For $\lambda_R = 0$, $3\sqrt{3}\lambda_{SO} > \lambda_\nu$ or alternatively $\lambda_\nu = 0$ and $2\sqrt{3}\lambda_{SO} > \lambda_R$ the system is a topological insulator. What will be of interest later on is the intermediate region with finite λ_ν and small λ_R. In this case, the phase boundary between the trivial and topological insulators is a bit more subtle. Fig. 4.2 shows a

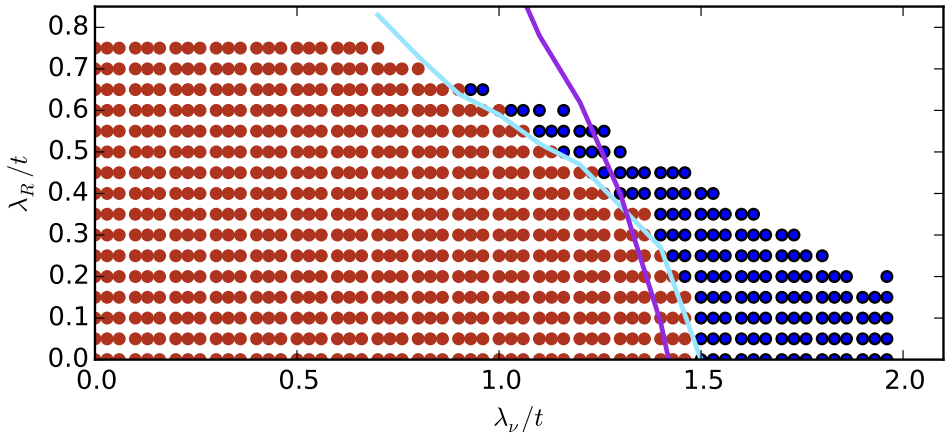

Figure 4.2: Configurations of the Kane-Mele band structure for different parameters λ_R and λ_ν. Above the light-blue, solid line (for $\lambda_{SO} = 0.3t$) the band structure is that of an ordinary insulator. The purple, solid line describes the same boundary for $\lambda_{SO} = 0.03t$. Below the light-blue, solid line the valence band and the conduction band touch at some point in k-space (for $\lambda_{SO} = 0.3t$) and the system is either a topological insulator or a metal or semimetal. The band structure was calculated for a strip with infinite length, zigzag edges and a width of $w = 30a$. The red dots mark parameters for which a topological insulator phase was found numerically. In the same way, the blue dots mark parameters for which a topological Anderson insulator was found.

diagram containing the different phases. The light-blue, solid line denotes the boundary above which a true insulator is expected for $\lambda_{SO} = 0.3t$. It was obtained by reading of the band structure, which means the data is afflicted by errors, which are not estimated. The criterion for the band structure to be in the class of a true insulator was that there is a bandgap around zero energy in which there are no states, independent of the momentum k. The purple, solid line shows the same data for $\lambda_{SO} = 0.03t$ but rescaled by a factor of 10. This is plotted to show that the data for different λ_{SO} is of the same scale, if both axes are rescaled by λ_{SO}.

Below the light-blue line the system is either a topological insulator or a metal. For small λ_ν and large λ_R (upper-left side in the figure) the band structure is that of a metal or semimetal. In this region, the conductance is not quantized anymore and larger than $2G_0$, even though still not at the same level as in the valence or conduction bands. Fig. 4.3 shows the essential part of the band structure for parameters in this region.

The band structure and all other numerical data was calculated using the Kwant software package [Groth14]. For the band structure, an infinite strip with width $w = 30a$ and zigzag edges was used. A larger width would not alter the diagram of Fig. 4.2 significantly. For each red dot, a topological insulator was also found from conductance calculations. In the same way, for each blue dot, a TAI was found. The method for this is explained in Section 4.3.

4.2.2 Typical energy scales

In this subsection, we shall list some numbers of the model parameters for the different materials. Graphene, silicene, germanene and stanene have lattice constants of $a_C =$

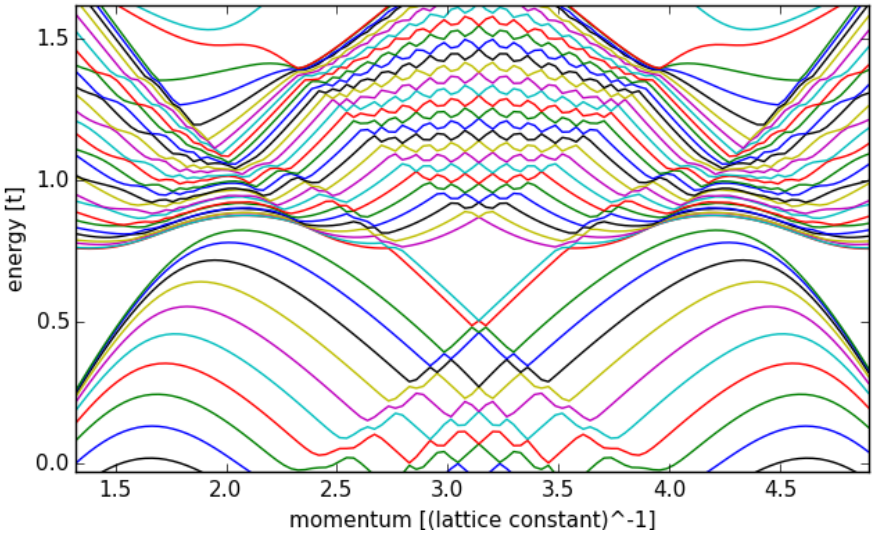

Figure 4.3: Band structure of a strip with zigzag edges, width $w = 30a$, $\lambda_{SO} = 0.3t$, $\lambda_R = 0.8t$, $\lambda_\nu = 0.03t$. The band structure is not that of a topological insulator anymore, but it can still be transformed continuously into that of a topological insulator. The conductance is larger than $2G_0$ for all relevant chemical potentials.

2.5Å[1], $a_{Si} = 3.8$Å, $a_{Ge} = 4.1$Å and $a_{Sn} = 4.7$Å. In contrast to graphene, the structures of silicene, germanene and stanene have a finite buckling, which originates from the relatively weak π-π bonding. They are not fully flat 2D planes, but the sublattices A and B are offset by a buckling distance of 0.5Å, 0.7Å and 1Å [Bishnoi13, Zhu15]. By applying an electric field perpendicular to the 2D plane, this finite buckling distance can be used to tune the potential of the A and B sublattices individually and thus change the coupling constant λ_ν in Eq. (4.1).

The bandgap in graphene was found to be of the order of only 10^{-3}meV[Yao07], originating from a spin-orbit coupling strength of the order of 10^{-3}meV [Min06]. While the spin-orbit coupling originates only from a second order expansion in the atomic carbon spin-orbit coupling strength ζ_0, Rashba spin-orbit interaction was found to be of first order in ζ_0 instead [Min06]. As an approximate value, $\lambda_R \approx 0.01$meV is given. This suggests that graphene will most likely not be in the topological phase.

Due to the buckled structure of silicene, it supports both an intrinsic Rashba spin-orbit coupling as well as a first order in ζ_0 spin-orbit coupling [Liu11b]. Values of $\lambda_R = 0.7$meV and $\lambda_{SO} = 4$meV are obtained, as well as a gap of 8meV. The same work also states values for germanene: $\lambda_R = 11$meV, $\lambda_{SO} = 46$meV and a gap of 93meV. Values for stanene are calculated as well and yield $\lambda_{SO} = 64$meV, $\lambda_R = 10$meV and a gap of 129meV. Numerical calculations found 2D stanene to be a topological insulator with a bandgap of about 0.1eV. Decorated stanene can even have bandgaps of 0.3eV [Xu13]. The Fermi velocity of the edge states was furthermore found to be about 4.4×10^5m/s.

[1]The nearest-neighbor distance for graphene is about 1.4Å.

4.2.3 Anderson disorder

As most other works on topological Anderson insulators, this chapter will be about Anderson disorder for most parts. Anderson disorder is one of the simplest possible disorder realizations. It is characterized by a uniformly distributed random potential for each site of the tight-binding model, expressed by the Hamiltonian

$$H_{Ad} = W \sum_i \epsilon_i c_i^\dagger c_i \tag{4.2}$$

with the disorder amplitude W and the uniformly distributed numbers $\epsilon_i \in [-1, 1]$. The random numbers for different sites are fully uncorrelated and follow the statistics (for large sample sizes)

$$\langle \epsilon_i \rangle = 0, \quad \langle \epsilon_i \epsilon_j \rangle = \frac{\delta_{ij}}{3}, \tag{4.3}$$

where δ_{ij} is the Kronecker delta and $\langle\rangle$ an average over all sites. The second moment of the distribution function is a characteristic quantity of the distribution and given by $\langle \epsilon_i^2 \rangle = 1/3$ for Anderson disorder. Anderson disorder was initially used to describe an effect about the absence of diffusive transport in certain doped semiconductors and led to a new view on metal-insulator transitions [Anderson58]. The main idea is that an electron that moves along a trajectory within a disordered material has a slightly higher probability to return to its origin, due to constructive interference. This leads to localization. While the same kind of disorder as in this original work is used here, the effect of a topological Anderson insulator is not connected to this idea in any obvious way.

The question about the physical origin of such a disorder term in the Kane-Mele model cannot be answered to full satisfaction so far. One possible realization could be a topological insulator, realized in an optical lattice [Béri11]. This setup would allow to induce a disorder potential with the help of an optical laser speckle potential [Billy08, Girschik13]. For graphene, one of the main sources for disorder are random strain fluctuations caused by the material that a graphene flake is usually deposited on [Couto14]. These fluctuations are of long range. Moreover, graphene was doped recently for example by boron [Kawai15]. This doping reached a level of 4.8 atom%, which corresponds to disorder with correlation lengths of roughly $5a$. For a better theoretical description of this kind of disorder, this chapter will cover spatially correlated random disorder potentials as well [Wagner15]. In this case, the variables ϵ_i will be modeled by

$$\epsilon_i = \sum_j a(\xi) e^{-\frac{r^2}{2\xi^2}} \varphi_j, \tag{4.4}$$

where ξ is the correlation length, $\varphi_j \in [-1, 1]$ are random variables uniformly distributed within the interval $[-1, 1]$ and the factor $a(\xi)$ is a correlation length dependent rescaling variable. The exponential accounts for a finite correlation between sites at position i and j if they are close to each other (r is the distance between site i and j). It can be shown that this definition of ϵ_i leads to a finite spatial gaussian correlation $\langle \epsilon_i \epsilon_j \rangle \propto \exp(-r^2/4\xi^2)$ up to an error ($\propto \exp(-r)$) which is only a small deviation from an ideal gaussian behavior. The rescaling coefficient $a(\xi)$ is necessary to keep the property $\langle \epsilon_i^2 \rangle = 1/3$ true. This can be done by a simple rescaling after calculation of the ϵ_i for $a(\xi) = 1$. In the limit of $\xi \to 0$ the disorder potential approaches the uncorrelated Anderson disorder again.

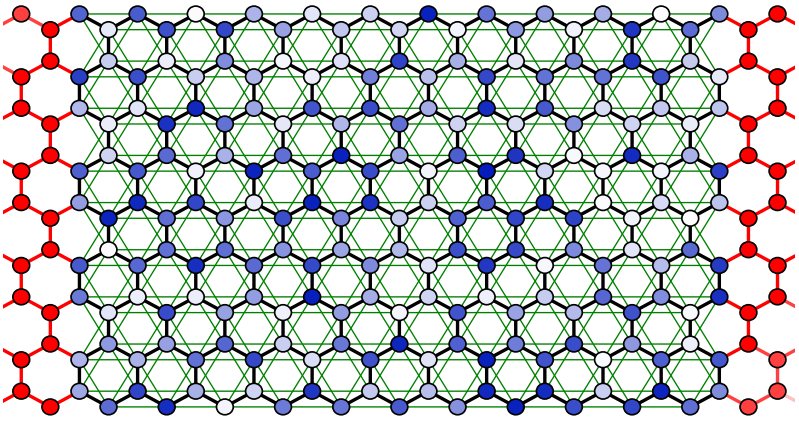

Figure 4.4: A typical setup for the numerical calculations. The sample has a size of length $l \approx 11a$ and width $w \approx 8a$. Second nearest neighbor hopping and nearest neighbor hopping are indicated. In red are the leads, which extend up to $\pm\infty$ and exhibit only ordinary nearest neighbor hopping. The shading of the sites shows the random potential of the atoms and ranges from $-W$ (white) to W (blue) on a linear scale.

4.3 Numerical realization

In this section we will present the numerical results that show that a TAI phase exists in the Kane-Mele model. It will start by giving some technical details about the numerical implementation using the Kwant code.

While the band structure can be calculated for an infinite strip of a certain width, disorder destroys the translational symmetry and can be simulated only for a finite sample region. Without translational symmetry, it is furthermore not possible to determine the band structure and a measure to determine if the system is in the topological regime or not is needed. Calculation of the conductance is the most widely applied method to do so. The way that is followed here is to attach two leads of width w and zigzag edges to a finite length, finite width (again w) sample with zigzag edges as well. The leads extend up to $\pm\infty$. Transport between the leads is then evaluated for varying Fermi energies E_F. It is convenient to model the leads as honeycomb lattices as well. For this chapter, the leads are assumed to be in the metallic regime, so we use the Kane-Mele model to describe the leads, but with parameters $\lambda_R = \lambda_{SO} = \lambda_\nu = 0$. Additionally, the chemical potential μ in the leads is pushed to be well inside the most conducting band by setting $\mu = 1.2t$ inside the leads. The chemical potential of the sample in-between is kept at $\mu_S = 0$, so the conduction through the disordered sample can be probed by tuning the Fermi energy roughly between the values $-\mu \lesssim E_F \lesssim \mu$. Conduction values of two times the conductance quantum $G = 2G_0$ indicate that the system is in a topological phase. Fermi energy values outside of the given regime can lead to misleading results as the leads might no longer be well-behaving conductors and alter the calculated conductance as well. In other words, there might not be enough overlap between the states in the leads and the energy levels of the sample.

Figure 4.4 shows an example setup for a rather small system with length $l \approx 11a$ and width $w \approx 8a$ for the purpose of illustration. The disorder potential is shown by a

blue shading of the sites. The small lattice size of this figure is chosen for a nice visual presentation of the lattice. In fact it turned out that a size of $l = 11a$, $w = 8a$ is too small for the system to be a TAI. The reason, as will be explained in the following sections, is that such a size is not enough to lead to a renormalization of the system parameters, which is the requirement to find a TAI.

In the following, we perform every evaluation of the conductance on a unique disorder realization. This is reasonable if quantities such as W are changed, because a different W necessarily corresponds to a new experimental realization which has its own disorder configuration. On the other hand, the Fermi energy can be tuned through a whole range of values within the same sample, featuring the same disorder realization. However, this could lead to undesirable effects. It might happen that by coincidence a disorder configuration has some special properties that render the sample non-characteristic. There is the unlikely case, for example, that the disorder forms something like a potential barrier in the middle of the strip, leading to a fully insulating setup. To exclude such a case, one usually does some averaging over many samples. The procedure in this chapter to use a new disorder realization for every value of the Fermi energy can be understood as a de-facto averaging procedure over several samples. This is why we preferred a higher resolution of the plots to an averaging procedure. With the higher resolution, the eye of the viewer can do a kind of averaging process by not looking at each individual point. This way, a region in parameter space with quantized conductance becomes even more impressive, as it is clear that the quantized conductance exists for the majority of disorder realizations, and is not an averaged quantity.

4.3.1 Dependence of the conductance on λ_R

The first quantity that we shall investigate is λ_R. Fig. 4.5 shows the conductance for a range of disorder strengths W, Fermi energy E_F and six different values of λ_R. The staggered sublattice potential is kept at a small value, $\lambda_\nu = 0.1t$. For all values of λ_R, the top and bottom parts for Fermi energies $|E_F| \gtrsim t$ show the conduction and valence bands with conductances $G > 2G_0$. With growing disorder strength W, the conductance vanishes as the bulk states localize. For disorder strengths of about $W \approx 2t$ there is some finite chance for the conductance of a certain disorder realization to be by accident $2G_0$, which is visible as a red dot. This happens both for topological insulators and for trivial insulators. Around $E_F \approx 0$, the system has a true conductance quantization of $2G_0$ for $\lambda_R < 0.84t$ only. That this region of solid red color exists means that the system is a topological insulator for the given parameters λ_R, λ_{SO}, λ_ν and W. We keep $\lambda_{SO} = 0.3t$ at a rather large value because in this case this effect is more pronounced. At $E_F = 1.2t$ an artifact of the leads can be seen. The reason is that the leads have a conductance minimum at the chemical potential $\mu = 1.2t$, which is visible also in the conductance of the whole setup as a small gap.

The effect of λ_R is twofold. On the one hand, it will push the system to a metallic/semimetallic phase. This can be seen, as the red region gets thinner and thinner with growing λ_R. With $\lambda_R = 0.84t \approx 2\sqrt{3}\lambda_{SO}$ the threshold to a semimetal is reached. The plot for $\lambda_R = 0.84t$ therefore shows a conductance minimum at $W = 0$ and $E_F \approx 0.6t$. The second effect of λ_R is that the red region starts to bend stronger with growing λ_R and the conductance shows furthermore a particle-hole asymmetry. The breaking of particle-hole symmetry is also visible from the Hamiltonian. In the tight-binding model, we define particle-hole symmetry as the replacement of creation by annihilation operators and vice

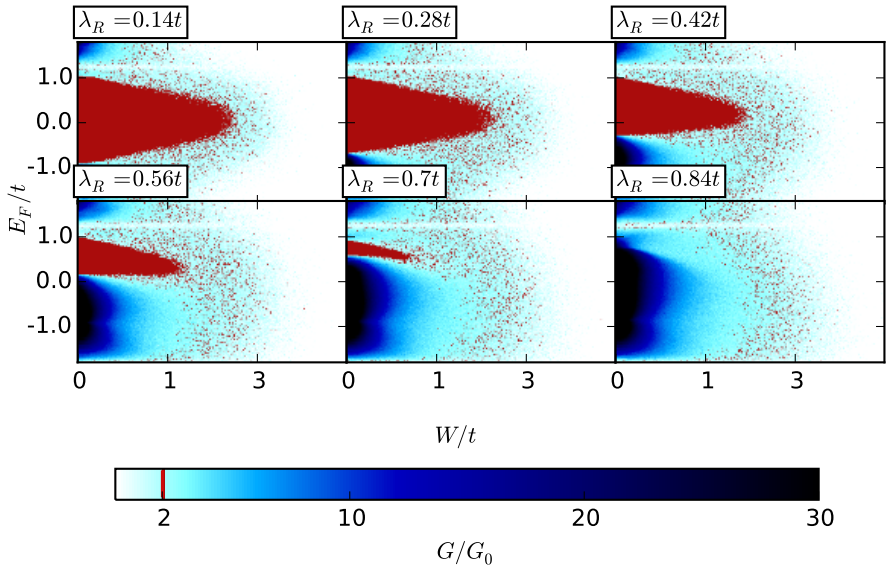

Figure 4.5: Heatmap of the conductance for varied disorder strength W and Fermi energy E_F. Quantized conductance of $G = 2G_0$ is highlighted in red. λ_R is tuned to six different values, showing a topological insulator to semimetal transition. The other parameters are $\lambda_\nu = 0.1t$, $\lambda_{SO} = 0.3t$, $\mu = 1.2t$ and $l = 150a$, $w = 93a$ for the system size.

versa. The particle-hole symmetry operator will then act as $\Upsilon c_i \Upsilon^{-1} = c_i^\dagger$. The effect of this symmetry operation on the Hamiltonian is that the energy spectrum should be reversed: $\Upsilon H \Upsilon^{-1} = -H$, if the system is particle-hole symmetric and the energy scale is shifted so that zero-energy is at half-filling. Certainly, this is not the only way to define a meaningful particle-hole symmetry operation. The transformed Hamiltonian reads

$$\begin{aligned}\Upsilon H \Upsilon^\dagger =& t \sum_{\langle ij \rangle} c_i c_j^\dagger + i\lambda_{SO} \sum_{\langle\langle ij \rangle\rangle} \nu_{ij} c_i s^z c_j^\dagger + i\lambda_R \sum_{\langle ij \rangle} c_i \left(\mathbf{s} \times \hat{\mathbf{d}}_{\mathbf{ij}} \right)_z c_j^\dagger + \sum_i \lambda_\nu \xi_i c_i c_i^\dagger \\ =& -t \sum_{\langle ij \rangle} c_i^\dagger c_j + i\lambda_{SO} \sum_{\langle\langle ij \rangle\rangle} \nu_{ij} c_i^\dagger s^z c_j + i\lambda_R \sum_{\langle ij \rangle} c_i^\dagger \left(\mathbf{s} \times \hat{\mathbf{d}}_{\mathbf{ij}} \right)_z c_j - \sum_i \lambda_\nu \xi_i c_i^\dagger c_i. \quad (4.5)\end{aligned}$$

The second line was obtained by using the fermionic anti-commutator and neglecting constant terms. One can see that the λ_{SO} and λ_R terms break the $\Upsilon H \Upsilon^{-1} = -H$ condition at the first glance.

However, it is possible to combine the particle-hole transformation with a mirror transformation about one of the symmetry axes of the hexagon lattice. If the axis is chosen in the right way, the transformation will map $\nu_{ij} \to -\nu_{ij}$ while keeping ξ_i constant. This is the case for example for the axis connecting A and B in Fig. 4.1. Mirroring about this axis will map atoms of sublattice A to the same sublattice A and B to atoms of the sublattice B. Moreover, second nearest neighbor hopping which was performing a right-turn will be mapped on hopping that is performing a left-turn, effectively changing the sign of ν_{ij}. This additional mirror symmetry can be used to restore the wrong sign of the spin-orbit term. Unfortunately, this is not compatible with the λ_R term, because $\hat{\mathbf{d}}_{ij} = (d_{ij}^x, d_{ij}^y)$ is mapped on either $\hat{\mathbf{d}}_{\mathbf{ij}}$ or $(-d_{ij}^x, d_{ij}^y)$, depending on its original orientation. For $\lambda_R = 0$ and

a sufficiently symmetric sample, particle-hole symmetry can be restored, though. This explains why Fig. 4.5 shows a particle-hole symmetry for small λ_R. This argument works because any chemical potential term was neglected. For a finite chemical potential, one can argue the same way, just that the particle hole operation needs to be combined with a finite shift in energy as well.

On the other hand, there is an inversion symmetry that allows to flip the sign of the λ_R term. This is for an inversion center at the center of a honeycomb hexagon. The inversion will lead to $\hat{\mathbf{d}}_{ij} \to -\hat{\mathbf{d}}_{ij}$. If $\lambda_\nu = 0$ and λ_{SO}, the particle-hole symmetry can therefore be restored if it is combined with this inversion symmetry. These symmetry considerations are valid for an infinite size 2D sample. Any finite boundary might break the symmetries as well.

4.3.2 The effect of λ_ν

In this subsection, we examine the effect of a finite λ_ν, but a vanishing or small λ_R. As derived in the last subsection, it can be expected that the system is particle-hole symmetric in this case. The transition between a topological insulator and a trivial insulator is expected to happen at $\lambda_\nu \approx 3\sqrt{3}\lambda_{SO}$. For $\lambda_{SO} = 0.3t$, Fig. 4.6 shows the conductance as a function of the Fermi energy, disorder strength W and several values of λ_ν. It can be seen that for a large range of values of λ_ν at the threshold between a topological insulator and a trivial insulator, the system shows a topological Anderson insulator phase. Interestingly, and in contrast to topological Anderson insulators found in the literature so far, the system is still perfectly particle-hole symmetric and the region with conductance quantization $2G_0$ broadens to both larger and smaller energies for larger W. A theoretical explanation of this will be given in Section 4.4.

At this point, we should write down a formal definition of a TAI. While in the clean limit, the system is a trivial gap insulator, disorder induces a gap closing and reopening of a topologically non-trivial gap. This behavior has to be the case for the majority of all possible disorder configurations, if the random distribution leading to the disorder has the same statistics. That this is the case is illustrated in Fig. 4.7

Figure 4.6 shows that a topological Anderson insulator is found between $0.96\times3\sqrt{3}\lambda_{SO} \lessapprox \lambda_\nu \lessapprox 1.18 \times 3\sqrt{3}\lambda_{SO}$. This means that through disorder the regime in which a $2G_0$ quantized conductance is found can be extended by 20% beyond the usual parameter regime. This result was obtained for a value of $\lambda_{SO} = 0.3t$. For smaller λ_{SO} the effect still exists, but in a less pronounced form. Figure 4.8 shows a TAI found for $\lambda_{SO} = 0.03t$. The effect is much weaker but still visible.

Spatially correlated disorder does influence the TAI phase as well [Girschik13]. For a disorder potential as in Eq. (4.4) one finds that the TAI effect vanishes with larger correlation length ξ. A critical threshold is reached at $\xi = 0.5a$ [Wagner15]. For larger values, the TAI phase is not seen. The critical correlation length is of about the order of the nearest neighbor distance. Fig. 4.8 illustrates the effect of spatially correlated disorder for a correlation length of $\xi = 0.3a$ and a finite λ_R (more on this in the next subsection).

The strong effect of the correlation length on the TAI phase sheds some light on the origin of the phenomenon. A trivial gap is generated by λ_ν because it acts as a natural potential barrier that blocks transport between two neighboring sites. If a random potential is added to these sites, it may happen that the potentials of two neighboring sites by accident become equal and transport is favored. This is however only possible if the correlation length is sufficiently small. For random disorder with a large ξ, two

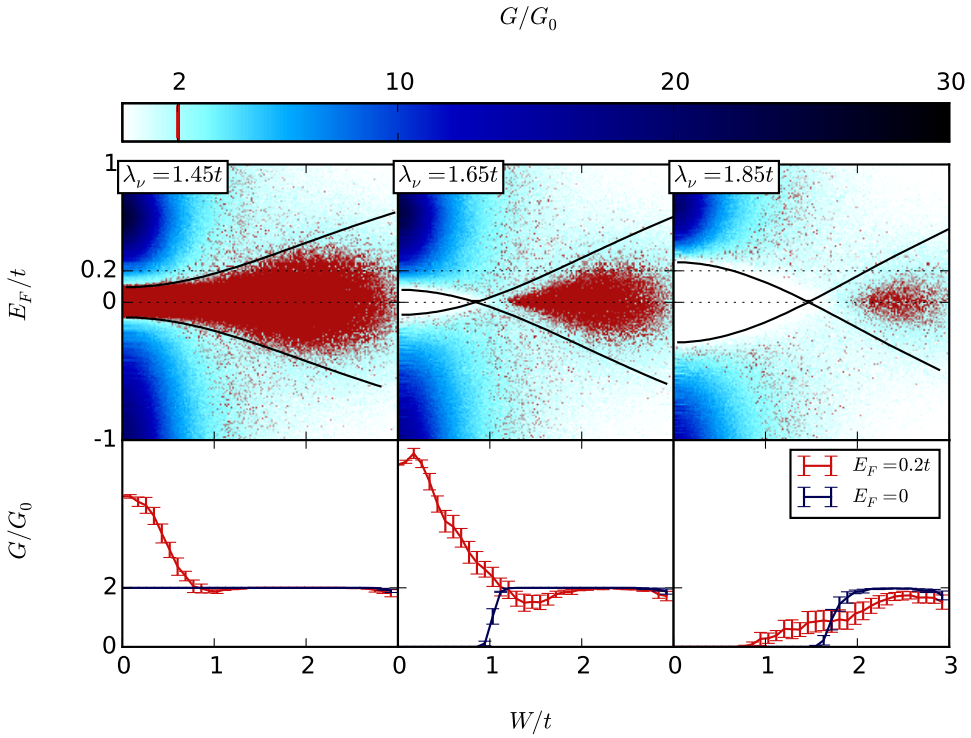

Figure 4.6: *Top row:* Heatmap of the conductance for varied disorder strength W and Fermi energy E_F. Quantized conductance of $G = 2G_0$ is highlighted in red. λ_ν is tuned through three different values, showing a topological insulator to trivial insulator transition. The other parameters are $\lambda_R = 0t$, $\lambda_{SO} = 0.3t$ and $l = 150a$, $w = 93a$ for the system size. The chemical potential of the leads is $\mu = 1.2t$. The black lines are calculated using an analytical approach, described in detail in Section 4.4. *Bottom row:* The plots show the conductance for two fixed energies $E_F = 0$ (blue), $E_F = 0.2t$ (red). This data was obtained as an average over 100 different disorder configurations. The errors are statistical errors of this averaging and vanish in the regions with conductance quantization at $2G_0$. The parameters are the same as in the top row.

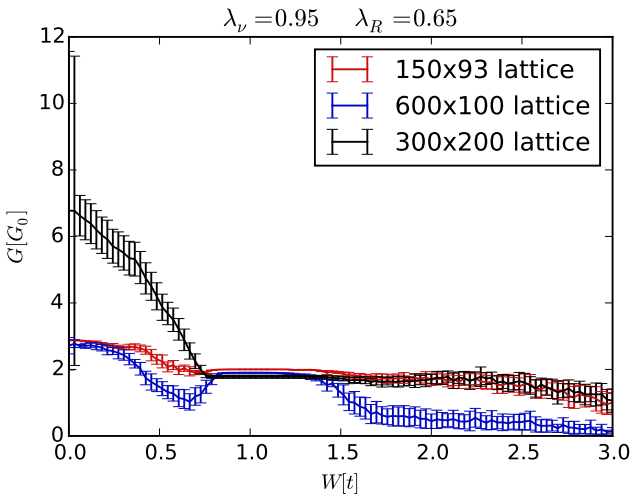

Figure 4.7: The conductance in units of G_0 as a function of disorder strength W. The red, blue and black data is for three different sample sizes, of $150a \times 93a$, $600a \times 100a$ and $300a \times 200a$ (length $\times$ width). Each conductance was calculated for 100 different disorder configurations and averaged, which leads to the error bars. The parameters are $\lambda_R = 0.65t$, $\lambda_\nu = 0.95t$, $\lambda_{SO} = 0.3t$, $E_F = 0.55t$ and $\mu = 1.2t$.

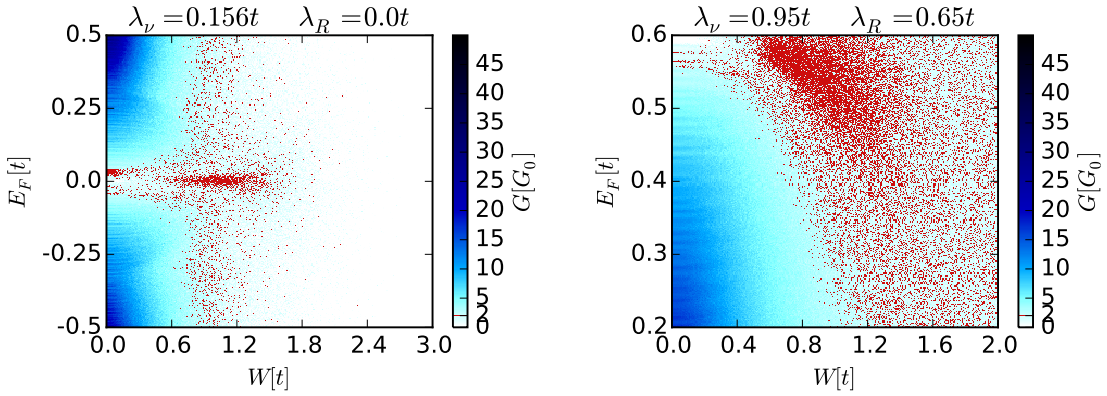

Figure 4.8: *Left:* A TAI phase found for small $\lambda_{SO} = 0.03t$ and Anderson disorder at the edge to a trivial insulating phase. *Right:* TAI in the case of spatial correlated disorder with correlation length $\xi = 0.4a$ and $\lambda_{SO} = 0.3t$. For reasons of implementation, the sample setup for this calculation is of trapezoidal and not rectangular shape. Both figures are for a sample size of $l = 150a$, $w = 93a$ and $\mu = 1.2t$.

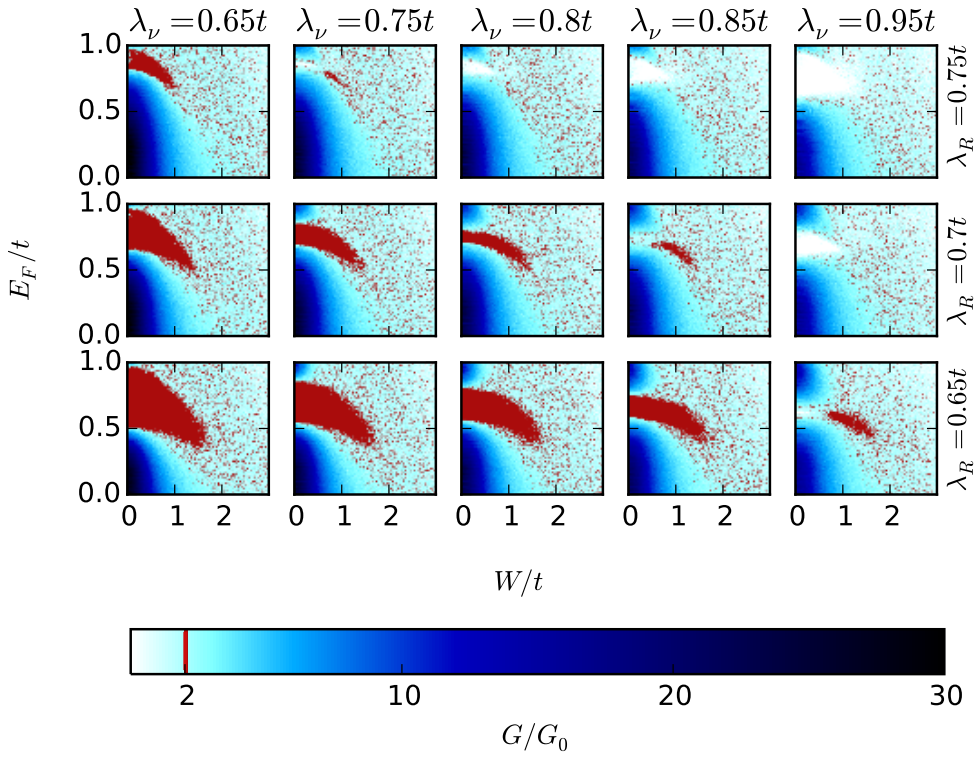

Figure 4.9: Conductance plots ($2G_0$ in red) showing the TAI phase for $\{\lambda_\nu, \lambda_R\} = \{\{0.75t, 0.65t\}, \{0.8t, 0.7t\}, \{0.85t, 0.7t\}, \{0.95t, 0.65t\}\}$. The remaining parameters are $\lambda_{SO} = 0.3t$, $w = 93a$, $l = 150a$, $\mu = 1.2t$.

neighboring sites share almost the same random potential and are forced to have quite different total potentials due to λ_ν. It therefore seems plausible that the gap opened by λ_ν is reduced due to the disorder and a topological insulator phase appears again.

4.3.3 Finite λ_R and λ_ν

The last two subsections showed that a topological Anderson insulator is found if a trivial gap is opened by λ_ν, while it is not present if the topological gap is closed by λ_R. This subsection illuminates the intermediate regime of finite λ_ν and λ_R. In a first try, we assume that the boundary between the topological phase and the trivial phase is given by an elliptic equation

$$\left(\frac{\lambda_R}{2\sqrt{3}}\right)^2 + \left(\frac{\lambda_\nu}{3\sqrt{3}}\right)^2 \approx \lambda_{SO}^2. \tag{4.6}$$

This way, we find the first set of parameters which shows a TAI phase as $\lambda_R = 0.7t$, $\lambda_\nu = 0.8t$, $\lambda_{SO} = 0.3t$. A parameter scan close to these values reveals a couple of other possible parameter combinations, with TAI phases as shown in Fig. 4.9. This plot allows the following conclusions. The TAI phase exhibits a strong particle-hole asymmetry. This

can be explained by the presence of λ_R, as shown already. The $2G_0$ quantized region is not only bending with growing W, also the topological insulator phase and the trivial gap are shifted to larger values of E_F, as can be seen at the $W = 0$ limit. Furthermore, the TAI phase seems to shrink for smaller λ_ν and larger λ_R. This is in accordance with the fact that the limit $\lambda_\nu = 0$ does not show any TAI while in the limit $\lambda_R = 0$ a rather pronounced TAI phase is found.

To get a clear picture of the region for finite λ_R and λ_ν, we go back to Fig. 4.2. Every evaluated parameter set is marked by a red or blue dot. The red dots mark parameters for which a topological insulator was found. This is the case for parameters close to or below the light-blue line, marking the existence of two Dirac cones in the gap of the band structure without disorder. The blue dots show that a TAI was found between the topological insulator and the trivial insulator phases. White space means that a trivial insulator or a metal was found. The TAI is mostly found for values of large λ_ν and small λ_R and is not found at all for small λ_ν. It is no longer found in the region where the direct bandgap vanishes, where the solid light-blue line starts to escape to large λ_R values. This shows moreover that the initial assumption of an ellipsoid boundary, Eq. (4.6), was not a useful condition to find a TAI phase. Instead, the TAI phase exists only at the boundary between topological insulators and trivial insulators, but not at the boundary towards metallic behavior for small λ_ν.

4.4 Born approximation for the Kane-Mele model

In this section, we shall explain several features of the numerical data shown in the last section on the basis of an analytical model. The broken particle-hole symmetry was already explained in Subsection 4.3.1 by the presence of Rashba spin-orbit coupling.

The main idea of an analytical model for the TAI phase found in the BHZ model [Li09, Jiang09] was given by [Groth09]. In this theory, the finite disorder strength leads to a renormalization of the topological mass parameter m. It is shown that a positive m, describing a trivial insulator, is renormalized and can become negative. The disorder is taken into account by the self-consistent Born approximation. This approximation is valid for small impurity densities n_{imp} compared to the electron density n_e and small scattering potentials compared to a characteristic level spacing. With impurity densities of about $1/a^2$ and a scattering potential of $W \gg \Delta$, where Δ is the bandgap, these conditions are not fulfilled for Anderson disorder. Nevertheless, the theory can correctly reproduce some of the features found numerically. We try at this point to give some ideas about how this can be possible. Assuming that a TAI phase exists, which will lead to protected edge states at the sample circumference, backscattering is strongly reduced for these edge states. The effective density of impurities that can lead to backscattering for these edge states is much reduced as well. Therefore, the mechanism that leads to the protected edge states of a topological insulator might also explain why the application of the self-consistent Born approximation to describe topological Anderson insulators can be successful. However, the approximation would be valid only within the regime of the $2G_0$ quantized conductance. Additionally, a strong scattering potential W does not mean that the self-consistent Born approximation does not work. This requirement mainly originates from the mathematical necessity that the summed diagrammatic expressions for the self-energy converge. This can still be the case for large W as well.

4.4.1 Diagonalization of the Kane-Mele model

The tight-binding model of Eq. (4.1) was written in momentum representation in [Kane05b]. It reads

$$\mathcal{H}(\boldsymbol{k}) = \sum_{a=1}^{5} d_a(\boldsymbol{k})\Gamma^a + \sum_{a<b=1}^{5} d_{ab}(\boldsymbol{k})\Gamma^{ab}, \tag{4.7}$$

were the Dirac matrices are defined as $\Gamma^{(1,2,3,4,5)} = (\sigma^x \otimes \mathbb{1}, \sigma^z \otimes \mathbb{1}, \sigma^y \otimes s^x, \sigma^y \otimes s^y, \sigma^y \otimes s^z)$ and $\Gamma^{ab} = [\Gamma^a, \Gamma^b]/(2i)$. The Pauli matrices σ^k represent the sublattice indices and s^k spin indices. The $\boldsymbol{k}$ dependent factors are given by

$$\begin{aligned}
d_1(\boldsymbol{k}) &= t(1 + 2\cos x \cos y) & d_{12}(\boldsymbol{k}) &= -2t \cos x \sin y \\
d_2(\boldsymbol{k}) &= \lambda_\nu & d_{15}(\boldsymbol{k}) &= \lambda_{SO}(2\sin 2x - 4 \sin x \cos y) \\
d_3(\boldsymbol{k}) &= \lambda_R(1 - \cos x \cos y) & d_{23}(\boldsymbol{k}) &= -\lambda_R \cos x \sin y \\
d_4(\boldsymbol{k}) &= -\sqrt{3}\lambda_R \sin x \sin y & d_{24}(\boldsymbol{k}) &= \sqrt{3}\lambda_R \sin x \cos y.
\end{aligned} \tag{4.8}$$

with $x = k_x a/2$ and $y = \sqrt{3}k_y a/2$.

The work of [Groth09] for the BHZ model relied on an effective low-energy model to describe the TAI effect. In this chapter, we choose a different approach instead. Indeed, the low-energy expansion leads to several open questions such as: which K-valley to choose for the expansion, what happens with the other K valley and why is the expansion justified. Instead, working with the exact Hamiltonian does not increase the complexity of the problem too much.

4.4.2 Lowest order Born approximation

In the self-consistent Born approximation, the self-energy is given by an integral equation [Bruus04]

$$\Sigma = \frac{1}{3}W^2 \left(\frac{a}{2\pi}\right)^2 \int_{BZ} d\boldsymbol{k} \frac{1}{E_F - \mathcal{H}(\boldsymbol{k}) - \Sigma}, \tag{4.9}$$

where the prefactor $W^2/3 = W^2\langle\epsilon_i^2\rangle$ results from the second moment of the disorder potential for $\epsilon_i \in [-1, 1]$. The self-energy Σ is assumed to be energy and momentum independent. The integration is over the first Brillouin zone, which has hexagonal shape and has a circumference with size $6 \times 4\pi/3a$. The first K-valley is at $(k_x, k_y) = (4\pi/3a, 0)$ and at the right corner of the first Brillouin zone. This way, the integral can be calculated as

$$\int_{BZ} d\boldsymbol{k} = 4\int_0^{2\pi/3a} dk_x \int_0^{2\pi/\sqrt{3}a} dk_y + 4\int_{2\pi/3a}^{4\pi/3a} dk_x \int_0^{-\sqrt{3}k_x + 4\pi/\sqrt{3}a} dk_y. \tag{4.10}$$

At this point, some general features of the self-energy can be derived. Even though Σ is a 4×4 matrix with up to 16 unknowns, it might be expressed by a smaller set of variables due to the special structure of the Hamiltonian $\mathcal{H}$. A promising ansatz for Σ is the following

$$\Sigma = \sum_{a=1}^{5} g_a \Gamma^a + \sum_{a<b=1}^{5} g_{ab}\Gamma^{ab}. \tag{4.11}$$

We use this ansatz where only those coefficients g are finite that were also non-vanishing in Eq. (4.7) and perform the matrix inversion of Eq. (4.9). This shows that a new matrix structure is generated and that at least g_{34} has to be finite. These additional terms have to be understood as new couplings that are generated in the Hamiltonian due to the disorder. The full solution of Eq. (4.9) is a tedious task, if possible at all. However, as it turns out, solving this equation is not necessary for a good quantitative description of the TAI, as we will show.

Instead, for the current purposes, it is sufficient to work with the lowest order in W approximation. This corresponds to setting $\Sigma = 0$ on the right hand side of Eq. (4.9). One complication arises still. After the matrix inversion and the integration, the components of the resulting matrix have to be sorted to extract the renormalized quantities. We accomplish this by adding the matrix elements in the right way. This leads to the equations

$$\begin{aligned}
\Sigma_{E_F} &= \frac{\Sigma_{11} + \Sigma_{22} + \Sigma_{33} + \Sigma_{44}}{4} \\
\Sigma_{\lambda_\nu} &= \frac{\Sigma_{11} + \Sigma_{22} - \Sigma_{33} - \Sigma_{44}}{4} = g_2 \\
\Sigma_{\lambda_{SO}} &= \frac{\Sigma_{11} - \Sigma_{22} - \Sigma_{33} + \Sigma_{44}}{4} = g_{15} = 0.
\end{aligned} \tag{4.12}$$

The Σ_{ij} are the ij components of the matrix Σ. While the determination of the λ_ν and E_F related self energies Σ_{λ_ν} and Σ_{E_F} is more or less straightforward, it is not that trivial for λ_R. The reason is that λ_R appears in the Hamiltonian as the prefactor of a $\sigma^y \otimes s^x$, $\sigma^y \otimes s^y$, $-\sigma^x \otimes s^x$ and $-\sigma^x \otimes s^y$ term. The self-energy in the lowest order however has only a $\sigma^y \otimes s^x$ term. We find

$$\begin{aligned}
\Sigma_{41} + \Sigma_{32} + \Sigma_{23} + \Sigma_{14} &= 4g_{23} = 0 \\
-\Sigma_{41} + \Sigma_{32} + \Sigma_{23} - \Sigma_{14} &= 4g_4 = 0 \\
-\Sigma_{41} + \Sigma_{32} - \Sigma_{23} + \Sigma_{14} &= 4g_{24} = 0 \\
\left[\Sigma\Gamma^3\right]_{11} = \left[\Sigma\Gamma^3\right]_{22} = \left[\Sigma\Gamma^3\right]_{33} = \left[\Sigma\Gamma^3\right]_{44} &= g_3 = \Sigma_{\lambda_{R3}},
\end{aligned} \tag{4.13}$$

where it was used that $[\Gamma^3]^{-1} = \Gamma^3$. The effect of the disorder on λ_R can thus not be described only by a renormalization of λ_R by a self-energy. Instead, just the part of the Rashba spin-orbit coupling that is proportional to $\sigma^y \otimes s^x$ renormalizes. To take this into account, one has to introduce a new coupling, labeled λ_{R3}, that exists only for finite disorder strength. The equations for the renormalized quantities $\bar{\lambda}_\nu$, $\bar{E}_F$, $\bar{\lambda}_{SO}$, $\bar{\lambda}_R$ and $\bar{\lambda}_{R3}$ finally read

$$\begin{aligned}
\bar{\lambda}_\nu &= \lambda_\nu + \Sigma_{\lambda_\nu} \\
\bar{E}_F &= E_F - \Sigma_{E_F} \\
\bar{\lambda}_{SO} &= \lambda_{SO} \\
\bar{\lambda}_R &= \lambda_R \\
\bar{\lambda}_{R3} &= \Sigma_{\lambda_{R3}},
\end{aligned} \tag{4.14}$$

were the negative sign in front of Σ_{E_F} originates from the denominator in Eq. (4.9) in which E_F and Σ enter with opposite signs. Unfortunately, the explicit expressions of $\Sigma_{E_F}, \Sigma_{\lambda_\nu}, \Sigma_{\lambda_{R3}}$ are to lengthy to be written down at this point. To understand the renormalization of λ_R, it is instructive to translate the model for the renormalized quantities

back to a tight-binding formulation. By doing this, the λ_{R3} term will become a nearest-neighbor hopping amplitude that exists only for one out of the three possible kind of hoppings, the hopping perpendicular to $\hat{\mathbf{a}}_\mathbf{1}$. Both the Rashba spin-orbit coupling and the λ_{R3} contribution are still rotation symmetric with respect to rotations about an angle of 120°. This rotation symmetry is microscopically broken by the disorder, but globally it exists still for the averaged quantities that are used to construct the effective medium theory. This can be seen by rotating both the real space lattice and the vector of Pauli matrices around the same angle (which has to be a multiple of 120°).

4.4.3 Comparison of the Born approximation and the tight-binding results

Equations (4.12), (4.13) and (4.14) as well as Eq. (4.9) can be used to calculate boundaries between which a quantized $2G_0$ conductance for a TAI can be expected. For $\lambda_R = 0$, it follows that $\bar{\lambda}_{R3} = 0$ and the condition for a system to be a topological insulator is given by $3\sqrt{3}\lambda_{SO} > \lambda_\nu$. The equation $3\sqrt{3}\lambda_{SO} = \lambda_\nu$ can be extrapolated to the case of finite disorder, $3\sqrt{3}\bar{\lambda}_{SO} = \bar{\lambda}_\nu$. The self-energy Σ_{λ_ν} is usually negative, therefore the system can become a topological insulator, even if the original $\lambda_\nu > 3\sqrt{3}\lambda_{SO}$. For larger initial λ_ν this happens at a larger disorder strength W. This is why the crossing of the two black lines in Fig. 4.6 move further to the right with growing λ_ν. For $\lambda_\nu = 1.95t$ the transition happens only at a disorder strength where the conductance is already suppressed, possibly due to emergent percolating states in the bulk. The system is not a TAI anymore. It is important to stress that the black lines are a result of the Born approximation while the underlying red and blue heatmap was obtained by numerically solving the tight-binding model for a given disorder realization. For this calculation, no adjustable parameter or fitting variable is used.

For the full two-dimensional Kane-Mele model with $\lambda_R = 0$ the size of the gap is given by $|2\lambda_\nu - 6\sqrt{3}\lambda_{SO}|$. As particle-hole symmetry is still given, the upper and lower edges of the gap are described by $\pm|\lambda_\nu - 3\sqrt{3}\lambda_{SO}|$. This can be extended again to the finite W case, $\pm|\bar{\lambda}_\nu - 3\sqrt{3}\bar{\lambda}_{SO}|$, which is exactly what is plotted as the black lines (in fact joined dots that represent each an individual evaluation of the integral in Eq. 4.9) in Fig. 4.6. The gap first closes and reopens as a negative gap for $\lambda_\nu = 1.65t, 1.85t$. The agreements of the lowest order Born approximation with the tight-binding solution is evident. Deviations exist only for large $W > 2t$.

For finite λ_R the situation is more difficult. To the best knowledge of the author, an analytical expression for the gap in a model with finite λ_R and λ_ν and especially λ_{R3} does not exist. An analytical expression can be derived if the Dirac cones are located at the K-points. It can be proven that this is the case if time-reversal, C_3 and an inversion symmetry are present [Bernevig13]. In this case, we evaluate the Hamiltonian at the K-points and diagonalize it. The four eigenvalues allow to determine an analytical solution for the gap of the 2D model. As it is not clear that this works in our case this can only be used as an approximative method here. To nevertheless obtain a meaningful condition in the finite λ_R case, we calculate the band structure of a strip of the clean system with finite λ_R, λ_ν and an artificial λ_{R3} and read off the gap and the positions of the bands manually. The values are then used to calculate two interpolating functions, $h_u(\lambda_\nu, \lambda_R, \lambda_{R3})$ and $h_l(\lambda_\nu, \lambda_R, \lambda_{R3})$, which describe the closing and re-opening of the gap. These functions are finally applied to the renormalized values $\bar{\lambda}_\nu$ and $\bar{\lambda}_{R3}$. h_u describes the lower edge of the upper band and h_l the upper edge of the lower band. The two functions are shown for

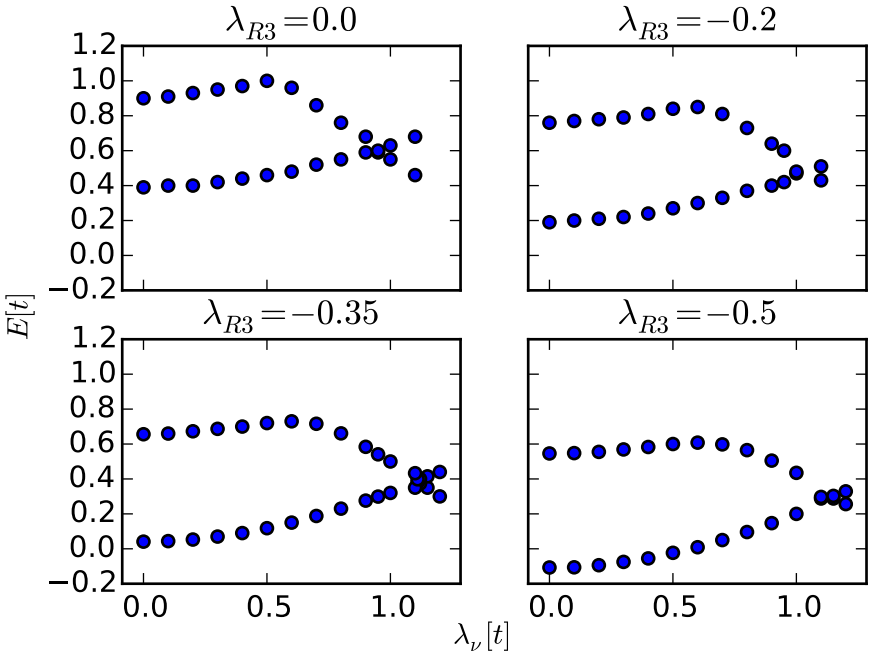

Figure 4.10: The upper edge of the lower band and the lower edge of the upper band as a function of λ_ν for the Kane-Mele model. The extra term λ_{R3} is added to the model and the band structure is evaluated for four different values of λ_{R3}. The band structure was calculated for a strip with width $w = 93a$ and $\lambda_{SO} = 0.3t$. The gap-closing is seen at approximately $\lambda_\nu = t$. Rashba spin-orbit coupling is kept at $\lambda_R = 0.65t$.

$\lambda_R = 0.65t$ and four values of λ_{R3} in Fig. 4.10. With growing W, λ_{R3} gets renormalized to negative values; between $\lambda_{R3} = 0$ and $\lambda_{R3} = -0.5t$ for values of $0 \leq W \leq 3t$.

Interestingly, an increasingly negative λ_{R3} not only shifts the gap to smaller energies, it furthermore leads to a closing of the gap for larger λ_ν only. This means that solely the existence of a finite λ_{R3} can lead to a topological transition to a non-trivial phase. This can be seen in Fig. 4.10. The topologically non-trivial gap is on the left-hand side of the gap-closing. This region further expands to larger λ_ν with the decrease of λ_{R3} from 0 to $-0.5t$.

The two conditions $h_u(\bar{\lambda}_\nu, \lambda_R, \bar{\lambda}_{R3}) = \bar{E}_F$ and $h_l(\bar{\lambda}_\nu, \lambda_R, \bar{\lambda}_{R3}) = \bar{E}_F$ can be used to describe the boundaries of the region with $2G_0$ conductance for finite λ_R. The solutions of these equations are plotted in Fig. 4.11 as the two black lines. Some significant deviations from the numerical data and the lowest order expansion of the Born approximation are visible. First of all, the solution of the Born approximation is much more demanding, as the Hamiltonian is a true 4×4 matrix that does not decompose into two 2×2 blocks as for $\lambda_R = 0$. This makes the numerical evaluation of the corresponding integrals more complex.

While the lower edge of the $2G_0$ conductance region is described quite well, the upper edge and especially the left part are not correctly reflected. This seems to be connected to a general deficit of the SCBA, as the left part is for small W only and thus likely to be described by the lowest order SCBA expansion. Furthermore, evaluation of the band structure reveals that for $\lambda_\nu = 0.95t$ and $\lambda_R = 0.65t$ the system is exactly at the transition between a trivial insulator and a topological insulator. The gap is just closed. While this can be seen in the lowest order Born approximation solution, the $2G_0$ conducting region

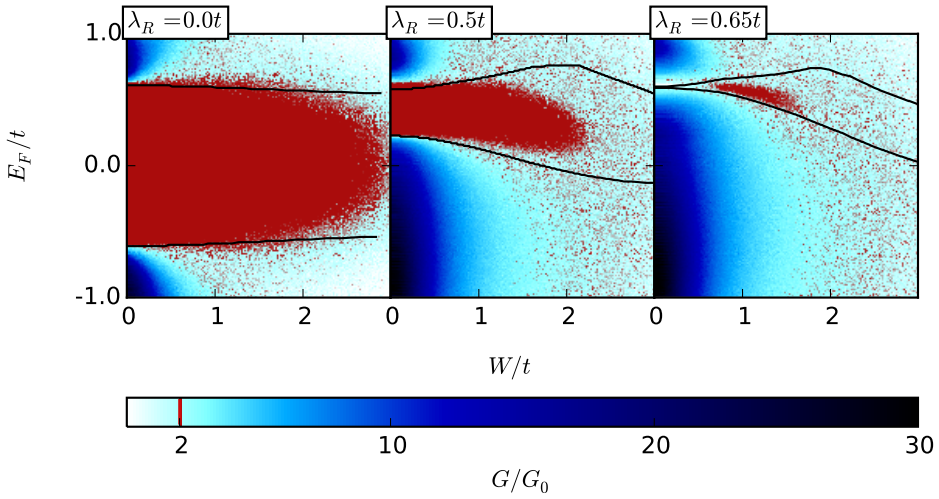

Figure 4.11: Comparison of the Born approximation to numerical data. The two dotted lines are solutions to the equations $h_u(\bar{\lambda}_\nu, \lambda_R, \bar{\lambda}_{R3}) = \bar{E}_F$ and $h_l(\bar{\lambda}_\nu, \lambda_R, \bar{\lambda}_{R3}) = \bar{E}_F$. The parameters for the plot are $\lambda_{SO} = 0.3t$, $\lambda_\nu = 0.95t$, $w = 93a$, $l = 150a$ and a chemical potential of $\mu = 1.2t$ in the leads.

starts only at larger disorder strength $W \approx 0.6t$. This is about the same energy scale at which the conduction and valence bands start to disappear as well. With this in mind, going back to Fig. 4.6 reveals that the same can be seen in the $\lambda_R = 0$ case as well: in the $\lambda_\nu = 1.55t$ data, the $2G_0$ conductance region starts only for $W \approx 0.6t$.

To understand this qualitatively, Fig. 4.12 shows the same data as in Fig. 4.11 with the only difference that we set all site potentials that are within the interval $(-0.6t, 0.6t)$ to zero. Therefore, for $W < 0.6t$ there is no disorder at all. This procedure increases the average impurity strength and at the same time reduces the impurity density. It has an effect on the TAI, which now exists only for larger W. The dashed, green line in the figure illustrates the beginning of the $2G_0$ conducting area as it was in the setup with an Anderson kind of disorder, see Fig. 4.11. That the left edge of that area moved indicates that the impurity density plays an important role. That it did not move up to $W \approx 2\times 0.6t$ shows that also the absolute impurity strength is a decisive quantity. A closer look leads to a critical value of $W \approx 0.67t$ for Fig. 4.11 and $W \approx 0.82t$ for Fig. 4.12. Calculating $\langle \epsilon^2 \rangle$ for these two cases leads to

$$\begin{aligned} \langle \epsilon^2 \rangle &= \frac{1}{2W} \int_{-W}^{W} d\epsilon \epsilon^2 = W^2/3 = 0.15 && \text{for } W = 0.67 \\ \langle \epsilon^2 \rangle &= \frac{1}{2W} \left[\int_{-W}^{-0.6} d\epsilon \epsilon^2 + \int_{0.6}^{W} d\epsilon \epsilon^2 \right] = 0.14 && \text{for } W = 0.82, \end{aligned} \tag{4.15}$$

which indicates that the second moment of the disorder potential $\langle \epsilon^2 \rangle$ has to be above a critical threshold of 0.14 to find a TAI. To investigate this hypothesis in more detail has to be the subject of future work. In the same way, the understanding why the lowest order Born approximation is not sufficient to describe the upper boundary of the TAI region in Fig. 4.11 has to be done at a later point.

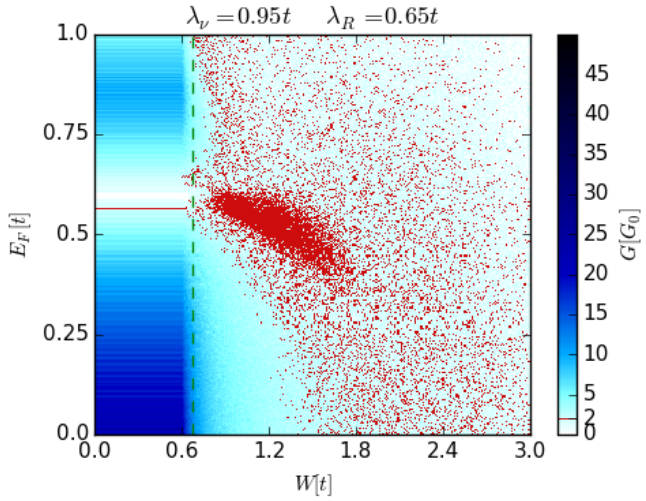

Figure 4.12: The conductance heatmap for a modified Anderson disorder. For this plot, Anderson disorder was used but all disorder potentials within the interval $(-0.6t, 0.6t)$ were set to zero. The remaining parameters are as in Fig. 4.11, the dashed, green line marks the beginning of the $2G_0$ conducting area as in Fig. 4.11.

Low energy expansion of the Kane-Mele model

We can obtain a simple, completely analytical explanation of the TAI effect for $\lambda_R = 0$. For this, we perform a low energy expansion of the terms in Eq. (4.8) up to second order in q_x, q_y. Here, the expansion is about $\boldsymbol{k} = \boldsymbol{K}^+ + \boldsymbol{q}$ with $\boldsymbol{K}^+ = \frac{2\pi}{a}(\frac{2}{3}, 0)$. Only the highest order terms are kept, as follows

$$\begin{aligned} d_1 &= -t\frac{\sqrt{3}a}{2}q_x, \qquad & d_2 &= \lambda_\nu, \\ d_{12} &= t\frac{\sqrt{3}a}{2}q_y, \qquad & d_{15} &= -3\sqrt{3}\lambda_{SO}\left(1 + q^2a^2/4\right), \end{aligned} \tag{4.16}$$

with all other components vanishing. In this limit, the system is equivalent to the BHZ model, the Hamiltonian decomposes into 2×2 blocks which read

$$H = \begin{pmatrix} \lambda_\nu - \left(1 + \frac{q^2a^2}{4}\right) 3\sqrt{3}\lambda_{SO} & -\frac{\sqrt{3}ta}{2}\left(q_x - iq_y\right) \\ -\frac{\sqrt{3}ta}{2}\left(q_x + iq_y\right) & -\lambda_\nu + \left(1 + \frac{q^2a^2}{4}\right) 3\sqrt{3}\lambda_{SO} \end{pmatrix}. \tag{4.17}$$

This model can be mapped on the BHZ Hamiltonian as it is stated in [Groth09]. The parameters then read $\alpha = -\frac{\sqrt{3}ta}{2}$, $m = \lambda_\nu - 3\sqrt{3}\lambda_{SO}$, $\beta = -3\sqrt{3}\frac{\lambda_{SO}a^2}{4}$ and $\gamma = 0$. The integral in Eq. (4.9) to lowest order in W can be done analytically using certain approximations as in [Groth09]. This yields the renormalization of the parameter λ_ν as

$$\bar{\lambda}_\nu = \lambda_\nu + \frac{W^2}{9\pi\sqrt{3}\lambda_{SO}} \log\left| \frac{27\lambda_{SO}^2}{E_F^2 - (\lambda_\nu - 3\sqrt{3}\lambda_{SO})^2} \left(\frac{\pi}{2}\right)^4 \right|, \tag{4.18}$$

while λ_{SO} does not renormalize because it entered with a factor q^2 in the Hamiltonian as well, and Σ is supposed to be momentum independent. For the right parameters, the

logarithm in this equation can get negative, leading to a negative renormalization of λ_ν with growing W. In this case, it is possible that even though initially $\lambda_\nu > 3\sqrt{3}\lambda_{SO}$, one finds that $\bar{\lambda}_\nu < 3\sqrt{3}\lambda_{SO}$. Therefore, the system undergoes a topological transition with increasing W.

4.5 Conclusions

Within this chapter, we investigated the effect of a topological Anderson insulator (TAI) in the Kane-Mele model for the first time. TAIs are topological insulators that are generated by a finite disorder potential (with strength W) in systems that would be trivially insulating in the clean limit. First, we showed that the effect exists not only in the Bernevig Hughes Zhang model but as well in the Kane-Mele model on a 2D honeycomb lattice. Different parameter regimes of the model have been explored and the critical energy scales approximated and compared to experimentally feasible values. This indicates that a TAI can most likely not be realized in graphene, but possibly in silicene, germanene or stanene.

We found that the system needs to be of a certain size to show the effect, which is of the order of 100×100 lattice sites. Besides the second nearest neighbor spin-orbit coupling (λ_{SO}), Rashba spin-orbit coupling (λ_R) and the staggered sublattice potential (λ_ν) are important ingredients for the effect. The numerical data shows that a TAI is found in the parameter region with $\lambda_R < 2\sqrt{3}\lambda_{SO}$ and $\lambda_\nu \gtrsim 3\sqrt{3}\lambda_{SO}$. A phase diagram was generated numerically for $\lambda_{SO} = 0.3t$ (t as the hopping amplitude) that illustrates for which λ_R, λ_ν combination a topological insulator, an ordinary insulator, a metal or a TAI can develop due to the disorder. Interestingly, the TAI does not exist for small λ_ν and $\lambda_R \approx 2\sqrt{3}\lambda_{SO}$, for which a continuous transformation of the topological insulator into a metal exists. Besides Anderson disorder, also spatially correlated disorder is investigated. Up to a small correlation length of about the lattice constant, the TAI is visible also for spatially correlated disorder.

An analytical model sheds light on the physics behind the TAI effect. Within the self-consistent Born approximation (SCBA), many features can be explained quantitatively. A lowest order expansion in the disorder potential W is enough to describe the boundaries of the inverted gap of the TAI for $\lambda_R = 0$. We observed a good agreement between the Born approximation and the direct numerical solution of the tight-binding model with disorder. For this, no adjustable parameter has to be used if the disorder potential in the Born approximation is chosen to be $W_{SCBA} = \sqrt{W^2/3}$. This however is plausible, as $W^2/3$ is the second moment of the disorder potential for Anderson disorder. A general understanding is that the disorder results in a renormalization of the system parameters and can lead to an effectively decreased λ_ν. This can lead to the closing of the trivial gap and re-opening of a topological gap.

In the case of finite λ_R, the Born approximation approach does not work as well anymore. General considerations can be made, however. It is found that λ_R does not renormalize with W. Instead, a new coupling λ_{R3} has to be introduced. Interestingly, λ_{R3} strengthens the topological phase and by itself can induce a topological transition as it can shift the closing of the topological gap to larger values of λ_ν.

An interesting open question that remains for the future is to better understand the effect of non-Anderson-like disorder. First calculations hint to the possibility that one characteristic feature that a disorder realization has to suffice so that the TAI effect is visible is that the second moment of the disorder potential has to be large enough. This can

be achieved either by dense, but weak disorder potentials or by dilute, strong potentials. The latter case is probably more relevant for experiments and should be investigated.

Chapter 5

Conclusions

This thesis consists of three independent chapters, which deal with different phenomena in topological insulators that are generated by a broken spin axis symmetry. This exists while time-reversal symmetry (TRS) is conserved. The symmetry breaking terms arise for example due to Rashba spin-orbit coupling, as in Chapter 4, and can be mathematically included using the concept of generic helical liquids, as in Chapter 2 and Chapter 3.

In Chapter 2, we investigated a narrow two-dimensional (2D) topological insulator. Under the influence of an inhomogeneous, perpendicular external electric field Rashba spin-orbit coupling is induced in the edge states on the sides of a sample. This is taken into account by utilizing the concept of generic helical liquids in two effective one-dimensional models. Therefore, we introduced two momentum dependent rotation matrices $B_{k,U}$ and $B_{k,L}$. The inhomogeneity ensures that the two matrices, and the Hamiltonian eigenstates of the two edges are distinct. As the sample is assumed to be rather narrow, the bulk supports several tunnel contacts that connect the two edges, and in conjunction with the different eigenstates allow for forward scattering and backscattering of the edge states. We found that in this setup, a change of the external field has a strong impact on the conductance of the sample. In the case that only two tunnel contacts are present, interference phenomena can be seen. For an elongated and narrow sample hosting several tunnel contacts, the full conductance is calculated and evaluated on average. This yields a inverted localization length of $\ell^{-1} = n\langle T\rangle \cos^2\left[\theta(\mu)\right]$, were n is the tunnel contact density, $\langle T\rangle$ the averaged tunnel amplitude and $\theta(\mu)$ characterizes the field inhomogeneity as a function of the chemical potential μ. This allows a measurement of the spin structure of the helical edge states. However, the application of this theory requires that the sample geometry and several other physical quantities are in a suitable parameter range.

In Chapter 3 we investigated the edge states of 2D topological insulators that are gapped out by either strong interactions or induced superconductivity. At the interface of two such regions, we found exotic bound states, so called non-Abelian parafermions. The electron-electron interactions are taken into account in Luttinger liquid theory and the edge states are described using generic helical liquids. In this chapter, we first showed that the combination of interactions and generic helical liquids generates a new interaction term, called umklapp scattering. Using a second order RG treatment, the flow equations of this term are derived. They read $dg_{\mathrm{um}}/d\ell = -2g_{\mathrm{um}}(2K-1) + \lambda^2\pi^2(K-3)\,(2K-1)\,(K-5)$, were $g_{um}(\ell)$ is the umklapp scattering strength and $d\lambda/d\ell = -(K+1)\lambda$ is the flow equation for the dimensionless parameter λ, which is related to the B_k matrix of the generic helical liquid. This result reveals that the considered kind of umklapp scattering gets relevant for strong interactions $K < 1/2$ (K being the Luttinger liquid parameter). The umklapp

scattering leads to a gap in the edge state spectrum. This is succeeded by a calculation based on bosonic Green's functions of a single interface between an edge state region that is gapped out by g_{um} and one which is gapped out by induced superconductivity. Refermionization discloses a pole in the fermionic Green's function, $G(\omega) \propto 2/(\omega + i0_+)$, at zero energy. This pole represents a zero energy bound state at the interface. With these results in mind, we extended the system to a circular setup, hosting $2N$ such interfaces. We found that this system has a N^4-fold ground state degeneracy. Effective operators are constructed that allow to cycle through the ground state manifold by creating/annihilating non-local electronic particles. It is shown that these operators satisfy $\chi_{2j}^4 = \chi_{2j-1}^4 = 1$. Furthermore, a braiding scheme is proposed that allows for non-Abelian braiding of these particles. Finally, we examine the Josephson effect in this setup, it shows a periodicity of 8π in the current. The system considered here is TRS conserving, which is a distinguishing feature as compared to other works realizing parafermions. For example, in contrast to proposals based on the fractional quantum hall (FQH) effect, it does not require the coexistence of a strong magnetic field and superconductivity. This can be an advantage for potential experiments.

Chapter 4 deals with disorder in the Kane-Mele model. In analogy to works based on the Bernevig Hughes Zhang (BHZ) model, we have shown that disorder can induce a topological phase, even though the clean sample model parameters belong to a trivial insulating phase. Besides the numerical solution of the tight-binding model, this chapter presents an analytical approach, based on the lowest-order Born approximation. This approach reveals that the model parameters get renormalized due to the disorder. We found that the renormalized staggered sublattice potential, λ_ν, gets decreased with growing disorder strength W. On the other hand, the spin-orbit coupling, λ_{SO}, does not renormalize. Therefore, a topological transition can take place as the condition for a topological phase is given by $\lambda_\nu < 3\sqrt{3}\lambda_{SO}$, if there is no Rashba spin-orbit coupling. Interestingly, the Rashba spin-orbit coupling λ_R is not renormalized to lowest order in W, instead a new, anisotropic Rashba coupling is generated, λ_{R3}. This coupling breaks the discrete C_3 rotation symmetry (rotation through an angle of 120°). Furthermore, we investigated the effect of spatially correlated disorder. While these results might not be relevant for graphene, the most prominent material for which the Kane-Mele model applies, they might be relevant for silicene, germanene or stanene. In these setups, disorder can be used to tune the system artificially between a trivial insulating and a topological insulating phase. This could possibly be utilized for new electronic applications.

Topological insulators are the foundation of an incredibly rich ensemble of phenomena and effects, three of which have been the subject of this thesis. With the knowledge that was gained during its writing, our understanding of these materials has substantially widened. The narrow 2D topological insulator setup that has been investigated allows a measurement and resolution of the spin-structure of the edge states. The non-Abelian parafermions that were found are new, possible candidates for the implementation of quantum computation. Finally, the TAI that was discovered in the Kane-Mele model broadens the range of possible materials that can be used as topological insulators or allow tuning of a material between a trivial and topological phase through doping with impurities. Together with the manifold of other works about topological insulators that have been published in the last years, this gives hope that topological insulators will find many applications and will let us understand nature at an even more profound level.

Appendix A

General Formulas

Fourier Transforms

$$\psi(x) = \frac{1}{L}\sum_k e^{ikx}\psi_k \qquad\qquad \psi_k = \int \mathrm{d}x e^{-ikx}\psi(x). \tag{A.1}$$

Normal ordering

$$:ABC\ldots: = ABC\cdots - \langle ABC\ldots\rangle. \tag{A.2}$$

Logarithm expressed as a sum

$$\log(1-y) = -\sum_{n=1}^{\infty} y^n/n. \tag{A.3}$$

Bosonization identity (Eq. 2.22 of [Giamarchi03])

$$\psi_\sigma(x) = U_\sigma \lim_{a\to 0}\frac{1}{\sqrt{2\pi a}} e^{i\sigma(k_F-\pi/L)x} e^{-i(\sigma\phi(x)-\theta(x))}, \tag{A.4}$$

with the Klein factors defined as Majorana particles: $U_\uparrow = U_\uparrow^\dagger$ and $U_\downarrow = U_\downarrow^\dagger$.
Unit-step function

$$\theta(x) = \begin{cases} 0 & \text{if } x < 0 \\ 1 & \text{if } x \geq 0 \end{cases} \tag{A.5}$$

Sign function

$$\mathrm{sign}(x) = \begin{cases} -1 & \text{if } x < 0 \\ 0 & \text{if } x = 0 \\ 1 & \text{if } x > 0 \end{cases} \tag{A.6}$$

Appendix B

Detailed calculations

B.1 Proof that the modulus $|v_j|$ is indeed always less than one

This appendix is used to show that the modulus $v_j = \left|c_j/(a_j b_j)\right|$ is always smaller than 1. As a first step, a transfer matrix with $a_{j-1}, b_{j-1}, c_{j-1}$ and the form of Eq. (2.47) is multiplied by P_j. This yields for the resulting elements $a'_{j-1}, b'_{j-1}, c'_{j-1}$

$$\begin{aligned} a'_{j-1} &= a_{j-1}e^{i\phi_j} \\ b'_{j-1} &= b_{j-1} \\ c'_{j-1} &= c_{j-1}e^{-i\phi_j} \end{aligned}$$

and especially $v'_{j-1} = v_{j-1}$. Now a transfer matrix with coefficients $a'_{j-1}, b'_{j-1}, c'_{j-1}$ is multiplied by a single point contact transfer matrix with tunneling probability T_j which will result in (not writing the angle ϑ_j and the indices of $T_j, a'_{j-1}, b'_{j-1}, c'_{j-1}$ to keep it short)

$$\begin{aligned} a_j &= \frac{\left(1 + b\sin(\theta)\Gamma\right)\left(ab\sqrt{T} + cT\cos(\theta)\right)}{b(1 - T\cos^2(\theta))\Gamma} \\ b_j &= \frac{b - \sin(\theta)\Gamma}{1 + b\sin(\theta)\Gamma} \\ c_j &= \frac{\left(b - \sin(\theta)\Gamma\right)\left(abT\cos(\theta) + c\sqrt{T}\right)}{b(1 - T\cos^2(\theta))\Gamma} \\ \Gamma &= \sqrt{\frac{T}{1-T}}, \end{aligned}$$

as the parameters of the new transfer matrix. This gives for the modulus

$$\begin{aligned} v_j &= \left| \frac{\left(b - \sin(\theta)\Gamma\right)\left(abT\cos(\theta) + c\sqrt{T}\right) b(1 - T\cos^2(\theta))\Gamma\left(1 + b\sin(\theta)\Gamma\right)}{b(1 - T\cos^2(\theta))\Gamma\left(1 + b\sin(\theta)\Gamma\right)\left(ab\sqrt{T} + cT\cos(\theta)\right)\left(b - \sin(\theta)\Gamma\right)} \right| \\ &= \left| \frac{\sqrt{T}\cos(\theta) + c/ab}{1 + \sqrt{T}\cos(\theta)c/ab} \right|. \end{aligned}$$

With an arbitrary phase φ it can be written as

$$v_j = \left| \frac{\sqrt{T}\cos(\theta) + v_{j-1}e^{i\varphi}}{1 + v_{j-1}e^{i\varphi}\sqrt{T}\cos(\theta)} \right| = \sqrt{\frac{\left(\sqrt{T}\cos(\theta) + v_{j-1}\cos(\varphi)\right)^2 + v_{j-1}^2\sin^2(\varphi)}{\left(1 + v_{j-1}\cos(\varphi)\sqrt{T}\cos(\theta)\right)^2 + v_{j-1}^2\sin^2(\varphi)T\cos^2(\theta)}}$$

expanding the powers shows that $1+v_{j-1}^2 T\cos^2(\theta) > v_{j-1}^2 + T\cos^2(\theta)$ is needed for $v_j < 1$ if $\cos(\theta)\cos(\phi) > 0$. This however is true as $-\left(1 - T\cos^2(\theta)\right)\left(1 - v_{j-1}^2\right) < 0$. We therefore showed that if all the point contacts have $\left|v_j\right| < 0$ this is also true for the total transfer matrix. The proof is not complete yet, as the case $\cos(\theta)\cos(\phi) < 0$ is not covered. However, it can be seen easily by plotting that $v_j < 1$ even in this case, and an exact mathematical proof has to be done elsewhere.

B.2 Bosonization of kinetic energy Hamiltonian

As an introduction to the methodology the linear dispersion Hamiltonian is bosonized (which turns out to be really tricky to get it right) in this appendix. This part is closely related to [vonDelft98] and starts with the Hamiltonian for free fermions

$$H_0 = -iv_F \sum_{\sigma=R,L} \sigma \int_{-L/2}^{L/2} \mathrm{d}x \,{}^*_* \psi_\sigma^\dagger(x)\partial_x\psi_\sigma(x) {}^*_* + \mathrm{H.c.} \tag{B.1}$$

with Fermi velocity v_F and the right/left moving fields ψ_R, ψ_L ($R, L = \pm$). The expression $({}^*_* \ldots {}^*_*)$ denotes the fermionic normal ordering, which is to prevent singularities originating from a linearized spectrum with an infinite number of occupied states below the Fermi energy. It is defined as usual by

$${}^*_* ABC \ldots {}^*_* = ABC\cdots - \langle ABC \ldots \rangle \tag{B.2}$$

where $\langle |, | \rangle$ is the (N-particle) ground state without any particle hole excitations. In this appendix the bosonization identity (A.4) is used, which is a Hamiltonian independent and exact operator identity. Furthermore, the definition $\varphi_\sigma(x) = \sigma\phi(x) - \theta(x)$ will turn out to be handy. U_σ is the Klein factor and k_F the Fermi momentum. The system has a finite length L and an infinitesimal regularization parameter a. $\phi(x), \theta(x)$ are the bosonized fields. The fields $\varphi_\sigma(x)$ are defined by, after [Giamarchi03],

$$\begin{aligned}\varphi_\sigma(x) = &-(\sigma N_R + N_R - \sigma N_L - N_L)\frac{\pi x}{L} \\ &- \frac{i\pi}{L}\sum_p \left(\frac{L|p|}{2\pi}\right)^{1/2} e^{-a|p|/2 - ipx}\left(\frac{\sigma b_p^\dagger + \sigma b_{-p}}{p} + \frac{b_p^\dagger - b_{-p}}{|p|}\right).\end{aligned} \tag{B.3}$$

It is furthermore necessary to split the fields into creation and annihilation parts, $\varphi_\sigma(x) = \varphi_\sigma^+(x) + \varphi_\sigma^-(x)$, using only the creation part and annihilation part of the b-operators, which commute with themselves. With this the following important commutators can be

calculated

$$\left[\varphi_R(x),\varphi_L(x)\right]=0 \tag{B.4}$$

$$\begin{aligned}\left[\varphi_\sigma^+(x),\varphi_{\sigma'}^-(x')\right] &= -\frac{\pi}{2L}\sum_{p,p'}\sqrt{|p||p'|}e^{-a|p|/2-a|p'|/2-ipx-ip'x'}\underbrace{\left[\frac{\sigma b_p^\dagger}{p}+\frac{b_p^\dagger}{|p|},\frac{\sigma' b_{-p'}}{p'}+\frac{-b_{-p'}}{|p'|}\right]}_{\delta_{p,-p'}\frac{1}{p^2}\left(\sigma\sigma'+(\sigma+\sigma')\mathrm{sign}(p)+1\right)}\\ &= -\frac{\pi}{2L}\sum_p e^{-a|p|-ip(x-x')}\frac{1}{|p|}\left(\sigma\sigma'+(\sigma+\sigma')\mathrm{sign}(p)+1\right)\\ &= -\frac{2\pi}{L}\delta_{\sigma,\sigma'}\sum_p e^{-a|p|-ip(x-x')}\frac{\theta(\sigma p)}{|p|}\end{aligned} \tag{B.5}$$

where it was used that the N_σ commute with each other and with the b-operators. In the following the identity of Eq. (A.3) and the momentum quantization $k=\frac{2\pi}{L}n_k$ is used to calculate

$$\begin{aligned}\left[\varphi_\sigma^+(x),\varphi_{\sigma'}^-(x')\right] &= -\frac{2\pi}{L}\delta_{\sigma\sigma'}\sum_{n_p=1}^{\infty}e^{-(a+i\sigma(x-x'))\frac{2\pi}{L}n_p}\frac{L}{2\pi n_p}\\ &= \delta_{\sigma\sigma'}\log\left[1-e^{-(a+i\sigma(x-x'))\frac{2\pi}{L}}\right].\end{aligned} \tag{B.6}$$

It is furthermore found that for both $\eta=\pm$ the following commutator holds as well

$$\left[\varphi_\sigma^\eta(x'),\partial_x\varphi_{\sigma'}^\eta(x)\right]=0. \tag{B.7}$$

To bosonize the kinetic energy, the derivative has to be written as the limit

$$:\psi_\sigma^\dagger(x)i\partial_x\psi_\sigma(x):+\text{H.c.}=i\lim_{\epsilon\to0}\frac{1}{\epsilon}:\psi_\sigma^\dagger(x)\psi_\sigma(x+\epsilon)-\psi_\sigma^\dagger(x)\psi_\sigma(x):+\text{H.c.}. \tag{B.8}$$

Here, it is already crucial to take the H.c. into account in the right way. For this reason it makes sense to also keep writing the i. Writing out the H.c. yields

$$\begin{aligned}&:\psi_\sigma^\dagger(x)i\partial_x\psi_\sigma(x):+\text{H.c.}\\ &\quad= i\lim_{\epsilon\to0}\frac{1}{\epsilon}:\psi_\sigma^\dagger(x)\psi_\sigma(x+\epsilon)-\psi_\sigma^\dagger(x)\psi_\sigma(x)-\psi_\sigma^\dagger(x+\epsilon)\psi_\sigma(x)+\psi_\sigma^\dagger(x)\psi_\sigma(x):\\ &\quad= i\lim_{\epsilon\to0}\frac{1}{\epsilon}:\psi_\sigma^\dagger(x)\psi_\sigma(x+\epsilon)-\psi_\sigma^\dagger(x+\epsilon)\psi_\sigma(x):.\end{aligned} \tag{B.9}$$

Here, products of two operators at the same point x are allowed and well defined because they are inside the normal ordering operation, which prevents any singularities. With the bosonization identity the normal ordered operator products can be calculated as

$$\begin{aligned}:\psi_\sigma^\dagger(x)\psi_\sigma(x+\epsilon):&=\lim_{a\to0}\frac{1}{2\pi a}e^{i\sigma(k_F-\pi/L)\epsilon}:e^{i\varphi_\sigma(x)}e^{-i\varphi_\sigma(x+\epsilon)}:\\ :\psi_\sigma^\dagger(x+\epsilon)\psi_\sigma(x):&=\lim_{a\to0}\frac{1}{2\pi a}e^{-i\sigma(k_F-\pi/L)\epsilon}:e^{i\varphi_\sigma(x+\epsilon)}e^{-i\varphi_\sigma(x)}:\end{aligned} \tag{B.10}$$

where it was used that the Klein factors are unitary. Before taking the limit $\epsilon\to0$ the limit $a\to0$ has to be taken as a is supposed to be even smaller than ϵ. This is because a is a measure for the length scale beyond which dynamics are cut-off. At distances smaller

than a, the fields are not supposed to vary anymore, and taking the derivative would make no sense. To do this, the fields have to be rearranged in a final way that does not require the use of commutators after taking the limit $a \to 0$, because commutators contain a. With the fields $\varphi_\sigma^\pm$ and the commutator Eq. (B.6) one finds

$$\begin{aligned}
{}^*_*\psi_\sigma^\dagger(x)\psi_\sigma(x+\epsilon){}^*_* &= \lim_{a\to 0}\frac{1}{2\pi a}e^{i\sigma(k_F-\pi/L)\epsilon}\,{}^*_*e^{i\varphi_\sigma^+(x)+i\varphi_\sigma^-(x)}e^{-i\varphi_\sigma^+(x+\epsilon)-i\varphi_\sigma^-(x+\epsilon)}{}^*_* \\
&= \lim_{a\to 0}\frac{1}{2\pi a}e^{i\sigma(k_F-\pi/L)\epsilon}\,{}^*_*e^{i\varphi_\sigma^+(x)}e^{+i\varphi_\sigma^-(x)}e^{-i\varphi_\sigma^+(x+\epsilon)}e^{-i\varphi_\sigma^-(x+\epsilon)} \\
&\quad\times e^{\left[\varphi_\sigma^+(x),\varphi_\sigma^-(x)\right]/2}e^{\left[\varphi_\sigma^+(x+\epsilon),\varphi_\sigma^-(x+\epsilon)\right]/2}{}^*_* \\
&= \lim_{a\to 0}\frac{1}{2\pi a}e^{i\sigma(k_F-\pi/L)\epsilon}\,{}^*_*e^{i\varphi_\sigma^+(x)}e^{-i\varphi_\sigma^+(x+\epsilon)}e^{+i\varphi_\sigma^-(x)}e^{-i\varphi_\sigma^-(x+\epsilon)} \\
&\quad\times e^{\left[\varphi_\sigma^-(x),\varphi_\sigma^+(x+\epsilon)\right]}e^{\left[\varphi_\sigma^+(x),\varphi_\sigma^-(x)\right]}{}^*_*. \qquad \text{(B.11)}
\end{aligned}$$

Finally, one can take the limit $a \to 0$ of the whole expression, including the prefactor $1/a$ and the two commutators. This yields

$$\begin{aligned}
\lim_{a\to 0}\frac{1}{2\pi a}e^{\left[\varphi_\sigma^-(x),\varphi_\sigma^+(x+\epsilon)\right]}e^{\left[\varphi_\sigma^+(x),\varphi_\sigma^-(x)\right]} &= \lim_{a\to 0}\frac{1}{2\pi a}\frac{1-e^{-a\frac{2\pi}{L}}}{1-e^{-(a+i\sigma\epsilon)\frac{2\pi}{L}}} \\
&= \frac{1}{L}\frac{1}{1-e^{-2i\sigma\epsilon\pi/L}}. \qquad \text{(B.12)}
\end{aligned}$$

This can be expanded for small ϵ. Taylor expansion works the usual way because $\partial_x\varphi_\sigma(x)$ commutes with $\varphi_\sigma(x)$. First, all the terms are expanded up to second order in ϵ to read

$$\begin{aligned}
&{}^*_*\psi_\sigma^\dagger(x)\psi_\sigma(x+\epsilon){}^*_* \approx \\
&\quad {}^*_*\left[1-i\partial_x\varphi_\sigma^+(x)\epsilon - i\partial_x^2\varphi_\sigma^+(x)\epsilon^2/2 - \left(\partial_x\varphi_\sigma^+(x)\right)^2\epsilon^2/2\right] \\
&\quad\times\left[1-i\partial_x\varphi_\sigma^-(x)\epsilon - i\partial_x^2\varphi_\sigma^-(x)\epsilon^2/2 - \left(\partial_x\varphi_\sigma^-(x)\right)^2\epsilon^2/2\right] \\
&\quad\times\left[1+i\sigma(k_F-\pi/L)\epsilon - \frac{1}{2}(k_F-\pi/L)^2\epsilon^2\right]\left[-\frac{i\sigma}{2\pi\epsilon}+\frac{1}{2L}+\frac{i\pi\epsilon\sigma}{6L^2}\right]{}^*_*. \qquad \text{(B.13)}
\end{aligned}$$

Keeping in mind that there is still a $1/\epsilon$ prefactor before taking the limit, all terms going as ϵ^2 can be neglected. Furthermore, all terms not containing any operators can be dropped due to the normal ordering. This yields

$$\begin{aligned}
{}^*_*\psi_\sigma^\dagger(x)\psi_\sigma(x+\epsilon){}^*_* \approx &\left(-\frac{i\sigma}{2\pi\epsilon}+\frac{1}{2L}\right){}^*_* - i\partial_x\varphi_\sigma(x)\epsilon\,{}^*_* \\
&- \frac{i\sigma}{2\pi\epsilon}{}^*_* - i\partial_x^2\varphi_\sigma(x)\epsilon^2/2 - \left(\partial_x\varphi_\sigma^+(x)\right)^2\epsilon^2/2 - \left(\partial_x\varphi_\sigma^-(x)\right)^2\epsilon^2/2\,{}^*_* \\
&- \frac{i\sigma}{2\pi\epsilon}{}^*_* - \partial_x\varphi_\sigma^+(x)\partial_x\varphi_\sigma^-(x)\epsilon^2 + \partial_x\varphi_\sigma(x)\sigma(k_F-\pi/L)\epsilon^2\,{}^*_*. \qquad \text{(B.14)}
\end{aligned}$$

An analogous calculation for the hermitian conjugate yields (the limit $a \to 0$ now leads to a term $\frac{1}{L}\frac{1}{1-e^{2i\epsilon\sigma\pi/L}}$)

$$
\begin{aligned}
{}^{*}_{*}\psi^{\dagger}_{\sigma}(x+\epsilon)\psi_{\sigma}(x){}^{*}_{*} \approx & \left(\frac{i\sigma}{2\pi\epsilon}+\frac{1}{2L}\right){}^{*}_{*} i\partial_x\varphi_{\sigma}(x)\epsilon{}^{*}_{*} \\
& + \frac{i\sigma}{2\pi\epsilon}{}^{*}_{*} i\partial_x^2\varphi_{\sigma}(x)\epsilon^2/2 - \left(\partial_x\varphi^{+}_{\sigma}(x)\right)^2\epsilon^2/2 - \left(\partial_x\varphi^{-}_{\sigma}(x)\right)^2\epsilon^2/2{}^{*}_{*} \\
& + \frac{i\sigma}{2\pi\epsilon}{}^{*}_{*} - \partial_x\varphi^{+}_{\sigma}(x)\partial_x\varphi^{-}_{\sigma}(x)\epsilon^2 + \partial_x\varphi_{\sigma}(x)\sigma(k_F-\pi/L)\epsilon^2{}^{*}_{*}. \quad \text{(B.15)}
\end{aligned}
$$

Insertion of these expressions into the Hamiltonian of Eq. (B.1) and the limit $\epsilon \to 0$ yields

$$
\begin{aligned}
H_0 = & -iv_F\sum_{\sigma}\sigma\int_{-L/2}^{L/2}\mathrm{d}x{}^{*}_{*} - \frac{1}{2L}i\partial_x\varphi_{\sigma}(x){}^{*}_{*} \\
& - iv_F\sum_{\sigma}\int_{-L/2}^{L/2}\mathrm{d}x{}^{*}_{*}\frac{i}{2\pi}\left(\partial_x\varphi_{\sigma}(x)\right)^2 - \frac{i}{\pi}\partial_x\varphi_{\sigma}(x)(k_F-\pi/L){}^{*}_{*} \qquad \text{(B.16)}
\end{aligned}
$$

where it was used that $\left[\partial_x\varphi^{+}_{\sigma}(x), \partial_x\varphi^{-}_{\sigma}(x)\right]$ is a number and vanishes in the fermion normal ordered expression. In the limit of large L one can neglect most of the terms and obtain the well known bosonic Hamiltonian

$$
H_0 = \frac{v_F}{2\pi}\sum_{\sigma}\int \mathrm{d}x{}^{*}_{*}\left(\partial_x\varphi_{\sigma}(x)\right)^2{}^{*}_{*}. \qquad \text{(B.17)}
$$

B.3 Majorana modes at the edges of 2D topological insulators with induced gaps

Consider the Hamiltonian $H = H_0 + H_\Delta + H_M$. It consists of a kinetic part with linear spectrum as in Eq. (3.1), a part with induced superconducting pairing Eq. (3.6) and one with induced magnetic pairing Eq. (3.8),

$$
\begin{aligned}
H_0 &= -iv_F\sum_{\sigma}\sigma\int dx\Psi^{\dagger}_{\sigma}(x)\partial_x\Psi_{\sigma}(x) \\
H_\Delta &= \int dx\left[\Delta(x)\Psi^{\dagger}_{\uparrow}(x)\Psi^{\dagger}_{\downarrow}(x) + \text{H.c.}\right] \\
H_M &= \int dx\left[M(x)\Psi^{\dagger}_{\uparrow}(x)\Psi_{\downarrow}(x) + \text{H.c.}\right] \qquad \text{(B.18)}
\end{aligned}
$$

where $\Delta(x) = \Delta\theta(-x)$ and $M(x) = M\theta(x)$. Introducing the Nambu spinor,

$$
\mathbf{\Psi} = [\Psi_{\uparrow}(x), \Psi_{\downarrow}(x), \Psi^{\dagger}_{\downarrow}(x), -\Psi^{\dagger}_{\uparrow}(x)]^T \qquad \text{(B.19)}
$$

it can be written as

$$
H = \frac{1}{2}\int dx\mathbf{\Psi}^{\dagger}(x)\begin{pmatrix} -iv_F\partial_x & M & \Delta & 0 \\ M^* & iv_F\partial_x & 0 & \Delta \\ \Delta^* & 0 & iv_F\partial_x & M \\ 0 & \Delta^* & M^* & -iv_F\partial_x \end{pmatrix}\mathbf{\Psi}(x). \qquad \text{(B.20)}
$$

B.3.1 Solution in the superconducting region

As a first step, the solution in the superconducting region ($x < 0$) is considered. Here, the Schrodinger equation reads

$$\begin{pmatrix} -iv_F\partial_x & 0 & \Delta & 0 \\ 0 & iv_F\partial_x & 0 & \Delta \\ \Delta^* & 0 & iv_F\partial_x & 0 \\ 0 & \Delta^* & 0 & -iv_F\partial_x \end{pmatrix} \mathbf{\Psi}_<(x) = E\mathbf{\Psi}_<(x) \tag{B.21}$$

This first order differential equation can be solved with the ansatz,

$$\mathbf{\Psi}_<(x) = \begin{pmatrix} e^{ik_\uparrow x}c_\uparrow \\ e^{ik_\downarrow x}c_\downarrow \\ e^{ik_\uparrow x}d_\downarrow \\ e^{ik_\downarrow x}d_\uparrow. \end{pmatrix} \tag{B.22}$$

Using this gives the equations

$$\begin{pmatrix} v_Fk_\uparrow - E & \Delta & 0 & 0 \\ \Delta^* & -v_Fk_\uparrow - E & 0 & 0 \\ 0 & 0 & -v_Fk_\downarrow - E & \Delta \\ 0 & 0 & \Delta^* & v_Fk_\downarrow - E \end{pmatrix} \begin{pmatrix} c_\uparrow \\ d_\downarrow \\ c_\downarrow \\ d_\uparrow \end{pmatrix} = 0. \tag{B.23}$$

This matrix is block diagonal, and its eigenenergies are given by

$$E_{\sigma\pm} = \pm\sqrt{(v_Fk_\sigma)^2 + |\Delta|^2}. \tag{B.24}$$

This allows to determine the eigenvectors. For instance, it is found

$$(v_Fk_\uparrow - E_{\uparrow\pm})c_\uparrow + \Delta d_\downarrow = 0 \quad \Longrightarrow \quad d_{\downarrow,\pm} = \frac{c_\uparrow}{\Delta}\left[\pm\sqrt{(v_Fk_\uparrow)^2 + |\Delta|^2} - v_Fk_\uparrow\right] \tag{B.25}$$

Therefore, defining

$$\alpha_{\sigma\pm} = \frac{1}{\Delta}\left[\pm\sqrt{(v_Fk_\sigma)^2 + |\Delta|^2} - v_F\sigma k_\sigma\right] \tag{B.26}$$

the (unnormalized) eigenvectors corresponding to the four eigenvalues $E_{\sigma\pm}$ are given by

$$e^{ik_\uparrow x}\begin{pmatrix} 1 \\ 0 \\ \alpha_{\uparrow+} \\ 0 \end{pmatrix}, \quad e^{ik_\uparrow x}\begin{pmatrix} 1 \\ 0 \\ \alpha_{\uparrow-} \\ 0 \end{pmatrix}, \quad e^{ik_\downarrow x}\begin{pmatrix} 0 \\ 1 \\ 0 \\ \alpha_{\downarrow+} \end{pmatrix}, \quad e^{ik_\downarrow x}\begin{pmatrix} 0 \\ 1 \\ 0 \\ \alpha_{\downarrow-} \end{pmatrix}. \tag{B.27}$$

Since normalization was not imposed so far, k_σ can be either real or imaginary (it cannot have nonzero real and imaginary parts, because the energy must be real). Real k_σ corresponds to states with energy above $|\Delta|$, whereas imaginary $k_\sigma = i\kappa_\sigma$ can generate subgap states, provided that $v_F^2\kappa_\sigma^2 < |\Delta|^2$.

In the following, the focus is put on possible zero energy eigenstates. Since the wave function must be convergent for $x \to -\infty$, $\kappa_\sigma < 0$ has to hold. There is thus a unique wave vector $\kappa_\sigma = -|\Delta|/v_F$ which can yield a zero energy solution. In that case

$$\alpha_{\sigma\pm}\big|_{k_\sigma = -i|\Delta|/v_F} = \frac{1}{\Delta}(\sigma i|\Delta|) = i\sigma e^{-i\phi} \tag{B.28}$$

with $\Delta = |\Delta| e^{i\phi}$. The most general wave function corresponding to that solution reads

$$\mathbf{\Psi}_{<}^{(0)}(x) = e^{x|\Delta|/v_F} \left[a_\uparrow \begin{pmatrix} 1 \\ 0 \\ ie^{-i\phi} \\ 0 \end{pmatrix} + a_\downarrow \begin{pmatrix} 0 \\ 1 \\ 0 \\ -ie^{-i\phi} \end{pmatrix} \right] \tag{B.29}$$

For arbitrary $a_\uparrow$ and $a_\downarrow$, this state is a zero energy eigenstate and it is normalizable in the interval $(-\infty, 0]$.

B.3.2 Solution in the magnetic region

In the magnetic region ($x > 0$), the Schrodinger equation reads

$$\begin{pmatrix} -iv_F\partial_x & M & 0 & 0 \\ M^* & iv_F\partial_x & 0 & 0 \\ 0 & 0 & iv_F\partial_x & M \\ 0 & 0 & M^* & -iv_F\partial_x \end{pmatrix} \mathbf{\Psi}_{>}(x) = E\mathbf{\Psi}_{>}(x). \tag{B.30}$$

This first order differential equation can be solved with the ansatz,

$$\mathbf{\Psi}_{>}(x) = \begin{pmatrix} e^{ik_1 x} c'_\uparrow \\ e^{ik_1 x} c'_\downarrow \\ e^{ik_{-1} x} d'_\downarrow \\ e^{ik_{-1} x} d'_\uparrow \end{pmatrix} \tag{B.31}$$

Using this yields the equations

$$\begin{pmatrix} v_F k_1 - E & M & 0 & 0 \\ M^* & -v_F k_1 - E & 0 & 0 \\ 0 & 0 & -v_F k_{-1} - E & M \\ 0 & 0 & M^* & v_F k_{-1} - E \end{pmatrix} \begin{pmatrix} c'_\uparrow \\ c'_\downarrow \\ d'_\downarrow \\ d'_\uparrow \end{pmatrix} = 0. \tag{B.32}$$

The eigenenergies are this time given by (for $j = \pm 1$),

$$F_{j,\pm} = \pm\sqrt{(v_F k_i)^2 + |M|^2}. \tag{B.33}$$

And the eigenvectors read

$$(v_F k_1 - F_{1,\pm}) c_\uparrow + M c_\downarrow = 0 \quad \Longrightarrow \quad c_{\downarrow,\pm} = \frac{c_\uparrow}{M} \left[\pm\sqrt{(v_F k_1)^2 + |M|^2} - v_F k_1 \right]. \tag{B.34}$$

Therefore, defining

$$\beta_{j,\pm} = \frac{1}{M} \left[\pm\sqrt{(v_F k_j)^2 + |M|^2} - v_F j k_j \right] \tag{B.35}$$

the (unnormalized) eigenvectors corresponding to the four eigenvalues are given by

$$e^{ik_1 x} \begin{pmatrix} 1 \\ \beta_{1+} \\ 0 \\ 0 \end{pmatrix}, \quad e^{ik_1 x} \begin{pmatrix} 1 \\ \beta_{1-} \\ 0 \\ 0 \end{pmatrix}, \quad e^{ik_{-1} x} \begin{pmatrix} 0 \\ 0 \\ 1 \\ \beta_{-1,+} \end{pmatrix}, \quad e^{ik_{-1} x} \begin{pmatrix} 0 \\ 0 \\ 1 \\ \beta_{-1,-} \end{pmatrix}. \tag{B.36}$$

It is again look at zero energy eigenstates. These must correspond to imaginary $k_j = i\kappa_j$, and normalizability means that $\kappa_j > 0$. This means that $\kappa_j = |M|/v_F$ is the only allowed wave vector. For that case, it is found

$$\beta_{j,\pm} = \frac{1}{M}(-ij|M|) = -ije^{-i\theta} \tag{B.37}$$

where $M = |M|e^{i\theta}$ was used. Therefore, the most general zero energy eigenstate reads

$$\mathbf{\Psi}^{(0)}_{>}(x) = e^{-x|M|/v_F}\left[b_\uparrow \begin{pmatrix} 1 \\ -ie^{-i\theta} \\ 0 \\ 0 \end{pmatrix} + b_\downarrow \begin{pmatrix} 0 \\ 0 \\ 1 \\ ie^{-i\theta} \end{pmatrix}\right] \tag{B.38}$$

B.3.3 Matching the solutions

Finally, the possible zero energy solution at $x = 0$ have to be matched. Using

$$\mathbf{\Psi}^{(0)}_{<}(0) = \mathbf{\Psi}^{(0)}_{>}(0) \tag{B.39}$$

yields

$$\begin{pmatrix} 1 & 0 & -1 & 0 \\ 0 & 1 & ie^{-i\theta} & 0 \\ ie^{-i\phi} & 0 & 0 & -1 \\ 0 & -ie^{-i\phi} & 0 & -ie^{-i\theta} \end{pmatrix} \begin{pmatrix} a_\uparrow \\ a_\downarrow \\ b_\uparrow \\ b_\downarrow \end{pmatrix} = 0. \tag{B.40}$$

Nontrivial solutions exist if the determinant of this matrix is zero. This is indeed the case for arbitrary θ and ϕ. The rank of the matrix is three, so is has three linearly independent rows or columns. This means that one parameter can be chosen, say $a_\uparrow$, and used to determine the remaining three. For fixed $a_\uparrow$, the unique solution reads

$$\begin{aligned} a_\downarrow &= -ie^{-i\theta}a_\uparrow \\ b_\uparrow &= a_\uparrow \\ b_\downarrow &= ie^{-i\phi}a_\uparrow. \end{aligned} \tag{B.41}$$

The remaining parameter $a_\uparrow$ can in principle be fixed by the normalization. Therefore, the Majorana mode reads

$$\begin{aligned} \mathbf{\Psi}^{MBS}(x) &\propto \left[\theta(-x)e^{x|\Delta|/v_F} + \theta(x)e^{-x|M|/v_F}\right] \begin{pmatrix} 1 \\ -ie^{-i\theta} \\ ie^{-i\phi} \\ -e^{-i(\phi+\theta)} \end{pmatrix} \\ &= \left[\theta(-x)e^{x|\Delta|/v_F} + \theta(x)e^{-x|M|/v_F}\right] e^{-i\theta/2}e^{-i\phi/2} \begin{pmatrix} e^{i\theta/2}e^{i\phi/2} \\ -ie^{-i\theta/2}e^{i\phi/2} \\ ie^{i\theta/2}e^{-i\phi/2} \\ -e^{-i\theta/2}e^{-i\phi/2} \end{pmatrix} \end{aligned} \tag{B.42}$$

An overall phase was pulled out in the last line. The remaining spinor has the structure $(a, b, b^*, -a^*)$ which, when comparing it with the definition of the Nambu spinor, shows that this is indeed a self-adjoint fermionic mode.

B.3.4 Bosonization of the single-particle backscattering Hamiltonian

In order to bosonize the single-particle backscattering term properly, it is most convenient to express it in terms of fermions and use a point-split expression,

$$H_{int}^{spb} = \frac{2U_0}{k_0^2}\int dx \lim_{x_{1,2,3,4}\to x} \partial_{x_1}\sum_\alpha \left[\psi_\alpha^\dagger(x_1)\psi_\alpha(x_2) + \psi_\alpha^\dagger(x_2)\psi_\alpha(x_1)\right] \times\partial_{x_3}\sum_\beta \beta\left[\psi_\beta^\dagger(x_3)\psi_{\bar\beta}(x_4) - \psi_\beta^\dagger(x_4)\psi_{\bar\beta}(x_3)\right]. \tag{B.43}$$

As a first step the two terms in the product can be bosonized individually,

$$\begin{aligned}(*) &= \partial_x\sum_\beta \beta\left[\psi_\beta^\dagger(x)\psi_{\bar\beta}(y) - (x\leftrightarrow y)\right] = \frac{1}{2\pi a}\partial_x\sum_\beta\beta\left[e^{i\varphi_\beta(x)}e^{-i\varphi_{\bar\beta}(y)} - (x\leftrightarrow y)\right]\\ &= \frac{1}{2\pi a}\partial_x\sum_\beta\beta\left[e^{iK_+\tilde\varphi_\beta(x)}e^{iK_-\tilde\varphi_{\bar\beta}(x)}e^{-iK_+\tilde\varphi_{\bar\beta}(y)}e^{-iK_-\tilde\varphi_\beta(y)} - (x\leftrightarrow y)\right]\\ &= \frac{1}{2\pi a}\partial_x\sum_\beta\beta\left[e^{iK_+\tilde\varphi_\beta(x)}e^{-iK_-\tilde\varphi_\beta(y)}e^{iK_-\tilde\varphi_{\bar\beta}(x)}e^{-iK_+\tilde\varphi_{\bar\beta}(y)} - (x\leftrightarrow y)\right]\end{aligned} \tag{B.44}$$

where the following was used

$$\begin{aligned}\varphi_\sigma &= \sigma\phi - \theta = \sigma\sqrt{K}\tilde\phi - \frac{1}{\sqrt{K}}\tilde\theta\\ &= \frac{\sigma\sqrt{K}}{2}(\tilde\varphi_+ - \tilde\varphi_-) + \frac{1}{2\sqrt{K}}(\tilde\varphi_+ + \tilde\varphi_-)\\ &= \left(\frac{\sigma\sqrt{K}}{2} + \frac{1}{2\sqrt{K}}\right)\tilde\varphi_+ + \left(-\frac{\sigma\sqrt{K}}{2} + \frac{1}{2\sqrt{K}}\right)\tilde\varphi_-\\ &= \left(\frac{\sqrt{K}}{2} + \frac{1}{2\sqrt{K}}\right)\tilde\varphi_\sigma + \left(-\frac{\sqrt{K}}{2} + \frac{1}{2\sqrt{K}}\right)\tilde\varphi_{\bar\sigma}\\ &= K_+\tilde\varphi_\sigma + K_-\tilde\varphi_{\bar\sigma}\end{aligned} \tag{B.45}$$

to express the operator in terms of $\tilde\varphi_\pm$. Normal ordering for pairs produces,

$$e^{iK_+\tilde\varphi_\beta(x)}e^{-iK_-\tilde\varphi_\beta(y)} = \left(\frac{L}{2\pi a}\right)^{-(K_+^2+K_-^2)/2}\left(\frac{2\pi i\beta(y-x)}{L}\right)^{-K_+K_-}{}^*_*\, e^{iK_+\tilde\varphi_\beta(x)}e^{-iK_-\tilde\varphi_\beta(y)}\,{}^*_* \tag{B.46}$$

where the cutoff a was dropped inside the second parenthesis since the distance $x-y$ is kept finite in this point-splitting scheme. The normal ordering is with respect to the

interacting bosonic fields. Since the two pairs of operators commute one obtains

$$
\begin{aligned}
(*) = & \frac{1}{2\pi a}\left(\frac{L}{2\pi a}\right)^{-K_+^2-K_-^2} \sum_\beta \beta\partial_x \Bigg[{}^*_* e^{iK_+\tilde{\varphi}_\beta(x)} e^{-iK_-\tilde{\varphi}_\beta(y)} e^{iK_-\tilde{\varphi}_{\bar{\beta}}(x)} e^{-iK_+\tilde{\varphi}_{\bar{\beta}}(y)} {}^*_* \\
& \left(\frac{2\pi i\beta(y-x)}{L}\right)^{-K_+K_-} \left(\frac{-2\pi i\beta(y-x)}{L}\right)^{-K_+K_-} - (x \leftrightarrow y) \Bigg] \\
= & \frac{1}{2\pi a}\left(\frac{L}{2\pi a}\right)^{-K_+^2-K_-^2} \sum_\beta \beta\partial_x \Bigg[{}^*_* e^{iK_+\tilde{\varphi}_\beta(x)} e^{-iK_-\tilde{\varphi}_\beta(y)} e^{iK_-\tilde{\varphi}_{\bar{\beta}}(x)} e^{-iK_+\tilde{\varphi}_{\bar{\beta}}(y)} {}^*_* \\
& \left[\left(\frac{2\pi(y-x)}{L}\right)^2\right]^{-K_+K_-} - (x \leftrightarrow y) \Bigg]
\end{aligned}
\tag{B.47}
$$

Using $K_+^2 + K_-^2 = 1/(2K) + K/2$ and $K_+K_- = 1/(4K) - K/4$ yields

$$
\begin{aligned}
(*) = & \frac{1}{2\pi a}\left(\frac{L}{2\pi a}\right)^{-1/(2K)-K/2} \left(\frac{2\pi a}{L}\right)^{-1/(2K)+K/2} \sum_\beta \beta\partial_x \\
& \left[{}^*_* e^{iK_+\tilde{\varphi}_\beta(x)} e^{-iK_-\tilde{\varphi}_\beta(y)} e^{iK_-\tilde{\varphi}_{\bar{\beta}}(x)} e^{-iK_+\tilde{\varphi}_{\bar{\beta}}(y)} {}^*_* \left[\frac{(y-x)^2}{a^2}\right]^{-K_+K_-} - (x \leftrightarrow y) \right] \\
= & \frac{1}{2\pi a}\left(\frac{2\pi a}{L}\right)^{K} \sum_\beta \beta\partial_x \left[\left[\frac{(y-x)^2}{a^2}\right]^{-K_+K_-} {}^*_* e^{i[\varphi_\beta(x)-\varphi_{\bar{\beta}}(y)]} - e^{i[\varphi_\beta(y)-\varphi_{\bar{\beta}}(x)]} {}^*_* \right] \\
= & \frac{1}{\pi a}\left(\frac{2\pi a}{L}\right)^{K} \sum_\beta \beta\partial_x \left[\left[\frac{(y-x)^2}{a^2}\right]^{-K_+K_-} {}^*_* \cos[\varphi_\beta(x)-\varphi_{\bar{\beta}}(y)] {}^*_* \right]
\end{aligned}
\tag{B.48}
$$

For the final step, the relabeling $\beta \to \bar{\beta}$ was done in the last term of the previous line. Next, the derivative leads to two terms,

$$
\begin{aligned}
(*) = & \frac{1}{\pi a}\left(\frac{2\pi a}{L}\right)^{K} \sum_\beta \beta \Bigg[\left[\frac{(y-x)^2}{a^2}\right]^{-K_+K_--1} \frac{-2(y-x)}{a^2} {}^*_* \cos[\varphi_\beta(x)-\varphi_{\bar{\beta}}(y)] {}^*_* \\
& - \left[\frac{(y-x)^2}{a^2}\right]^{-K_+K_-} {}^*_* [\partial_x\varphi_\beta(x)] \sin[\varphi_\beta(x)-\varphi_{\bar{\beta}}(y)] {}^*_* \Bigg]
\end{aligned}
\tag{B.49}
$$

Next, using $y = x + a$ yields

$$
(*) = -\frac{1}{\pi a}\left(\frac{2\pi a}{L}\right)^{K} \sum_\beta {}^*_* \frac{2\beta}{a} \cos[\varphi_\beta(x)-\varphi_{\bar{\beta}}(x+a)] + \beta[\partial_x\varphi_\beta(x)] \sin[\varphi_\beta(x)-\varphi_{\bar{\beta}}(x+a)] {}^*_*
\tag{B.50}
$$

In the normal-ordered terms, one can take the limit $a \to 0$ but should keep the first order term in the expansion of the cosine,

$$\begin{aligned}(*) =& \frac{1}{\pi a}\left(\frac{2\pi a}{L}\right)^K \sum_\beta \beta \Bigg\{ -\frac{2}{a}\left[{}^*_* \cos[\varphi_\beta(x) - \varphi_{\bar\beta}(x)] + a[\partial_x \varphi_{\bar\beta}(x)] \sin[\varphi_\beta(x) - \varphi_{\bar\beta}(x)] {}^*_*\right] \\ & - {}^*_* [\partial_x \varphi_\beta(x)] \sin[\varphi_\beta(x) - \varphi_{\bar\beta}(x)] {}^*_* \Bigg\} \\ =& \frac{1}{\pi a}\left(\frac{2\pi a}{L}\right)^K \sum_\beta \beta \Bigg\{ -\frac{2}{a}\left[{}^*_* \cos[2\beta\phi(x)] + a[\partial_x \varphi_{\bar\beta}(x)] \sin[2\beta\phi(x)] {}^*_*\right] \\ & - {}^*_* [\partial_x \varphi_\beta(x)] \sin[2\beta\phi(x)] {}^*_* \Bigg\} \end{aligned} \tag{B.51}$$

The cosine term vanishes in the summation over β, but the sine terms survive,

$$\begin{aligned}(*) &= \frac{1}{\pi a}\left(\frac{2\pi a}{L}\right)^K \left\{ -2 \sum_\beta {}^*_* [\partial_x \varphi_{\bar\beta}(x)] \sin[2\phi(x)] {}^*_* - \sum_\beta {}^*_* [\partial_x \varphi_\beta(x)] \sin[2\phi(x)] {}^*_* \right\} \\ &= -\frac{3}{\pi a}\left(\frac{2\pi a}{L}\right)^K \sum_\beta {}^*_* [\partial_x \varphi_{\bar\beta}(x)] \sin[2\phi(x)] {}^*_* \\ &= \frac{6}{\pi a}\left(\frac{2\pi a}{L}\right)^K {}^*_* [\partial_x \theta(x)] \sin[2\phi(x)] {}^*_* . \end{aligned} \tag{B.52}$$

This completes the bosonization of the first part of the product. The density-term can be bosonized straightforwardly,

$$\sum_\alpha \partial_x \rho_\alpha(x) = -\frac{1}{\pi}\partial_x^2 \phi(x) \tag{B.53}$$

Therefore, the bosonized single-particle backscattering Hamiltonian reads

$$\begin{aligned} H_{int}^{spb} &= \frac{2U_0}{k_0^2}\left(-\frac{1}{\pi}\right)\left[\frac{6}{\pi a}\left(\frac{2\pi a}{L}\right)^K\right] \int dx [\partial_x^2 \phi(x)] {}^*_* [\partial_x \theta(x)] \sin[2\phi(x)] {}^*_* \\ &= -\frac{12U_0}{\pi^2 k_0^2 a}\left(\frac{2\pi a}{L}\right)^K \int dx [\partial_x^2 \phi(x)] {}^*_* [\partial_x \theta(x)] \sin[2\phi(x)] {}^*_* \end{aligned} \tag{B.54}$$

As expected, the cutoff dependence drops out for $K = 1$. Now, one has to find a dimensionless coupling constant as the basis for RG. Since $U_0/(k_0^2 a)$ has units energy times length squared (U_0 has energy times length), the choice is pretty much unique. Defining

$$\lambda = \frac{12U_0}{\pi^2 v_F k_0^2 a^2} \tag{B.55}$$

yields

$$H_{int}^{spb} = -\lambda v_F a \left(\frac{2\pi a}{L}\right)^K \int dx [\partial_x^2 \phi(x)] {}^*_* [\partial_x \theta(x)] \sin[2\phi(x)] {}^*_* \tag{B.56}$$

However, this operator is not normal-ordered yet. Since it should be normal ordered with respect to the bosonic fields of the interacting system, it makes sense to first rewrite it as

$$\begin{aligned}
H_{int}^{spb} =& -\lambda v_F a \left(\frac{2\pi a}{L}\right)^K \int dx [\partial_x^2 \tilde{\phi}(x)]_*^* [\partial_x \tilde{\theta}(x)] \sin[2\sqrt{K}\tilde{\phi}(x)]_*^* \\
=& -\frac{\lambda v_F a}{2i} \left(\frac{2\pi a}{L}\right)^K \int dx \sum_{\alpha=\pm} \alpha [\partial_x^2 \tilde{\phi}(x)]_*^* [\partial_x \tilde{\theta}(x)] e^{2i\alpha\sqrt{K}\tilde{\phi}(x)}{}_*^* \\
=& -\frac{\lambda v_F a}{2i} \left(\frac{2\pi a}{L}\right)^K \int dx \sum_{\alpha=\pm} \alpha \partial_x^2 (\tilde{\phi}^+ + \tilde{\phi}^-) \Big[\partial_x \tilde{\theta}^+ e^{2i\alpha\sqrt{K}\tilde{\phi}^+(x)} e^{2i\alpha\sqrt{K}\tilde{\phi}^-(x)} \\
&+ e^{2i\alpha\sqrt{K}\tilde{\phi}^+(x)} e^{2i\alpha\sqrt{K}\tilde{\phi}^-(x)} \partial_x \tilde{\theta}^- \Big]
\end{aligned} \tag{B.57}$$

with the creator and annihilator parts $\tilde{\theta}^\pm$ and $\tilde{\phi}^\pm$ and an explicit writing out of the normal ordering. The term containing $\partial_x^2 \tilde{\phi}^+$ is already normal ordered, but in the other term one still has to commute $\partial_x^2 \tilde{\phi}^-$ past $\tilde{\theta}^+$ and $\tilde{\phi}^+$. In terms of bosonic modes, [Giamarchi03]

$$\tilde{\phi}^+(x) = -\frac{i\pi}{L} \sum_p \sqrt{\frac{L|p|}{2\pi}} \frac{1}{p} e^{-a|p|/2} e^{-ipx} b_p^\dagger \tag{B.58}$$

$$\tilde{\phi}^-(x) = -\frac{i\pi}{L} \sum_p \sqrt{\frac{L|p|}{2\pi}} \frac{1}{p} e^{-a|p|/2} e^{-ipx} b_{-p} \tag{B.59}$$

$$\tilde{\theta}^+(x) = \frac{i\pi}{L} \sum_p \sqrt{\frac{L|p|}{2\pi}} \frac{1}{|p|} e^{-a|p|/2} e^{-ipx} b_p^\dagger \tag{B.60}$$

$$\tilde{\theta}^-(x) = -\frac{i\pi}{L} \sum_p \sqrt{\frac{L|p|}{2\pi}} \frac{1}{|p|} e^{-a|p|/2} e^{-ipx} b_{-p}. \tag{B.61}$$

Some commutators become inevitable,

$$\begin{aligned}
[\tilde{\phi}^-(x), \tilde{\phi}^+(y)] &= -\frac{\pi^2}{L^2} \frac{L}{2\pi} \sum_p |p| \frac{1}{-p^2} e^{-a|p|} e^{-ip(x-y)} = \frac{\pi}{2L} \sum_p \frac{1}{|p|} e^{-a|p|} e^{-ip(x-y)} \\
&= \frac{1}{4} \sum_n \frac{1}{|n|} e^{-2\pi a|n|/L} e^{-2\pi i n(x-y)/L} \\
&= \frac{1}{4} \sum_{n>0} \frac{1}{n} e^{-2\pi(a+i(x-y))n/L} + \frac{1}{4} \sum_{n>0} \frac{1}{n} e^{-2\pi(a-i(x-y))n/L} \\
&= -\frac{1}{4} \ln\left[1 - e^{-2\pi(a+i(x-y))/L}\right] - \frac{1}{4} \ln\left[1 - e^{-2\pi(a-i(x-y))/L}\right] \\
[\tilde{\phi}^-(x), \tilde{\theta}^+(y)] &= \frac{\pi^2}{L^2} \frac{L}{2\pi} \sum_p |p| \frac{1}{p|p|} e^{-a|p|} e^{-ip(x-y)} = \frac{\pi}{2L} \sum_p \frac{1}{p} e^{-a|p|} e^{-ip(x-y)} \\
&= \frac{1}{4} \sum_{n>0} \frac{1}{n} e^{-2\pi(a+i(x-y))n/L} - \frac{1}{4} \sum_{n>0} \frac{1}{n} e^{-2\pi(a-i(x-y))n/L} \\
&= -\frac{1}{4} \ln\left[1 - e^{-2\pi(a+i(x-y))/L}\right] + \frac{1}{4} \ln\left[1 - e^{-2\pi(a-i(x-y))/L}\right].
\end{aligned} \tag{B.62}$$

Taking the limit $L \to \infty$ at fixed a, x, y first, the differentiating twice with respect to x, and finally letting $y \to x$, yields,

$$\begin{aligned}[\partial_x^2 \tilde{\phi}^-(x), \tilde{\phi}^+(x)] &= -\frac{1}{2a^2} \\ [\partial_x^2 \tilde{\phi}^-(x), \tilde{\theta}^+(x)] &= 0. \end{aligned} \tag{B.63}$$

Therefore, using the formula $[A, e^B] = [A, B]e^B$ for $[A, B] \in \mathbb{C}$, one finds

$$\begin{aligned} H_{int}^{spb} =& -\frac{\lambda v_F a}{2i}\left(\frac{2\pi a}{L}\right)^K \int dx \sum_{\alpha=\pm} \alpha \Big\{ \\ & \partial_x^2\tilde{\phi}^+ \left[\partial_x\tilde{\theta}^+ e^{2i\alpha\sqrt{K}\tilde{\phi}^+(x)} e^{2i\alpha\sqrt{K}\tilde{\phi}^-(x)} + e^{2i\alpha\sqrt{K}\tilde{\phi}^+(x)} e^{2i\alpha\sqrt{K}\tilde{\phi}^-(x)} \partial_x\tilde{\theta}^-\right] \\ & + \left[\partial_x\tilde{\theta}^+ \partial_x^2\tilde{\phi}^- e^{2i\alpha\sqrt{K}\tilde{\phi}^+(x)} e^{2i\alpha\sqrt{K}\tilde{\phi}^-(x)} + \partial_x^2\tilde{\phi}^- e^{2i\alpha\sqrt{K}\tilde{\phi}^+(x)} e^{2i\alpha\sqrt{K}\tilde{\phi}^-(x)} \partial_x\tilde{\theta}^-\right] \Big\} \\ =& -\frac{\lambda v_F a}{2i}\left(\frac{2\pi a}{L}\right)^K \int dx \sum_{\alpha=\pm} \alpha \Big\{ \\ & \partial_x^2\tilde{\phi}^+ \left[\partial_x\tilde{\theta}^+ e^{2i\alpha\sqrt{K}\tilde{\phi}^+(x)} e^{2i\alpha\sqrt{K}\tilde{\phi}^-(x)} + e^{2i\alpha\sqrt{K}\tilde{\phi}^+(x)} e^{2i\alpha\sqrt{K}\tilde{\phi}^-(x)} \partial_x\tilde{\theta}^-\right] \\ & + \partial_x\tilde{\theta}^+ e^{2i\alpha\sqrt{K}\tilde{\phi}^+(x)} \left(\partial_x^2\tilde{\phi}^- - \frac{i\alpha\sqrt{K}}{a^2}\right) e^{2i\alpha\sqrt{K}\tilde{\phi}^-(x)} \\ & + e^{2i\alpha\sqrt{K}\tilde{\phi}^+(x)} \left(\partial_x^2\tilde{\phi}^- - \frac{i\alpha\sqrt{K}}{a^2}\right) e^{2i\alpha\sqrt{K}\tilde{\phi}^-(x)} \partial_x\tilde{\theta}^- \Big\} \end{aligned} \tag{B.64}$$

Finally, one obtains the expected normal-ordered term plus two additional terms which arise from the commutators,

$$\begin{aligned} H_{int}^{spb} =& -\lambda v_F a \left(\frac{2\pi a}{L}\right)^K \int dx \, {}^*_*(\partial_x^2\tilde{\phi})(\partial_x\tilde{\theta}) \sin[2\sqrt{K}\tilde{\phi}(x)]{}^*_* \\ & + \frac{\lambda v_F \sqrt{K}}{a}\left(\frac{2\pi a}{L}\right)^K \int dx \, {}^*_*(\partial_x\tilde{\theta}) \cos[2\sqrt{K}\tilde{\phi}(x)]{}^*_* \\ =& -\lambda v_F a \left(\frac{2\pi a}{L}\right)^K \int dx \, {}^*_*(\partial_x^2\phi)(\partial_x\theta) \sin[2\phi(x)]{}^*_* \\ & + \frac{\lambda v_F K}{a}\left(\frac{2\pi a}{L}\right)^K \int dx \, {}^*_*(\partial_x\theta) \cos[2\phi(x)]{}^*_* . \end{aligned} \tag{B.65}$$

The first term was expected. In the second term, it is a bit surprising to recover the old friend, the linear Rashba Hamiltonian again. It is also slightly disturbing because that terms appears to have a stronger scaling dimension than the fermionic Hamiltonian (3.27) that was started out with. Then again, one starts out from a non-normal-ordered fermionic Hamiltonian (3.27), and if this was normal-ordered then one would also encounter a non-vanishing commutator which would then produce a Rashba-like term. The correct way would be to start from a normal-ordered fermionic Hamiltonian. When using bosonization, this will give the same result apart from the spurious Rashba term. Therefore, one should simply use,

$$H_{int}^{spb} = -\lambda v_F a \left(\frac{2\pi a}{L}\right)^K \int dx \, {}^*_*(\partial_x^2\phi)(\partial_x\theta) \sin[2\phi(x)]{}^*_* \tag{B.66}$$

as the bosonized single-particle backscattering term.

B.4 Derivation of the RG operator product expansion

The goal of this appendix is to derive an operator product expansion for two single-particle backscattering terms. The first step is to derive some commutators that will become necessary later on. One can split the bosonic fields into a creator and annihilator part as follows

$$\begin{aligned}\phi(x_1,t_1) &= \sqrt{K}\tilde{\phi}(x_1,t_1)\\ &= \frac{\sqrt{K}}{2}\left(\tilde{\varphi}_R(x_1,t_1)-\tilde{\varphi}_L(x_1,t_1)\right)\\ &= \frac{\sqrt{K}}{2}\left(\tilde{\varphi}_R(x_1-vt_1)-\tilde{\varphi}_L(x_1+vt_1)\right)\\ &= \frac{\sqrt{K}}{2}\left(\tilde{\varphi}_R^+(x_1-vt_1)-\tilde{\varphi}_L^+(x_1+vt_1)+\tilde{\varphi}_R^-(x_1-vt_1)-\tilde{\varphi}_L^-(x_1+vt_1)\right) \quad \text{(B.67)}\\ \theta(x_1,t_1) &= \frac{1}{2\sqrt{K}}\left(-\tilde{\varphi}_R^+(x_1-vt_1)-\tilde{\varphi}_L^+(x_1+vt_1)-\tilde{\varphi}_R^-(x_1-vt_1)-\tilde{\varphi}_L^-(x_1+vt_1)\right). \quad \text{(B.68)}\end{aligned}$$

The commutator of these fields can not be fully determined by the commutator of ϕ,θ. So it can be chosen in such a way that $\left[\phi(x),\theta(y)\right]=-i\pi\Theta(x-y)$ holds. A first try is

$$\left[\tilde{\varphi}_\alpha^+(x),\tilde{\varphi}_{\alpha'}^-(y)\right]=\delta_{\alpha\alpha'}\log\left[1-e^{-(a+i\alpha(x-y))\frac{2\pi}{L}}\right]. \quad \text{(B.69)}$$

From this one can back-check

$$\begin{aligned}\left[\tilde{\phi}(x),\tilde{\theta}(y)\right] &= \frac{1}{2}\left[\log\left(1-e^{-(a-i(x-y))\frac{2\pi}{L}}\right)-\log\left(1-e^{-(a+i(x-y))\frac{2\pi}{L}}\right)\right]\\ &= -\frac{i\pi}{2}\mathrm{sign}(x-y). \quad \text{(B.70)}\end{aligned}$$

This is indeed the right commutator, but not in the convention used before. To get the $\Theta(x-y)$ function one would have to use a more complicated commutator as a starting point for the $\tilde{\varphi}^\pm$ fields, but this would make the following calculation longer, so it is better to stick to the sign commutator convention for this part. Next, some useful abbreviations

$$A_i^+ = \partial_x\frac{-\tilde{\varphi}_R^+(x_i^-)-\tilde{\varphi}_L^+(x_i^+)}{2} \quad \text{(B.71)}$$

$$A_i^- = \partial_x\frac{-\tilde{\varphi}_R^-(x_i^-)-\tilde{\varphi}_L^-(x_i^+)}{2} \quad \text{(B.72)}$$

$$C_i^+ = \frac{\tilde{\varphi}_R^+(x_i^-)-\tilde{\varphi}_L^+(x_i^+)}{2} \quad \text{(B.73)}$$

$$C_i^- = \frac{\tilde{\varphi}_R^-(x_i^-)-\tilde{\varphi}_L^-(x_i^+)}{2} \quad \text{(B.74)}$$

$$x_i^\pm = x_i \pm vt_i, \quad \text{(B.75)}$$

are defined. The following step is needed for the second order RG equations. It is necessary to normal order a product of two single particle backscattering terms

$$
\begin{aligned}
&{}^{*}_{*}(\partial^2_{x_1}\phi)(\partial_{x_1}\theta)\sin[2\phi(x_1,t_1)]^{*}_{*}\,{}^{*}_{*}(\partial^2_{x_2}\phi)(\partial_{x_2}\theta)\sin[2\phi(x_2,t_2)]^{*}_{*}\\
=&-\sum_{\alpha,\beta=\pm}\frac{1}{4}{}^{*}_{*}(\partial^2_{x_1}\phi)(\partial_{x_1}\theta)e^{i\alpha 2\phi(x_1,t_1)}{}^{*}_{*}\,{}^{*}_{*}(\partial^2_{x_2}\phi)(\partial_{x_2}\theta)e^{i\beta 2\phi(x_2,t_2)}{}^{*}_{*}\\
\approx&-\sum_{\alpha,\beta=\pm}\frac{1}{4}e^{i\alpha 2\sqrt{K}C_1^+}e^{i\alpha 2\sqrt{K}C_1^-}(\partial^2_{x_1}C_1^-)A_1^-(\partial^2_{x_2}C_2^+)A_2^+e^{i\beta 2\sqrt{K}C_2^+}e^{i\beta 2\sqrt{K}C_2^-}\,.
\end{aligned}
\tag{B.76}
$$

The last transformation did already something quite complex. All terms that can be identified right now that would lead to a final expression in the end containing derivatives were neglected. This can be done because these are less divergent. One can identify these terms because they contain a derivative term which is already in the right normal ordered position. This expression needs to be normal ordered now. The first and the last exponential are already in the right place, so one takes the operators in between only and rearranges them as follows, using the relation $ae^b = e^b(a + [a, b])$ which holds if the commutator is a number

$$
\begin{aligned}
&e^{i\alpha 2\sqrt{K}C_1^-}(\partial^2_{x_1}C_1^-)A_1^-(\partial^2_{x_2}C_2^+)A_2^+e^{i\beta 2\sqrt{K}C_2^+}\\
=&e^{i\alpha 2\sqrt{K}C_1^-}(\partial^2_{x_1}C_1^-)e^{i\beta 2\sqrt{K}C_2^+}\left(A_1^- + \left[A_1^-, i\beta 2\sqrt{K}C_2^+\right]\right)(\partial^2_{x_2}C_2^+)A_2^+\\
=&e^{i\alpha 2\sqrt{K}C_1^-}e^{i\beta 2\sqrt{K}C_2^+}\left((\partial^2_{x_1}C_1^-) + \left[(\partial^2_{x_1}C_1^-), i\beta 2\sqrt{K}C_2^+\right]\right)\\
&\times\left(A_1^- + \left[A_1^-, i\beta 2\sqrt{K}C_2^+\right]\right)(\partial^2_{x_2}C_2^+)A_2^+\\
=&e^{\left[i\alpha 2\sqrt{K}C_1^-, i\beta 2\sqrt{K}C_2^+\right]}e^{i\beta 2\sqrt{K}C_2^+}\left((\partial^2_{x_1}C_1^-) + \left[\partial^2_{x_1}C_1^-, i\beta 2\sqrt{K}C_2^+\right]\right)\\
&\times\left(A_1^- + \left[A_1^-, i\beta 2\sqrt{K}C_2^+\right]\right)\left(\partial^2_{x_2}C_2^+ + \left[i\alpha 2\sqrt{K}C_1^-, \partial^2_{x_2}C_2^+\right]\right)\\
&\times\left(A_2^+ + \left[i\alpha 2\sqrt{K}C_1^-, A_2^+\right]\right)e^{i\alpha 2\sqrt{K}C_1^-}\,.
\end{aligned}
\tag{B.77}
$$

The exponentials are now normal ordered. We again proceed by taking the expression in parenthesis only and normal order it

$$
\begin{aligned}
&\left(\partial_{x_1}^2 C_1^- + i\beta 2\sqrt{K}\left[\partial_{x_1}^2 C_1^-, C_2^+\right]\right)\left(A_1^- + i\beta 2\sqrt{K}\left[A_1^-, C_2^+\right]\right)\\
&\times\left(\partial_{x_2}^2 C_2^+ + i\alpha 2\sqrt{K}\left[C_1^-, \partial_{x_2}^2 C_2^+\right]\right)\left(A_2^+ + i\alpha 2\sqrt{K}\left[C_1^-, A_2^+\right]\right)\\
\approx& 16K^2\left[\partial_{x_1}^2 C_1^-, C_2^+\right]\left[A_1^-, C_2^+\right]\left[C_1^-, \partial_{x_2}^2 C_2^+\right]\left[C_1^-, A_2^+\right] + \left[\left(\partial_{x_1}^2 C_1^-\right)A_1^-, \left(\partial_{x_2}^2 C_2^+\right)A_2^+\right]\\
&- 4\alpha\beta K\Big\{\left[A_1^-, C_2^+\right]\left[\partial_{x_1}^2 C_1^-, \partial_{x_2}^2 C_2^+\right]\left[C_1^-, A_2^+\right] + \left[A_1^-, C_2^+\right]\left[C_1^-, \partial_{x_2}^2 C_2^+\right]\left[\partial_{x_1}^2 C_1^-, A_2^+\right]\\
&+ \left[A_1^-, \partial_{x_2}^2 C_2^+\right]\left[C_1^-, A_2^+\right]\left[\partial_{x_1}^2 C_1^-, C_2^+\right] + \left[\partial_{x_1}^2 C_1^-, C_2^+\right]\left[C_1^-, \partial_{x_2}^2 C_2^+\right]\left[A_1^-, A_2^+\right]\Big\}\\
\approx& 16K^2\left[\partial_{x_1}^2 C_1^-, C_2^+\right]\left[A_1^-, C_2^+\right]\left[C_1^-, \partial_{x_2}^2 C_2^+\right]\left[C_1^-, A_2^+\right] + \left[\partial_{x_1}^2 C_1^-, \partial_{x_2}^2 C_2^+\right]\left[A_1^-, A_2^+\right]\\
&- 4\alpha\beta K\Big\{\left[A_1^-, C_2^+\right]\left[\partial_{x_1}^2 C_1^-, \partial_{x_2}^2 C_2^+\right]\left[C_1^-, A_2^+\right] + \left[A_1^-, C_2^+\right]\left[C_1^-, \partial_{x_2}^2 C_2^+\right]\left[\partial_{x_1}^2 C_1^-, A_2^+\right]\\
&+ \left[A_1^-, \partial_{x_2}^2 C_2^+\right]\left[C_1^-, A_2^+\right]\left[\partial_{x_1}^2 C_1^-, C_2^+\right] + \left[\partial_{x_1}^2 C_1^-, C_2^+\right]\left[C_1^-, \partial_{x_2}^2 C_2^+\right]\left[A_1^-, A_2^+\right]\Big\}\\
&+ \left[\partial_{x_1}^2 C_1^-, A_2^+\right]\left[A_1^-, \partial_{x_2}^2 C_2^+\right]
\end{aligned}
\tag{B.78}
$$

The whole expression contains the following commutators only

$$
\begin{aligned}
\left[C_1^-, C_2^+\right] &= \frac{1}{4}\left[\tilde{\varphi}_R^-(x_1^-), \tilde{\varphi}_R^+(x_2^-)\right] + \frac{1}{4}\left[\tilde{\varphi}_L^-(x_1^+), \tilde{\varphi}_L^+(x_2^+)\right] = g_{++}\\
\left[A_1^-, A_2^+\right] &= \frac{1}{4}\partial_{x_1}\partial_{x_2}\left(\left[-\tilde{\varphi}_R^-(x_1^-), -\tilde{\varphi}_R^+(x_2^-)\right] + \left[-\tilde{\varphi}_L^-(x_1^+), -\tilde{\varphi}_L^+(x_2^+)\right]\right) = \partial_{x_1}\partial_{x_2} g_{++}\\
\left[C_1^-, A_2^+\right] &= -\frac{1}{4}\partial_{x_2}\left[\tilde{\varphi}_R^-(x_1^-), \tilde{\varphi}_R^+(x_2^-)\right] + \frac{1}{4}\partial_{x_2}\left[\tilde{\varphi}_L^-(x_1^+), \tilde{\varphi}_L^+(x_2^+)\right] = \partial_{x_2} g_{-+}\\
\left[A_1^-, C_2^+\right] &= \partial_{x_1} g_{-+}
\end{aligned}
\tag{B.79}
$$

with the properties $\partial_{x_2} = -\partial_{x_1}$, so it can be written as

$$
\begin{aligned}
&- 16K^2\left(\partial_{x_1}^2 g_{++}\right)^2\left(\partial_{x_1} g_{-+}\right)^2 + 4\alpha\beta K\left(\partial_{x_1}^2 g_{++}\right)^3 + 4\alpha\beta K\left(\partial_{x_1} g_{-+}\right)^2\left(\partial_{x_1}^4 g_{++}\right)\\
&+ 8\alpha\beta K\left(\partial_{x_1} g_{-+}\right)\left(\partial_{x_1}^2 g_{++}\right)\left(\partial_{x_1}^3 g_{-+}\right) - \left(\partial_{x_1}^4 g_{++}\right)\left(\partial_{x_1}^2 g_{++}\right) - \left(\partial_{x_1}^3 g_{-+}\right)^2,
\end{aligned}
\tag{B.80}
$$

while

$$
g_{\alpha\beta} = -\frac{\alpha}{4}\log\left[1 - e^{-(a+i(x_2 - vt_2 - x_1 + vt_1))\frac{2\pi}{L}}\right] - \frac{\beta}{4}\log\left[1 - e^{-(a-i(x_2 + vt_2 - x_1 - vt_1))\frac{2\pi}{L}}\right].
\tag{B.81}
$$

What remains is to calculate the prefactor with the exponentiated commutator as

$$\begin{aligned} e^{\left[i\alpha 2\sqrt{K}C_1^-, i\beta 2\sqrt{K}C_2^+\right]} &= e^{-4\alpha\beta K g_{++}} \\ &= e^{-\alpha\beta K\left[\tilde{\varphi}_R^-(x_1^-),\tilde{\varphi}_R^+(x_2^-)\right]-\alpha\beta K\left[\tilde{\varphi}_L^-(x_1^+),\tilde{\varphi}_L^+(x_2^+)\right]} \\ &= \left(1-e^{-(a+i(x_2^- - x_1^-))\frac{2\pi}{L}}\right)^{\alpha\beta K}\left(1-e^{-(a-i(x_2^+ - x_1^+))\frac{2\pi}{L}}\right)^{\alpha\beta K} \\ &\approx \left(a+i(x_2^- - x_1^-)\right)^{\alpha\beta K}\left(a-i(x_2^+ - x_1^+)\right)^{\alpha\beta K}\left(\frac{2\pi}{L}\right)^{2\alpha\beta K} \end{aligned} \tag{B.82}$$

All of this finally leads to the result

$$\begin{aligned} &{}^*_*(\partial_{x_1}^2\phi)(\partial_{x_1}\theta)\sin[2\phi(x_1,t_1)]^*_*\,{}^*_*(\partial_{x_2}^2\phi)(\partial_{x_2}\theta)\sin[2\phi(x_2,t_2)]^*_* \\ \approx &-\sum_{\alpha,\beta=\pm}\frac{1}{4}\left(a+i(x_2^- - x_1^-)\right)^{\alpha\beta K}\left(a-i(x_2^+ - x_1^+)\right)^{\alpha\beta K}\left(\frac{2\pi}{L}\right)^{2\alpha\beta K} \\ &\Big[-16K^2\left(\partial_{x_1}^2 g_{++}\right)^2\left(\partial_{x_1}g_{-+}\right)^2+4\alpha\beta K\left(\partial_{x_1}^2 g_{++}\right)^3+4\alpha\beta K\left(\partial_{x_1}g_{-+}\right)^2\left(\partial_{x_1}^4 g_{++}\right) \\ &+8\alpha\beta K\left(\partial_{x_1}g_{-+}\right)\left(\partial_{x_1}^2 g_{++}\right)\left(\partial_{x_1}^3 g_{-+}\right)-\left(\partial_{x_1}^4 g_{++}\right)\left(\partial_{x_1}^2 g_{++}\right)-\left(\partial_{x_1}^3 g_{-+}\right)^2\Big] \\ &\times\,{}^*_*e^{i\alpha 2\phi(x_1,t_1)+i\beta 2\phi(x_2,t_2)}{}^*_*, \end{aligned} \tag{B.83}$$

here, for $x_1 = x_2$ and $t_1 = t_2$ the operator expression vanishes for $\alpha = -\beta$, therefore one has $\alpha = \beta$.

B.5 Commutation relations of bound state operators

In this appendix, important commutators for the bound state operators are derived. Basically all commutators can be derived from $[\phi(x),\theta(y)] = -i\pi\Theta(x-y)$. It starts with

$$\begin{aligned} \left[S_i, Q_j\right] &= \frac{1}{\pi^2}\left[\theta_{i+1}-\theta_i, \phi_{j+1}-\phi_j\right] = -\frac{1}{\pi^2}\left[\phi_{j+1}-\phi_j, \theta_{i+1}-\theta_i\right] \\ &= \frac{i}{\pi}\left[\Theta(j-i)-\Theta(j+1-i)-\Theta(j-i-1)+\Theta(j-i)\right] \\ &= \frac{i}{\pi}\left(\delta_{ij}-\delta_{i,j+1}\right), \end{aligned} \tag{B.84}$$

with $i,j \in \{1,\ldots,N-1\}$. Especially, the commutator is just a number. From now on, for this section, $i,j = 1,\ldots,N-1$ is always implied. Using this, one can show that

$$e^{i\pi S_i}e^{i\pi Q_j} = e^{i\pi Q_j}e^{i\pi S_i}e^{\left[i\pi S_i, i\pi Q_j\right]} = e^{i\pi Q_j}e^{i\pi S_i}e^{-i\pi(\delta_{ij}-\delta_{i,j+1})}. \tag{B.85}$$

In particular, the following results hold

$$\begin{aligned} e^{i\pi S_j/2}e^{i\pi Q_j} &= e^{-i\pi/2}e^{i\pi Q_j}e^{i\pi S_j/2} \\ e^{i\pi S_{j+1}/2}e^{i\pi Q_j} &= e^{i\pi/2}e^{i\pi Q_j}e^{i\pi S_{j+1}/2} \end{aligned} \tag{B.86}$$

and also for the total charge and spin operators

$$[Q_{tot}, S_{tot}] = \left[\phi(L^-),\theta(L^-)\right] - \left[\phi(L^-),\theta(0^+)\right] + \left[\phi(0^+),\theta(0^+)\right] = 0 \tag{B.87}$$

if we define $\Theta(0) = 1/2$ for the continuous Θ-function. In the same way one finds

$$e^{i\pi Q_{tot}} e^{i\pi S_i/2} = e^{i\pi S_i/2} e^{i\pi Q_{tot}} \tag{B.88}$$

for the mixed commutators. It is assumed here that θ_1 is defined somewhere within the open interval $(0^+, \chi_1)$.

Bibliography

[Altland10] A. Altland and B. Simons, *Condensed Matter Field Theory*. 2nd edition, Cambridge University Press, Cambridge (2010).

[Anderson58] P. W. Anderson, *Absence of Diffusion in Certain Random Lattices*. Phys. Rev. **109**, 1492 (1958).

[Anderson80] P. W. Anderson, D. J. Thouless, E. Abrahams, and D. S. Fisher, *New method for a scaling theory of localization*. Phys. Rev. B **22**, 3519 (1980).

[Ando06] T. Ando, *Screening Effect and Impurity Scattering in Monolayer Graphene*. Journal of the Physical Society of Japan **75**, 074716 (2006).

[Aufray10] B. Aufray, A. Kara, S. Vizzini, H. Oughaddou, C. Léandri, B. Ealet, and G. Le Lay, *Graphene-like silicon nanoribbons on Ag(110): A possible formation of silicene*. Applied Physics Letters **96**, 183102 (2010).

[Bardeen57] J. Bardeen, L. N. Cooper, and J. R. Schrieffer, *Microscopic Theory of Superconductivity*. Phys. Rev. **106**, 162 (1957).

[Béri11] B. Béri and N. R. Cooper, $\mathbb{Z}_2$ *Topological Insulators in Ultracold Atomic Gases*. Phys. Rev. Lett. **107**, 145301 (2011).

[Bernevig06] B. A. Bernevig, T. L. Hughes, and S.-C. Zhang, *Quantum Spin Hall Effect and Topological Phase Transition in HgTe Quantum Wells*. Science **314**, 1757 (2006).

[Bernevig13] A. Bernevig and T. Hughes, *Topological Insulators and Topological Superconductors*. Princeton University Press (2013).

[Billy08] J. Billy, V. Josse, Z. Zuo, A. Bernard, B. Hambrecht, P. Lugan, D. Clement, L. Sanchez-Palencia, P. Bouyer, and A. Aspect, *Direct observation of Anderson localization of matter waves in a controlled disorder*. Nature **453**, 891 (2008).

[Bishnoi13] B. Bishnoi and B. Ghosh, *Spin transport in silicene and germanene*. RSC Adv. **3**, 26153 (2013).

[Black-Schaffer11] A. M. Black-Schaffer, *Self-consistent superconducting proximity effect at the quantum spin Hall edge*. Phys. Rev. B **83**, 060504 (2011).

[Braunecker12] B. Braunecker, C. Bena, and P. Simon, *Spectral properties of Luttinger liquids: A comparative analysis of regular, helical, and spiral Luttinger liquids*. Phys. Rev. B **85**, 035136 (2012).

[Bruus04] H. Bruus and K. Flensberg, *Many-Body Quantum Theory in Condensed Matter Physics*. Oxford University Press (2004).

[Cardy96] J. Cardy, *Scaling and Renormalization in Statistical Physics*. Cambridge University Press (1996).

[Cazalilla14] M. A. Cazalilla, H. Ochoa, and F. Guinea, *Quantum Spin Hall Effect in Two-Dimensional Crystals of Transition-Metal Dichalcogenides*. Phys. Rev. Lett. **113**, 077201 (2014).

[Chen12] L. Chen, Q. Liu, X. Lin, X. Zhang, and X. Jiang, *Disorder dependence of helical edge states in HgTe/CdTe quantum wells*. New Journal of Physics **14**, 043028 (2012).

[Chu09] R.-L. Chu, J. Li, J. K. Jain, and S.-Q. Shen, *Coherent oscillations and giant edge magnetoresistance in singly connected topological insulators*. Phys. Rev. B **80**, 081102 (2009).

[Clarke13] D. J. Clarke, J. Alicea, and K. Shtengel, *Exotic non-Abelian anyons from conventional fractional quantum Hall states*. Nat. Comm. **4**, 1348 (2013).

[Couto14] N. J. G. Couto, D. Costanzo, S. Engels, D.-K. Ki, K. Watanabe, T. Taniguchi, C. Stampfer, F. Guinea, and A. F. Morpurgo, *Random Strain Fluctuations as Dominant Disorder Source for High-Quality On-Substrate Graphene Devices*. Phys. Rev. X **4**, 041019 (2014).

[Das Sarma06] S. Das Sarma, M. Freedman, and C. Nayak, *Topological Quantum Computation*. Physics Today **59**, 32 (2006).

[Das12] A. Das, Y. Ronen, Y. Most, Y. Oreg, M. Heiblum, and H. Shtrikman, *Zero-bias peaks and splitting in an Al-InAs nanowire topological superconductor as a signature of Majorana fermions*. Nature Physics **8**, 887 (2012).

[Delplace12] P. Delplace, J. Li, and M. Büttiker, *Magnetic-Field-Induced Localization in 2D Topological Insulators*. Phys. Rev. Lett. **109**, 246803 (2012).

[Deng12] M. T. Deng, C. L. Yu, G. Y. Huang, M. Larsson, P. Caroff, and H. Q. Xu, *Anomalous Zero-Bias Conductance Peak in a Nb–InSb Nanowire–Nb Hybrid Device*. Nano Letters **12**, 6414 (2012).

[Dolcetto12] G. Dolcetto, S. Barbarino, D. Ferraro, N. Magnoli, and M. Sassetti, *Tunneling between helical edge states through extended contacts*. Phys. Rev. B **85**, 195138 (2012).

[Dolcini11] F. Dolcini, *Full electrical control of charge and spin conductance through interferometry of edge states in topological insulators*. Phys. Rev. B **83**, 165304 (2011).

[Du15] L. Du, I. Knez, G. Sullivan, and R.-R. Du, *Robust Helical Edge Transport in Gated* InAs/GaSb *Bilayers*. Phys. Rev. Lett. **114**, 096802 (2015).

[Dávila14] M. E. Dávila, L. Xian, S. Cahangirov, A. Rubio, and G. L. Lay, *Germanene: a novel two-dimensional germanium allotrope akin to graphene and silicene*. New Journal of Physics **16**, 095002 (2014).

[Edge13] J. M. Edge, J. Li, P. Delplace, and M. Büttiker, *Z_2 Peak of Noise Correlations in a Quantum Spin Hall Insulator*. Phys. Rev. Lett. **110**, 246601 (2013).

[Ezawa15] M. Ezawa, *Antiferromagnetic Topological Superconductor and Electrically Controllable Majorana Fermions*. Phys. Rev. Lett. **114**, 056403 (2015).

[Fratini08] S. Fratini and F. Guinea, *Substrate-limited electron dynamics in graphene*. Phys. Rev. B **77**, 195415 (2008).

[Freedman02] M. H. Freedman, M. Larsen, and Z. Wang, *A Modular Functor Which is Universal for Quantum Computation*. Communications in Mathematical Physics **227**, 605 (2002).

[Fu07] L. Fu, C. L. Kane, and E. J. Mele, *Topological Insulators in Three Dimensions*. Phys. Rev. Lett. **98**, 106803 (2007).

[Fu08] L. Fu and C. L. Kane, *Superconducting Proximity Effect and Majorana Fermions at the Surface of a Topological Insulator*. Phys. Rev. Lett. **100**, 096407 (2008).

[Fu09] L. Fu and C. L. Kane, *Josephson current and noise at a superconductor/quantum-spin-Hall-insulator/superconductor junction*. Phys. Rev. B **79**, 161408 (2009).

[Fu14] B. Fu, H. Zheng, Q. Li, Q. Shi, and J. Yang, *Topological phase transition driven by a spatially periodic potential*. Phys. Rev. B **90**, 214502 (2014).

[Gangadharaiah11] S. Gangadharaiah, B. Braunecker, P. Simon, and D. Loss, *Majorana Edge States in Interacting One-Dimensional Systems*. Phys. Rev. Lett. **107**, 036801 (2011).

[Garate13] I. Garate, *Phonon-Induced Topological Transitions and Crossovers in Dirac Materials*. Phys. Rev. Lett. **110**, 046402 (2013).

[Giamarchi03] T. Giamarchi, *Quantum Physics in One Dimension*. Clarendon Press, Oxford (2003).

[Girschik13] A. Girschik, F. Libisch, and S. Rotter, *Topological insulator in the presence of spatially correlated disorder*. Phys. Rev. B **88**, 014201 (2013).

[Girschik15] A. Girschik, F. Libisch, and S. Rotter, *Percolating states in the topological Anderson insulator*. Phys. Rev. B **91**, 214204 (2015).

[Groth09] C. W. Groth, M. Wimmer, A. R. Akhmerov, J. Tworzydło, and C. W. J. Beenakker, *Theory of the Topological Anderson Insulator*. Phys. Rev. Lett. **103**, 196805 (2009).

[Groth14] C. W. Groth, M. Wimmer, A. R. Akhmerov, and X. Waintal, *Kwant: a software package for quantum transport*. New Journal of Physics **16**, 063065 (2014).

[Guo10] H.-M. Guo, G. Rosenberg, G. Refael, and M. Franz, *Topological Anderson Insulator in Three Dimensions*. Phys. Rev. Lett. **105**, 216601 (2010).

[Haldane88] F. D. M. Haldane, *Model for a Quantum Hall Effect without Landau Levels: Condensed-Matter Realization of the "Parity Anomaly"*. Phys. Rev. Lett. **61**, 2015 (1988).

[Hart14] S. Hart, H. Ren, T. Wagner, P. Leubner, M. Muhlbauer, C. Brune, H. Buhmann, L. W. Molenkamp, and A. Yacoby, *Induced superconductivity in the quantum spin Hall edge*. Nat. Phys. **10**, 638 (2014).

[Hasan10] M. Z. Hasan and C. L. Kane, *Colloquium: Topological insulators*. Rev. Mod. Phys. **82**, 3045 (2010).

[Hsieh08] D. Hsieh, D. Qian, L. Wray, Y. Xia, Y. S. Hor, R. J. Cava, and M. Z. Hasan, *A topological Dirac insulator in a quantum spin Hall phase*. Nature **452**, 970 (2008).

[Huang13] C.-W. Huang, S. T. Carr, D. Gutman, E. Shimshoni, and A. D. Mirlin, *Transport via double constrictions in integer and fractional topological insulators*. Phys. Rev. B **88**, 125134 (2013).

[Žutić04] I. Žutić, J. Fabian, and S. Das Sarma, *Spintronics: Fundamentals and applications*. Rev. Mod. Phys. **76**, 323 (2004).

[Imambekov12] A. Imambekov, T. L. Schmidt, and L. I. Glazman, *One-dimensional quantum liquids: Beyond the Luttinger liquid paradigm*. Rev. Mod. Phys. **84**, 1253 (2012).

[Ishigami07] M. Ishigami, J. H. Chen, W. G. Cullen, M. S. Fuhrer, and E. D. Williams, *Atomic Structure of Graphene on SiO2*. Nano Letters **7**, 1643 (2007).

[Ishii03] H. Ishii, H. Kataura, H. Shiozawa, H. Yoshioka, H. Otsubo, Y. Takayama, T. Miyahara, S. Suzuki, Y. Achiba, M. Nakatake, T. Narimura, M. Higashiguchi, K. Shimada, H. Namatame, and M. Taniguchi, *Direct observation of Tomonaga-Luttinger-liquid state in carbon nanotubes at low temperatures*. Nature **426**, 540 (2003).

[Jiang09] H. Jiang, L. Wang, Q.-f. Sun, and X. C. Xie, *Numerical study of the topological Anderson insulator in HgTe/CdTe quantum wells*. Phys. Rev. B **80**, 165316 (2009).

[Jiang12] H. Jiang, Z. Qiao, H. Liu, J. Shi, and Q. Niu, *Stabilizing Topological Phases in Graphene via Random Adsorption*. Phys. Rev. Lett. **109**, 116803 (2012).

[Kainaris14] N. Kainaris, I. V. Gornyi, S. T. Carr, and A. D. Mirlin, *Conductivity of a generic helical liquid*. Phys. Rev. B **90**, 075118 (2014).

[Kane05a] C. L. Kane and E. J. Mele, *Quantum Spin Hall Effect in Graphene*. Phys. Rev. Lett. **95**, 226801 (2005).

[Kane05b] C. L. Kane and E. J. Mele, *Z_2 Topological Order and the Quantum Spin Hall Effect*. Phys. Rev. Lett. **95**, 146802 (2005).

[Kara12] A. Kara, H. Enriquez, A. P. Seitsonen, L. L. Y. Voon, S. Vizzini, B. Aufray, and H. Oughaddou, *A review on silicene — New candidate for electronics*. Surface Science Reports **67**, 1 (2012).

[Kawai15] S. Kawai, S. Saito, S. Osumi, S. Yamaguchi, A. S. Foster, P. Spijker, and E. Meyer, *Atomically controlled substitutional boron-doping of graphene nanoribbons*. Nat Commun **6** (2015).

[Khaymovich11] I. M. Khaymovich, N. M. Chtchelkatchev, and V. M. Vinokur, *Instability of topological order and localization of edge states in HgTe quantum wells coupled to s-wave superconductor*. Phys. Rev. B **84**, 075142 (2011).

[Kitaev01] A. Y. Kitaev, *Unpaired Majorana fermions in quantum wires*. Physics-Uspekhi **44**, 131 (2001).

[Klinovaja14] J. Klinovaja, A. Yacoby, and D. Loss, *Kramers pairs of Majorana fermions and parafermions in fractional topological insulators*. Phys. Rev. B **90**, 155447 (2014).

[Klinovaja15] J. Klinovaja and D. Loss, *Fractional charge and spin states in topological insulator constrictions*. Phys. Rev. B **92**, 121410 (2015).

[Knez11] I. Knez, R.-R. Du, and G. Sullivan, *Evidence for Helical Edge Modes in Inverted InAs/GaSb Quantum Wells*. Phys. Rev. Lett. **107**, 136603 (2011).

[König13] M. König, M. Baenninger, A. G. F. Garcia, N. Harjee, B. L. Pruitt, C. Ames, P. Leubner, C. Brüne, H. Buhmann, L. W. Molenkamp, and D. Goldhaber-Gordon, *Spatially Resolved Study of Backscattering in the Quantum Spin Hall State*. Phys. Rev. X **3**, 021003 (2013).

[König07] M. König, S. Wiedmann, C. Brüne, A. Roth, H. Buhmann, L. W. Molenkamp, X.-L. Qi, and S.-C. Zhang, *Quantum Spin Hall Insulator State in HgTe Quantum Wells*. Science **318**, 766 (2007).

[Lee12] Y.-W. Lee, Y.-L. Lee, and C.-H. Chung, *Nonequilibrium noise correlations in a point contact of helical edge states*. Phys. Rev. B **86**, 235121 (2012).

[Levin09] M. Levin and A. Stern, *Fractional Topological Insulators*. Phys. Rev. Lett. **103**, 196803 (2009).

[Li09] J. Li, R.-L. Chu, J. K. Jain, and S.-Q. Shen, *Topological Anderson Insulator*. Phys. Rev. Lett. **102**, 136806 (2009).

[Lindner12] N. H. Lindner, E. Berg, G. Refael, and A. Stern, *Fractionalizing Majorana Fermions: Non-Abelian Statistics on the Edges of Abelian Quantum Hall States*. Phys. Rev. X **2**, 041002 (2012).

[Liu08] C. Liu, T. L. Hughes, X.-L. Qi, K. Wang, and S.-C. Zhang, *Quantum Spin Hall Effect in Inverted Type-II Semiconductors*. Phys. Rev. Lett. **100**, 236601 (2008).

[Liu11a] C.-C. Liu, W. Feng, and Y. Yao, *Quantum Spin Hall Effect in Silicene and Two-Dimensional Germanium*. Phys. Rev. Lett. **107**, 076802 (2011).

[Liu11b] C.-C. Liu, H. Jiang, and Y. Yao, *Low-energy effective Hamiltonian involving spin-orbit coupling in silicene and two-dimensional germanium and tin*. Phys. Rev. B **84**, 195430 (2011).

[Liu11c] C.-X. Liu, J. C. Budich, P. Recher, and B. Trauzettel, *Charge-spin duality in nonequilibrium transport of helical liquids*. Phys. Rev. B **83**, 035407 (2011).

[Lobos15] A. M. Lobos, A. O. Dobry, and V. Galitski, *Magnetic End States in a Strongly Interacting One-Dimensional Topological Kondo Insulator*. Phys. Rev. X **5**, 021017 (2015).

[Lutchyn10] R. M. Lutchyn, J. D. Sau, and S. Das Sarma, *Majorana Fermions and a Topological Phase Transition in Semiconductor-Superconductor Heterostructures*. Phys. Rev. Lett. **105**, 077001 (2010).

[Lv13] S.-H. Lv, J. Song, and Y.-X. Li, *Topological Anderson insulator induced by intercell hopping disorder*. Journal of Applied Physics **114**, 183710 (2013).

[Maciejko09] J. Maciejko, C. Liu, Y. Oreg, X. Qi, C. Wu, and S. Zhang, *Kondo Effect in the Helical Edge Liquid of the Quantum Spin Hall State*. Phys. Rev. Lett. **102**, 256803 (2009).

[Maslov95] D. L. Maslov and M. Stone, *Landauer conductance of Luttinger liquids with leads*. Phys. Rev. B **52**, R5539 (1995).

[Michetti11] P. Michetti and P. Recher, *Bound states and persistent currents in topological insulator rings*. Phys. Rev. B **83**, 125420 (2011).

[Min06] H. Min, J. E. Hill, N. A. Sinitsyn, B. R. Sahu, L. Kleinman, and A. H. MacDonald, *Intrinsic and Rashba spin-orbit interactions in graphene sheets*. Phys. Rev. B **74**, 165310 (2006).

[Moore07] J. E. Moore and L. Balents, *Topological invariants of time-reversal-invariant band structures*. Phys. Rev. B **75**, 121306 (2007).

[Mourik12] V. Mourik, K. Zuo, S. M. Frolov, S. R. Plissard, E. P. A. M. Bakkers, and L. P. Kouwenhoven, *Signatures of Majorana Fermions in Hybrid Superconductor-Semiconductor Nanowire Devices*. Science **336**, 1003 (2012).

[Nalitov15] A. V. Nalitov, D. D. Solnyshkov, and G. Malpuech, *Polariton $\mathbb{Z}$ Topological Insulator*. Phys. Rev. Lett. **114**, 116401 (2015).

[Nayak08] C. Nayak, S. H. Simon, A. Stern, M. Freedman, and S. Das Sarma, *Non-Abelian anyons and topological quantum computation*. Rev. Mod. Phys. **80**, 1083 (2008).

[Oreg10] Y. Oreg, G. Refael, and F. von Oppen, *Helical Liquids and Majorana Bound States in Quantum Wires*. Phys. Rev. Lett. **105**, 177002 (2010).

[Orth13] C. P. Orth, G. Strübi, and T. L. Schmidt, *Point contacts and localization in generic helical liquids*. Phys. Rev. B **88**, 165315 (2013).

[Orth15a] C. P. Orth, R. P. Tiwari, T. Meng, and T. L. Schmidt, *Non-Abelian parafermions in time-reversal-invariant interacting helical systems*. Phys. Rev. B **91**, 081406 (2015).

[Orth15b] C. P. Orth, T. Sekera, C. Bruder, and T. L. Schmidt, *The topological Anderson insulator phase in the Kane-Mele model*. ArXiv e-prints: 1512.03233 (2015).

[Pachos12] J. Pachos, *Introduction to Topological Quantum Computation*. Cambridge University Press (2012).

[Pendry94] J. Pendry, *Symmetry and transport of waves in one-dimensional disordered systems*. Advances in Physics **43**, 461 (1994).

[Pesin12] D. Pesin and A. H. MacDonald, *Spintronics and pseudospintronics in graphene and topological insulators*. Nat Mater **11**, 409 (2012).

[Peskin95] M. Peskin and D. Schroeder, *An Introduction to Quantum Field Theory*. Westview Press (1995).

[Ponomarenko95] V. Ponomarenko, *Renormalization of the one-dimensional conductance in the Luttinger-liquid model*. Physical Review B **52**, R8666 (1995).

[Pribiag15] V. S. Pribiag, A. J. A. Beukman, F. Qu, M. C. Cassidy, C. Charpentier, W. Wegscheider, and L. P. Kouwenhoven, *Edge-mode superconductivity in a two-dimensional topological insulator*. Nat. Nano. **10**, 593 (2015).

[Prodan11] E. Prodan, *Three-dimensional phase diagram of disordered HgTe/CdTe quantum spin-Hall wells*. Phys. Rev. B **83**, 195119 (2011).

[Qi11] X. Qi and S. Zhang, *Topological insulators and superconductors*. Rev. Mod. Phys. **83**, 1057 (2011).

[Rod15] A. Rod, T. L. Schmidt, and S. Rachel, *Spin texture of generic helical edge states*. Phys. Rev. B **91**, 245112 (2015).

[Romeo12] F. Romeo, R. Citro, D. Ferraro, and M. Sassetti, *Electrical switching and interferometry of massive Dirac particles in topological insulator constrictions*. Phys. Rev. B **86**, 165418 (2012).

[Romeo14] F. Romeo and R. Citro, *Interaction effects in nonequilibrium transport properties of a four-terminal topological corner junction*. Phys. Rev. B **90**, 155408 (2014).

[Roth09] A. Roth, C. Brüne, H. Buhmann, L. W. Molenkamp, J. Maciejko, X.-L. Qi, and S.-C. Zhang, *Nonlocal Transport in the Quantum Spin Hall State*. Science **325**, 294 (2009).

[Rothe10] D. G. Rothe, R. W. Reinthaler, C. Liu, L. W. Molenkamp, S. Zhang, and E. M. Hankiewicz, *Fingerprint of different spin-orbit terms for spin transport in HgTe quantum wells*. New J. Phys. **12**, 065012 (2010).

[Safi95] I. Safi and H. Schulz, *Transport in an inhomogeneous interacting one-dimensional system*. Physical Review B **52**, R17040 (1995).

[Schmidt11] T. L. Schmidt, *Current Correlations in Quantum Spin Hall Insulators*. Phys. Rev. Lett. **107**, 096602 (2011).

[Schmidt12] T. L. Schmidt, S. Rachel, F. von Oppen, and L. I. Glazman, *Inelastic Electron Backscattering in a Generic Helical Edge Channel*. Phys. Rev. Lett. **108**, 156402 (2012).

[Schmidt13] T. L. Schmidt, *Finite-temperature conductance of interacting quantum wires with Rashba spin-orbit coupling*. Phys. Rev. B **88**, 235429 (2013).

[Sela11] E. Sela, A. Altland, and A. Rosch, *Majorana fermions in strongly interacting helical liquids*. Phys. Rev. B **84**, 085114 (2011).

[Skinner12] B. Skinner, T. Chen, and B. I. Shklovskii, *Why Is the Bulk Resistivity of Topological Insulators So Small?* Phys. Rev. Lett. **109**, 176801 (2012).

[Song12] J. Song, H. Liu, H. Jiang, Q.-f. Sun, and X. C. Xie, *Dependence of topological Anderson insulator on the type of disorder*. Phys. Rev. B **85**, 195125 (2012).

[Sternativo14] P. Sternativo and F. Dolcini, *Effects of disorder on electron tunneling through helical edge states*. Phys. Rev. B **90**, 125135 (2014).

[Tanaka11] Y. Tanaka, A. Furusaki, and K. A. Matveev, *Conductance of a Helical Edge Liquid Coupled to a Magnetic Impurity*. Phys. Rev. Lett. **106**, 236402 (2011).

[Teo09] J. C. Y. Teo and C. L. Kane, *Critical behavior of a point contact in a quantum spin Hall insulator*. Phys. Rev. B **79**, 235321 (2009).

[Titum15] P. Titum, N. H. Lindner, M. C. Rechtsman, and G. Refael, *Disorder-Induced Floquet Topological Insulators*. Phys. Rev. Lett. **114**, 056801 (2015).

[Ueda13] S. Ueda, N. Kawakami, and M. Sigrist, *Proximity effects in a topological-insulator/Mott-insulator heterostructure*. Phys. Rev. B **87**, 161108 (2013).

[Varlet15] A. Varlet, M. Mucha-Kruczyński, D. Bischoff, P. Simonet, T. Taniguchi, K. Watanabe, V. Fal'ko, T. Ihn, and K. Ensslin, *Tunable Fermi surface topology and Lifshitz transition in bilayer graphene*. Synthetic Metals **210, Part A**, 19 (2015).

[Väyrynen13] J. I. Väyrynen, M. Goldstein, and L. I. Glazman, *Helical Edge Resistance Introduced by Charge Puddles*. Phys. Rev. Lett. **110**, 216402 (2013).

[Virtanen11] P. Virtanen and P. Recher, *Dephasing of spin and charge interference in helical Luttinger liquids*. Phys. Rev. B **83**, 115332 (2011).

[Volkov95] A. Volkov, P. Magnée, B. van Wees, and T. Klapwijk, *Proximity and Josephson effects in superconductor-two-dimensional electron gas planar junctions*. Physica C: Superconductivity **242**, 261 (1995).

[vonDelft98] J. von Delft and H. Schoeller, *Bosonization for beginners — refermionization for experts*. Annalen der Physik **7**, 225 (1998).

[Wagner15] S. Wagner, *Topological Anderson insulator with spatially correlated disorder in the Kane-Mele model* (2015), project thesis, University of Basel.

[Wang13] Z. Wang, Z. Liu, and F. Liu, *Organic topological insulators in organometallic lattices*. Nat Commun **4**, 1471 (2013).

[Weeks11] C. Weeks, J. Hu, J. Alicea, M. Franz, and R. Wu, *Engineering a Robust Quantum Spin Hall State in Graphene via Adatom Deposition*. Phys. Rev. X **1**, 021001 (2011).

[Wiedmann15] S. Wiedmann, A. Jost, C. Thienel, C. Brüne, P. Leubner, H. Buhmann, L. W. Molenkamp, J. C. Maan, and U. Zeitler, *Temperature-driven transition from a semiconductor to a topological insulator*. Phys. Rev. B **91**, 205311 (2015).

[Wu06] C. Wu, B. A. Bernevig, and S. Zhang, *Helical Liquid and the Edge of Quantum Spin Hall Systems*. Phys. Rev. Lett. **96**, 106401 (2006).

[Xing11] Y. Xing, L. Zhang, and J. Wang, *Topological Anderson insulator phenomena*. Phys. Rev. B **84**, 035110 (2011).

[Xu06] C. Xu and J. E. Moore, *Stability of the quantum spin Hall effect: Effects of interactions, disorder, and Z_2 topology*. Phys. Rev. B **73**, 045322 (2006).

[Xu13] Y. Xu, B. Yan, H.-J. Zhang, J. Wang, G. Xu, P. Tang, W. Duan, and S.-C. Zhang, *Large-Gap Quantum Spin Hall Insulators in Tin Films*. Phys. Rev. Lett. **111**, 136804 (2013).

[Yang15] Z. Yang, F. Gao, X. Shi, X. Lin, Z. Gao, Y. Chong, and B. Zhang, *Topological Acoustics*. Phys. Rev. Lett. **114**, 114301 (2015).

[Yao07] Y. Yao, F. Ye, X.-L. Qi, S.-C. Zhang, and Z. Fang, *Spin-orbit gap of graphene: First-principles calculations*. Phys. Rev. B **75**, 041401 (2007).

[Zhang14] F. Zhang and C. L. Kane, *Time-Reversal-Invariant Z_4 Fractional Josephson Effect*. Phys. Rev. Lett. **113**, 036401 (2014).

[Zhou08] B. Zhou, H.-Z. Lu, R.-L. Chu, S.-Q. Shen, and Q. Niu, *Finite Size Effects on Helical Edge States in a Quantum Spin-Hall System*. Phys. Rev. Lett. **101**, 246807 (2008).

[Zhu15] F.-f. Zhu, W.-j. Chen, Y. Xu, C.-l. Gao, D.-d. Guan, C.-h. Liu, D. Qian, S.-C. Zhang, and J.-f. Jia, *Epitaxial growth of two-dimensional stanene*. Nat. Mater. **14**, 1020 (2015).